THE EVALUATION OF A SHUTTLE BORNE LIDAR EXPERIMENT TO MEASURE THE GLOBAL DISTRIBUTION OF AEROSOLS AND THEIR EFFECT ON THE ATMOSPHERIC HEAT BUDGET

FINAL REPORT

ON NASA GRANT NSG 1057

APRIL 1975

S. T. Shipley, J. H. Joseph, J. T. Trauger, P. J. Guetter,
E. W. Eloranta, J. E. Lawler, W. J. Wiscombe, A. P. Odell,
F. L. Roesler, J. A. Weinman

Department of Meteorology

University of Wisconsin

Madison, Wisconsin 53706

The Evaluation of a Shuttle Borne Lidar Experiment to Measure the Global Distribution of Aerosols and their Effect on the Atmospheric Heat Budget

Final Report on
NASA Grant NSG 1057
April 1975

S. T. Shipley, J. H. Joseph, J. T. Trauger, P. J. Guetter,
E. W. Eloranta, J. E. Lawler, W. J. Wiscombe, A. P. Odell,
F. L. Roesler, J. A. Weinman

Department of Meteorology
University of Wisconsin
Madison, Wisconsin 53706

Index

The investigations presented in Chapters 1 to 3 are mainly the work of Prof. Joachim H. Joseph of Tel Aviv University and Mr. Peter J. Guetter.* Data with which the δ-Eddington approximation was compared was provided by Dr. W. J. Wiscombe of NCAR. The analysis presented in Chapters 4 is mainly the work of Mr. Scott T. Shipley*. This effort was assited by Dr. Edwin W. Eloranta* and Dr. John Trauger of the Physics Dept. Appendix 4-II was mainly contributed by Prof. A. P. Odell now at Northern Iowa University. Preliminary tests of possible lidar configurations which are described in Chapter 4 were conducted by Mr. James Lawler, Dr. John Trauger and Prof. Fred Roesler of the Physics Dept.

We wish to thank Mrs. E. Singer for her patient typing of the manuscript, Ms. S. Antin for her preparation of the figures, Ms. M. Libal and Mrs. N. Tegen for their diverse support in preparing the figures and editing the manuscript.

James A. Weinman*
Principal Investigator
3/15/75

*Dept. of Meteorology
University of Wisconsin
Madison, Wisconsin 53706

1-0) Preface

The development of the Space Shuttle will provide a unique vehicle from which the global distribution of aerosols may be measured. The Shuttle missions will occur at a time when the interests of the meteorological community are concentrating on a better understanding of the earth's climate. Desert aerosols are the most abundant atmospheric aerosols and it appears that they will significantly affect the climate. A Shuttle-borne lidar system can provide basic data about aerosol distributions for forthcoming models of climate.

Chapter 1 of this report summarizes our present knowledge of the physical characteristics of desert aerosols and the absorption characteristics of atmospheric gas. Chapter 2 presents an analysis of radiative heating computations. Computational simplicity and adequate accuracy are fundamental criteria which any computational scheme must satisfy in order to be useful as part of a comprehensive climatic model. Sample computations of the radiative heating effects produced by desert aerosols are also presented in Chapter 2. General circulation models are insensitive to changes in heating rates less than 0.5°K/day; this ultimately determines the accuracy with which the aerosol distribution must be determined by the Shuttle-borne lidar. These considerations are presented in Chapter 3.

A high spectral resolution lidar can provide profiles of the aerosol extinction coefficient. Tables 3-1 and 3-2 establish criteria for height resolution and the accuracy with which the lidar must provide aerosol extinction coefficients. The analysis of Chapter 4 presents the characteristics of a Shuttle-borne lidar that will satisfy the criteria established in Chapter 3. Chapter 4 also presents some laboratory studies which seek to identify schemes that might permit the implementation of a high spectral resolution lidar system.

1-1) Introduction

Climatic variability is a major hazard which afflicts agricultural production. Much attention has been devoted to the influence of atmospheric constituents on the heat budget and its possible long-term impact on climatic trends, see e.g. SMIC report (1971). The distribution of radiatively active constituents such as aerosols and clouds may produce changes in the distribution of surface temperatures (duration of growing season) or precipitation (drought or floods) before longer range trends such as ice ages become significant. General circulation patterns are influenced by the vertical stability of the atmosphere. The temperature profiles which determine this stability are affected by the vertical distributions of radiatively active constituents which may alter radiative heating or cooling rates.

Global measurements of the vertical distributions of clouds and aerosols will be required as input for models needed to study the influence of aerosols and clouds on climatic variability. Lidar can be used to measure the vertical distribution of aerosols and clouds; and the development of the space shuttle provides a vehicle which may be used to transport a lidar system over much of the earth.

Cloud top heights are easily determined by lidar. The optical thickness of cirrus clouds can also be readily determined by lidar. While these quantities are of considerable meteorological interest in their own right, we will confine our attention to aerosols and their heating effect on the atmosphere. The reasons for this choice are that desert aerosols are more wide spread than anthroprogenic aerosols, they are found nearer to the equator where they may interact more effectively with solar radiation, they frequently appear in cloud free regions so that their radiative effects are not obscured by clouds, and they are more difficult to measure with a lidar than clouds.

1-2) The Desert Aerosol

1-2-a) Geographical Distribution and Climatic Role of Desert Aerosols

The desert aerosol is probably the most wide-spread natural aerosol. Figure 1-1 shows the approximate global distribution of desert aerosol sources. The largest source is the long band of deserts and steppes stretching from West Africa east through the Sahara, the Sahel, the Lybian and Egyptian deserts, the Sudan, Saudi Arabia, Jordan, Israel, Syria, Iraq, Iran, Pakistan, and India. The second source is located in the extensive Siberian and Chinese deserts. Other sources, are located in South Africa, South America, Australia and the Western U.S. All together, deserts comprise about eight percent of the Earth's surface or close to one third of the total land surface. The total output of "long-lived" dust from this source is at least 120 million metric tons annually according to Carlson and Prospero, (1972) and Joseph et al., (1973) and it may reach more than four times this value, see Goldberg, (1971). An upper bound to the global atmospheric aerosol load of the order of 2000 million metric tons/year was cited in the SMIC report, (1971).

There is evidence that overcultivation of marginal lands promotes the development of deserts. As population pressure places more marginal land under cultivation, the aerosol density in the atmosphere may be expected to increase.

One reason for the climatic importance of desert aerosol is that small changes in climate or in man's activities may cause considerable displacement of arid zone boundaries. The more arid the climate thus becomes, the more desert aerosol will be introduced on a global scale into the atmosphere. There might thus be an initial positive feedback mechanism between desertification and a change in radiation balance due to desert aerosol.

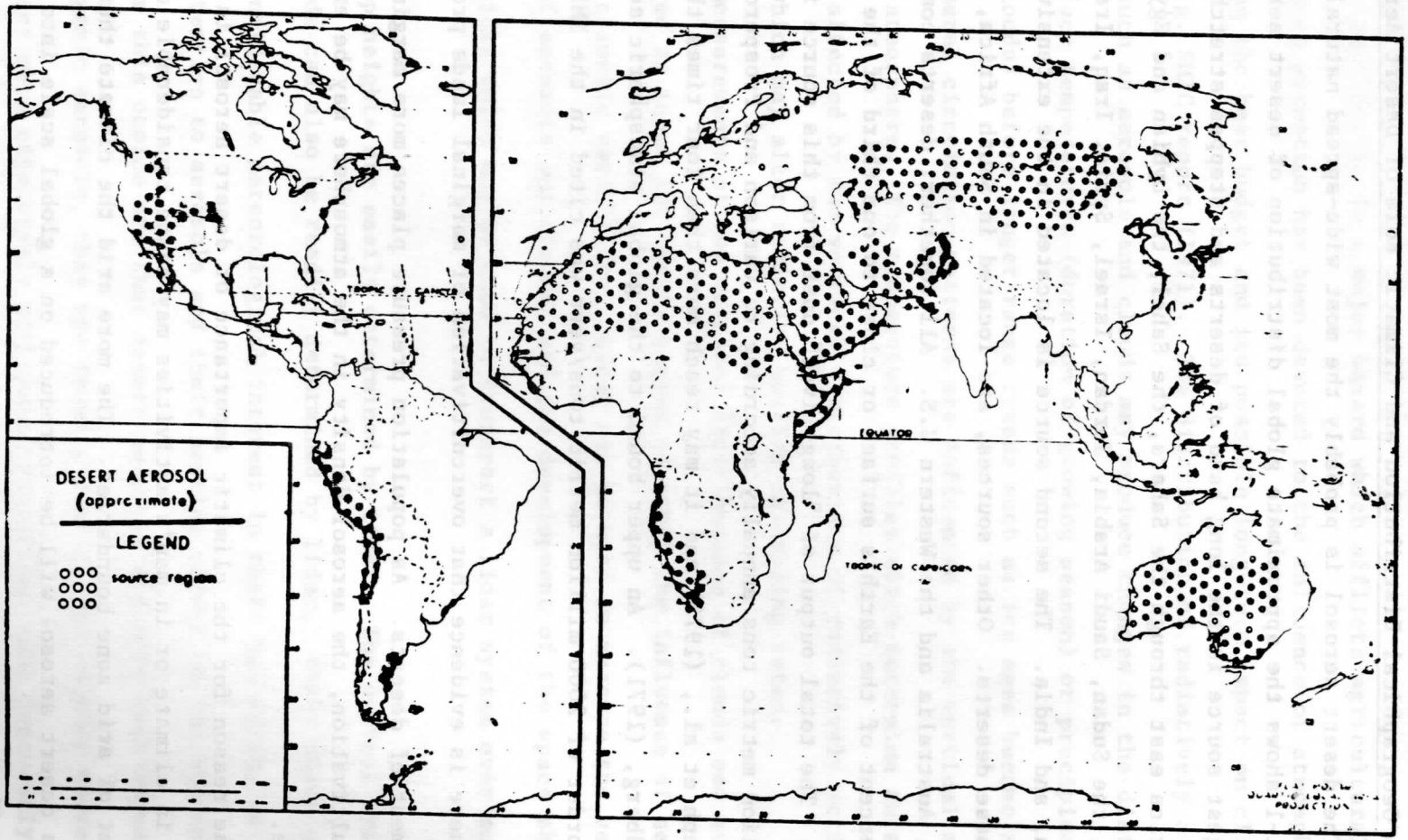

Fig. 1-1 Global distribution of desert aerosol sources and regions over which the atmosphere frequently contains aerosols. From The Times Atlas of the World, London, Times Newspapers Ltd. (1968) pp 272.

Heavy desert dust deposition far away from its source has been reported extensively. North African dust has been reported in Northern Europe by Morikofer, (1941) and Stevenson, (1969), in the West Indies by Prospero, (1968); and Carlson and Prospero, (1971). Desert aerosols have been shown to exist in the atmosphere at low and sub-tropical latitudes by Peterson, (1968); Bryson and Wendland, (1970); Volz, (1970); Volz and Sheehan, (1971); SMIC (1971); Joseph and Manes, (1971); Joseph et al., (1973); and Sargent and Beckman, (1973).

The appearance of desert dust in large quantities over Japan and the Western and Central Pacific is correlated in spring with the northward migration of the 0°C isotherm in the Central Asian deserts. T. Kitaoka, (1971), indicates that the turbidity over Japan may increase by 300% when this dust appears. The wind-borne desert aerosol from Asia has also been found in geologically and pedologically important amounts on the islands of Hawaii by Jackson et al., (1971). Heavy dust falls reported by ships in the Pacific up to 3000 km from the source, have been cited by Ing (1972).

The horizontal distribution of aerosol in large scale air masses is dense enough so that its presence is easily detectable in broadband satellite photographs obtained in reflected sunlight.

1-2-b) Vertical Distribution of Desert Aerosols

Desert aerosols are very dense over source regions. Surface concentrations are very frequently of the order of 1000 $\mu g/m^3$ according to Peterson, (1968). The average surface mass concentration in the desert aerosol layer is between 30-300 $\mu g/m^3$ away from the source, see Carlson and Prospero, (1972), Reynolds et al., (1973) and Joseph et al., (1973). These mass concentrations are comparable to those found where man-made

pollution is severe. This is one reason why natural desert aerosols may be more significant to the global energy balance than man-made aerosols.

The presence of desert aerosols is clearly evident in visibility measurements. In very dense desert haze (not a sand storm) the visibility may be less than one km. In the Middle East area, days with visibility less than about 10 km have a frequency of occurrence of about 50-200 per year according to Manes and Guetta, (1973), and Lentz and Hoidale, (1974).

Prospero, (1968), and Carlson and Prospero, (1972) found that desert aerosols are usually transported away from their source in an isentropic layer. Over the Atlantic Ocean this layer is usually found between 800 and 500 mb. Below this layer, the air contains very little desert aerosol, Junge, (1972). The same stable layers in which the desert aerosol is advected were also found over the Middle East by Joseph, Ashbell and Eviatar, (1961). However, the aerosol has been found well-mixed to high altitudes over the source region by Peterson (1968), and Peterson and Bryson, (1968).

1-2-c) Physical Properties of Desert Aerosols

A study of the effect of a model aerosol, with properties similar to a desert aerosol, on total solar and infra-red radiative fluxes, flux-divergence and radiative-convective temperature profiles has been published recently by Wang and Domoto, (1974). They found that the absorption of the aerosol was equal to that of the water vapor in the solar spectral region. Over regions of high albedo (e.g. deserts), an increase in the aerosol concentration will heat the earth-atmosphere system. Furthermore, convection is suppressed by the presence of aerosol and in the case of a "dense" aerosol (visibility $\lesssim$ 5 km), a temperature inversion layer is formed. Net heating rates in the lowest layers are changed by about 1.0°K day^{-1}.

An experimental study by Reynolds et al., (1973) shows that the presence of a layer of desert aerosol aloft in the tropical oceanic atmosphere may shift the net (solar + thermal infra red) radiation heating rate curve downward in altitude and increase the heating at the altitude where the concentration is a maximum.

The stabilizing effect of solar absorption by the atmospheric aerosol and its greenhouse effect in the thermal infra-red may play a significant role in maintaining temperature inversions over deserts and it may affect convection over oceans. The peculiar height distribution of the desert aerosol over the tropical oceans may increase the static stability enough to inhibit the rainfall during daylight hours.

Joseph, (1970), (1971), Stowe, (1971), and Jacobowitz and Coulson (1973) have shown that the presence of aerosol over a surface will also significantly affect the remote determination of the surface temperature from a satellite.

It is thus extremely important to study the vertical distribution of the desert aerosol on a global basis.

1-2-d) Composition of the Desert Aerosol

The composition of desert aerosols has been investigated by Junge, (1972), Goldberg, (1971), Carlson and Prospero, (1972), Kondratiev, (1972), Volz, (1971), Peterson (1968), Lentz and Hoidale, (1974), Lindberg and Laude, (1975), and Bullrich et al. (1973).

The largest fraction of the desert dust is a variety of silicate clays, together with admixtures of calcite, quartz, sodium nitrate and organic matter. Organic matter or iron compounds may be necessary to explain the relatively high measured absorptivity of the desert aerosol for visible solar radiation found by Joseph and Wolfson (1975), and Kondratiev (1972); (1974).

The composition by weight summarized in Table 1-1 is based primarily on work by Lentz and Hoidale, (1974).

Table 1-1 Composition of Desert Aerosol

Montmorillonite	35%
Kaolinite	20%
Illite	20%
Calcite	10%
Iron Compounds (Limonite), Organic Compounds	5%
Quartz	5%
Sodium Nitrate	5%

The silicaceous clays that comprise the bulk of desert aerosol and possibly organic material that adheres to the clay particles, found by Gillette et al., (1974), are excellent natural cloud seeding agents. This fact may lead to a significant effect on cloud and rain formation and cloud optical properties. This property of the clays may lead to a profound diurnal change of the aerosol over deserts. During daytime, when the relative humidity becomes quite low, aerosols may be dry and non-spherical. Such aerosols absorb both solar radiation and thermal radiation. At night the relative humidity often approaches 100 percent; the aerosols may rapidly change their optical properties, their shape and their size distribution as water is adsorbed onto the aerosols. Such aerosols will absorb less in the visible in the early morning hours till the water-vapor evaporates. Some experimental indications of such a phenomenon have been reported by Vittori et al., (1974) for aerosols in Italy.

Lindberg, (1974) found that the hydroxyl bonds in clays have absorption bands in the near infra-red and these may simulate the radiative effect of water vapor. The absorption of solar radiation by desert aerosols is about equal in magnitude to that of water-vapor according to Reynolds et al., (1973); and Kondratiev, (1972,1973), Kondratiev et al., (1972), (1974).

1-2-e) Refractive Index of Desert Aerosol

(1) The Solar Spectral Region: .4 μm < λ < 1.1 μm.

Most measurements and theoretical evaluations agree that the real part of the refractive index of "dry" (ambient relative humidity $\lesssim$ 60%) desert aerosol is of the order $1.46 \lesssim n \lesssim 1.54$. This is the range of values appropriate for both amorphous and crystallite quartz according to Day et al., (1974), and for siliceous clays like kaolinite according to Steyer et al., (1974). It is too low for iron or organic compounds which comprise at most 5% of desert aerosols. We suggest the value of n = 1.54 in the spectral range .4 μm < λ < 1.1 μm.

There is much less agreement on the value of the imaginary part of the refractive index, k, see Fig. 1-2. The highest values are those deemed appropriate for limonite, see Kondratiev et al., (1972),(1974). The lowest values are those of Lindberg and Laude, (1975), based on reflectivity measurements of a desert aerosol diluted in a powder matrix. Brinkworth (1972) suggests that such results may be too low by a factor of about 2. The values used by McClatchey et al. (1970) are based on Volz's (1957) data. Joseph and Wolfson (1975) deduced a mean value for the spectral region .3 μm < λ < 2.5 μm of k = .03 ± .02 on the basis of solar flux measurements. The curve 3K in Figure 1-2 shows the Lindberg and Laude curve shifted upward by a factor of 3 to coincide with that reported by Kondratiev. The range of uncertainties for k thus seems to lie between that of limonite and the "desert dust" curve

of Lindberg and Laude (1974), in which there is no limonite. It is impossible to fix the value any better. The curves presented by Kondratiev et al. (1974) are the most acceptable values.

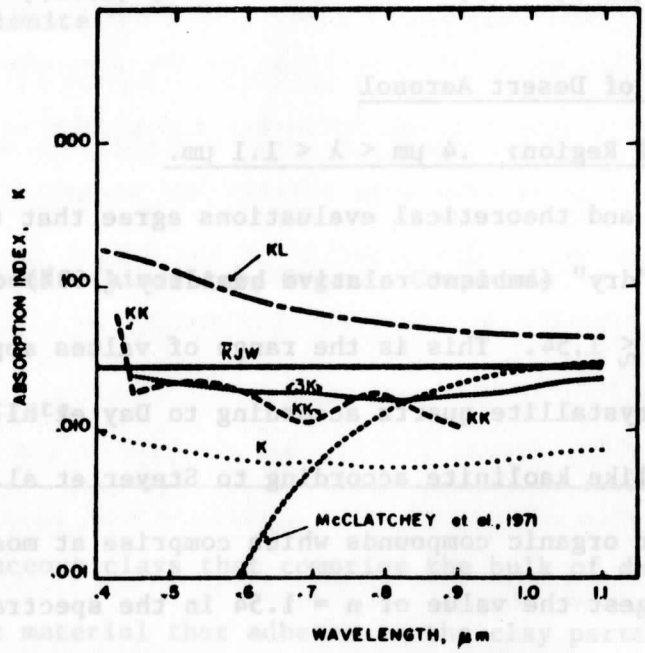

Figure 1-2. The absorption index of desert aerosols in the solar visible region.

K: Desert dust - Lindberg and Laude (1975)

3K: 3X desert dust - Lindberg and Laude (1975)

KK: Desert dust - Kondratiev et al. (1974)

$\bar{K}JW$: Average desert dust - Joseph and Wolfson (1975)

KL: Limonite - Egan and Becker (1968), Kondratiev (1972)

(2) The Solar Spectral Region: $1.1\ \mu m \leq \lambda < 2.5\ \mu m$

Lindberg and Smith, (1974), and Kondratiev, (1972) presented the most recent data on the properties of desert aerosol clays in this spectral region. Their data show a continuous extinction with an extinction coefficient between .01 cm^{-1} and 1 cm^{-1}, leading to $8 \times 10^{-6} \gtrsim k \gtrsim 2 \times 10^{-7}$. Superimposed on this are band-absorption features centered on the water-vapor absorption bands.

The value of k in these bands may reach $1 \times 10^{-4} \lesssim k \lesssim 1 \times 10^{-3}$ and $.002 \lesssim k \lesssim .02$ in the 2.7 μm band. The absroption in these bands depends on the state of hydration of the clay sample.

We recommend the averaged values of $\bar{n} = 1.54$ and $\bar{k} = .008$. These values are based on spectral averaging using the solar spectrum as a weighting function. The value of $\bar{k}$ may be twice as large (Brinkworth, 1972).

(3) The Thermal Infra-red Spectral Region: $\lambda \geq 2.5$ μm

All materials that may be present in desert aerosols have strong absorption bands in this region and they may be bi-refringent. Peterson and Weinman, (1969), and Steyer et al., (1974) present results for quartz, and Lentz and Hoidale (1974), present results for silicate clays and carbonates. The imaginary part of the refractive index varies over several orders of magnitude in the shortwave and the 8 μm < λ < 12 μm parts of this spectral region. The maximum extinction coefficient may be 15-20 times larger than in the solar range, Day et al., (1974). The same authors show that the determination of the imaginary part of the refractive index by transmissometry of samples dispersed in a matrix under-estimates the absorption at the peak by about a factor of three due to saturation. However, the spectrally integrated absorption as evaluated by Mie calculations based on the conventional data, gives the absorption within 15 percent. It follows thus that a "band model" for aerosol absorption based on these Mie calculations should have reasonable success in simulating the infra-red optical effect of aerosols.

Evidence of the global homogeneity of the desert aerosol is demonstrated in Figure 1-3 which shows the imaginary part of the refractive index of desert aerosol as found in the Western U.S. by Lentz and Hoidale, (1974). Two similar sets of the spectral determinations of the same quantity from the desert of Israel are also shown. The large variability from dust storm to dust storm and even in one storm is also evident from the difference in the two sets of measurements in the Israeli desert, which were taken by Fischer (1972).

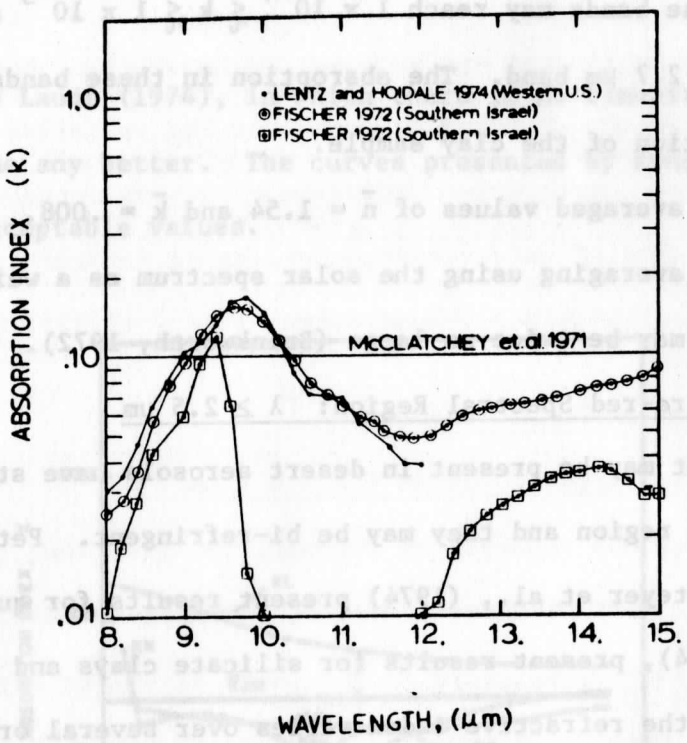

Figure 1-3. Imaginary part of the refractive index of desert aerosols in the spectral region of the atmosphere's infra-red window.

The real part of the refractive index may thus be taken as n = 2.45 and the imaginary part may be taken from Lentz and Hoidale's model of the optical constants of the desert aerosol.

1-2-f) Size Distribution of Desert Aerosols

The size distribution of desert aerosol has been investigated by Junge, (1972), Bullrich, et al. (1973), Lentz and Hoidale (1974), Volz (1970), Joseph and Manes (1971), Joseph et al., (1973), Joseph and Guetta (1975), Prospero, (1968), Carlson and Prospero, (1972), Peterson (1968), Bryson et al. (1964), Bryson and Peterson (1968), Lindberg and Laude (1975), Lentz and Hoidale (1974), Grams et al. (1972), Shaw et al. (1973), Kondratiev (1972), Kondratiev et al. (1972), Schutz and Jaenecke, (1974).

On the average, the experimental size distributions may be represented by a sum of two incomplete gamma-functions, one peaking between 1 and 10 μm, the other at radii less than 1 μm

$$n(r) = n_1(r) + n_2(r)$$
$$= a_1 r^{\alpha_1} \exp(-b_1 r^{\gamma_1}) + a_2 r^{\alpha_2} \exp(-b_2 r^{\gamma_2}) \qquad 1\text{-}2.1)$$

$a_1 = 3.5 \times 10^5$, $cm^{-3}\mu m^{-3}$ $\alpha_1 = 2.$, $b_1 = 20.$ $\mu m^{-\frac{1}{2}}$, $\gamma_1 = .50$

$a_2 = 2.9 \times 10^5$ $cm^{-3}\mu m^{-11}$, $\alpha_2 = 10.$, $b_2 = 10.$ μm^{-1}, $\gamma_2 = 1.0$

Assuming the mass density to be 2.0, the corresponding mass M_1 is 1.25 $\mu g/m^3$ and M_2 is 299. $\mu g/m^3$ for a "normal" desert aerosol.

The $n_1(r)$ is introduced because the desert clays cannot absorb solar radiation in the amounts experimentally found. The simple way of providing for the absorption is to add a small mass of limonite in the form of small particles. Kondratiev (1973) also found that limonite is only in aerosols with r<1 μm and that the larger aerosols are clays.

Not enough data are available to say much about the change in height of the size-distribution. Due to the efficient mixing by convection of the air over deserts we shall assume that the size distribution is independent of height.

An estimate of the parameters of the size distribution of desert aerosols can be obtained in the following way:

The refractive indices, as presented previously, have been used to compute the Mie optical depths for extinction in the solar spectrum, 0.4 μm $< \lambda <$ 1.1 μm, and in the 8.0 μm $< \lambda <$ 12.5 μm thermal infra-red region for a range of values of the parameters of the size-distribution. In the infra-red, $n_2(r)$ is the main contributor to the optical depth whereas $n_1(r)$ and $n_2(r)$ are both important in the solar visible and near infra-red.

Our comparisons show that the parameters cited for $n_2(r)$ yield

a best fit between the optical depths computed from Mie theory in the 8.0 μm < λ < 12.5 μm region with those reported by Lentz and Hoidale (1974).

We then take the optical depths in the visible, based on this best-fit size distribution, $n_2(r)$, and combine it with a set of extinction optical depths for limonite with a size distribution $n_1(r)$. The parameters of the size-distribution $n_1(r)$ are then varied to obtain a best fit to the spectral extinction of solar radiation.

The best fits, $n_1(r)$ and $n_2(r)$, are compared with various size distributions in Figure 1-4. The sum of these two distributions constitute our proposal for the average size distribution of the desert aerosol as found over the oceans or over deserts during calm conditions.

1-2-g) The Maximal Amounts of Desert Aerosol

In order to describe the extreme effects of desert aerosols on thermal infra-red heating rates as measured by Bryson et al., (1964), for example, quite large optical depths must be assumed ($\tau \sim 3 - 6$). Above "normal" optical depths are also needed to partially explain the decreased cooling in the lower troposphere observed by Peterson (1968). This means that between 10 - 20 x normal amounts of $n_2(r)$ are needed to explain the Bryson et al. case and 1 - 10 x normal are required to account for the Peterson measurements. Measurements of the concentration of large particles over the Sahara Desert by Schütz and Jaenicke (1974) indeed show concentrations of large particles which are 5 - 10 times greater than were assumed in the derivation of our "normal" desert aerosol.

The average optical depth at $\lambda \simeq 0.5$ μm of the aerosol during Khamsinic phenomena over Israel is .4, however, optical depths exceeding 1 occur about 10 percent of the time, Joseph and Manes (1971), Joseph, Manes and Ashbell (1973),

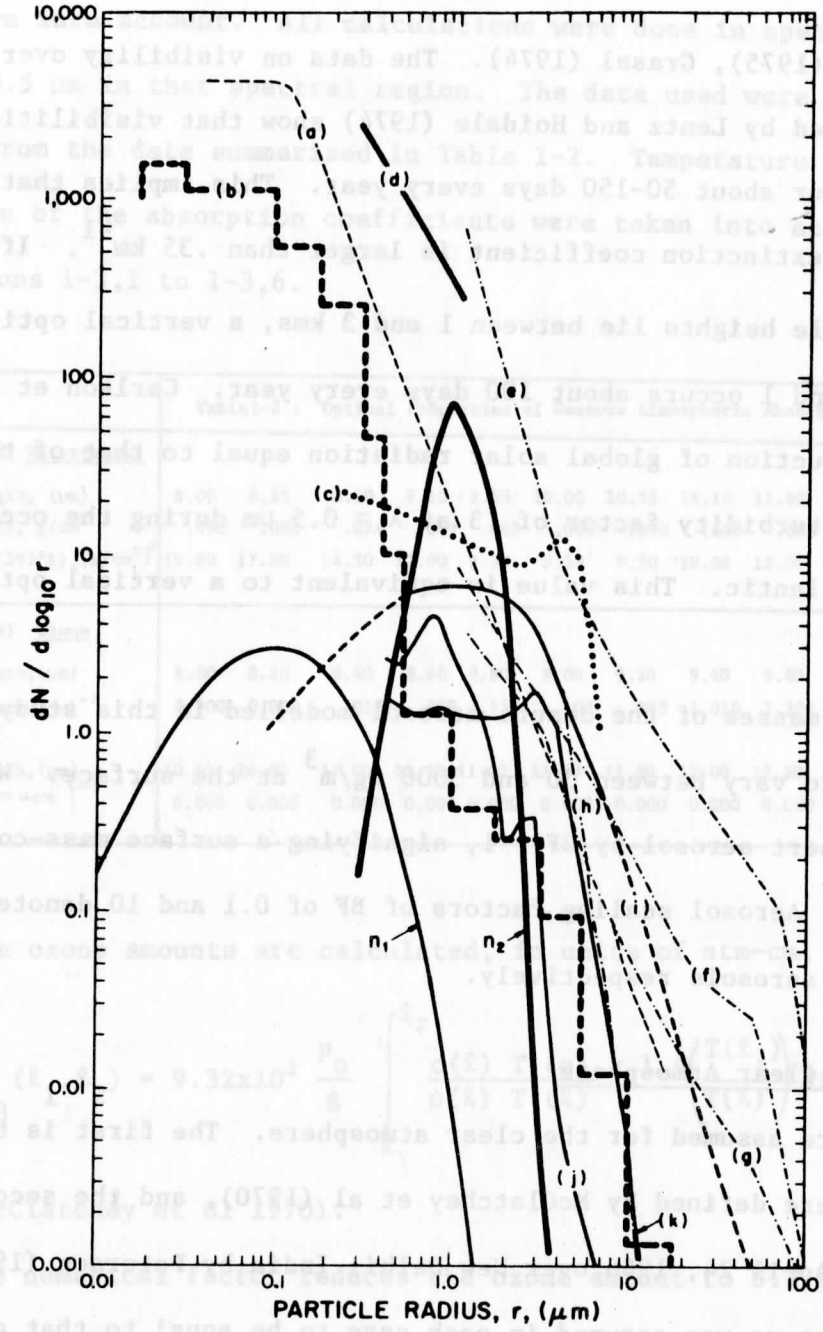

Figure 1-4 Size distributions of desert aerosols (a) Rajasthan desert - Peterson (1968), (b) Colorado - Whitby (1974), (c) Texas - Gillette et al. (1972), (d) Rajasthan desert - Bryson et al. (1964), (e) Sahara sand storm - Schütz and Jaenicke (1974), (f) Camp Derji Sahara, sand storm - Schütz and Jaenicke (1974), (g) Mean of Sebha, Sahara - Schütz and Jaenicke (1974), (h) Atlantic Ocean - Schütz and Jaenicke (1974), (i) Grams et al. (1974), (j) and (k) deLuisi, private communication.

Joseph and Wolfson (1975), Grassl (1974). The data on visibility over the Middle East collected by Lentz and Hoidale (1974) show that visibilities less than 11 km occur about 50-150 days every year. This implies that the visible horizontal extinction coefficient is larger than .35 km^{-1}. If typical aerosol scale heights lie between 1 and 3 kms, a vertical optical depth between .35 and 1 occurs about 100 days every year. Carlson et al. (1973) report a reduction of global solar radiation equal to that of thin clouds and a Linke turbidity factor of .3 at $\lambda \simeq 0.5$ μm during the occurrence of dust over the Atlantic. This value is equivalent to a vertical optical depth of .69.

The range of masses of the desert aerosol modelled in this study is therefore assumed to vary between 30 and 3000 $\mu g/m^3$ at the surface. We shall denote a normal desert aerosol by BF = 1, signifying a surface mass-concentration of 300 $\mu g/m^3$. Aerosol scaling factors of BF of 0.1 and 10 denote "light" and "heavy" desert aerosols respectively.

1-3 Models of the Clear Atmosphere

Two models were assumed for the clear atmosphere. The first is that of a tropical atmosphere defined by McClatchey et al (1970), and the second is that given for April 24, 1966 over New Delhi, India by Peterson (1968). The surface temperature was assumed in each case to be equal to that of the air at the surface. The main difference between the two is the higher air temperatures below 700 mb in the New Delhi case. The air temperatures at the surface, at 900 mb and 800 mb, are about 10°K higher. That at 700 mb is two degrees higher. The water-content is about the same. The ozone-profile from the McClatchey model was used in both cases.

The optical properties of water-vapor at 8 μm < λ < 13 μm were taken from the study of Cox (1973) and both continuous and e-type absorption

were taken into account. All calculations were done in spectral intervals of $\Delta\lambda \simeq 0.5$ μm in that spectral region. The data used were linearly interpolated from the data summarized in Table 1-2. Temperature and pressure dependence of the absorption coefficients were taken into account as shown in Equations 1-3,1 to 1-3,6.

Table 1-2 : Optical Properties of Gaseous Atmospheric Absorbers

(a) Water-vapor													
Wavelength, (μm)	8.00	8.35	8.70	9.10	9.55	10.00	10.55	11.10	11.80	12.50	13.35		
$K_W(293°K)$, g/cm^2	.090	.080	.074	.069	.062	.068	.090	.100	.102	.108	.113		
$K_{e\text{-type}}(293°K)$, $[g/cm^2]^2$	19.80	17.00	14.50	12.00	9.30	9.30	9.50	10.00	12.00	14.00	20.00		
(b) Ozone													
Wavelength, (μm)	8.00	8.20	8.40	8.60	8.80	9.00	9.20	9.40	9.60	9.80	10.00	10.20	10.40
K_{O_3} $(atm-cm)^{-1}$	0.000	0.000	.015	.079	.128	.105	.083	1.016	2.303	2.659	1.609	.431	.051
Wavelength, (μm)	10.60	10.80	11.00	11.20	11.40	11.60	11.80	12.00	12.20	12.40	12.60	12.80	13.00
K_{O_3} $(atm-cm)^{-1}$	0.000	0.000	0.000	0.000	0.000	0.000	0.000	0.000	0.000	0.000	.008	.020	.051

The ozone amounts are calculated, in units of atm-cm, reduced to S.T.P.

$$u_{O_3}(\ell_1,\ell_2) = 9.32\times10^2 \frac{p_o}{g} \int_{\ell_1}^{\ell_2} \frac{c(\ell)\ T\ (o)}{\rho(\ell)\ T\ (\ell)}\ \ell^{1.4}\left(\frac{T(\ell_1)}{T(\ell)}\right) d\ell \qquad 1\text{-}3,1$$

(McClatchey et al 1970).

The numerical factor reduces the ozone amount to S.T.P.

$\ell \equiv p/p_o$

p_o is surface pressure in dyne cm^{-2}

g the gravitational constant in cm sec^{-2}

c the ozone concentration in g/m^3

ρ the air density in g/m^3

Water-vapor amounts were modelled by

$$u_{H_2O}(\ell_1, \ell_2) = \frac{p_1 q(p_1)}{g} \int_{\ell_1}^{\ell_2} c(\ell) \left(\frac{T(\ell_1)}{T(\ell)}\right)^{1/2} \frac{\ell \; f(\ell) \; d\ell}{\rho(\ell)} \qquad 1\text{-}3,2$$

$$u(\ell_1, \ell_2)_{H_2O,\ e\text{-type}} = \frac{p_1 q^2(\ell_1)}{.622g} \int_{\ell_1}^{\ell_2} \frac{C(T)}{C(293°K)} \ell \; f^2(\ell) \; d\ell \qquad 1\text{-}3,3$$

where $p_o = 1.01 \times 10^6$ dyne-cm^{-2}

$q(1) = 1.63 \times 10^{-2}$ /g

$g = 981$ cm sec^{-2}

$T_1 = 273°K$

T = temperature, °K

$$C(T) = 2 + x(T) - [(2 + x(T))^2 - 4]^{1/2} \qquad 1\text{-}3\text{-}4$$

$$x(T) = \frac{.622 \exp\{-c_1 - (c_2/T)\}}{q(\ell_1) \quad f(\ell)} \qquad 1\text{-}3\text{-}5$$

$$f(\ell) = \begin{cases} \ell^{3.56} & .130 \le \ell \le 1 \\ (.130)^{3.56} & .001 \le \ell \le .130 \\ 0 & \ell < .001 \end{cases} \qquad 1\text{-}3\text{-}6$$

$c_1 = 13.01$ (Cox 1973)

$c_2 = 2878.2°K$

The models for absorption by gases outside the 8.0 μm < λ < 12.5 μm window are based on those of Rodgers and Walshaw (1966), and Rodgers (1967) and used conventionally in the manner cited by R. Bursztyn (1974), to evaluate fluxes in 65 pressure intervals from the surface to 1 mb.

References: Chapter 1

Brinkworth, B. J., (1972): Interpretation of the Kubelka-Munk Coefficients in Reflection Theory, Appl. Opt. 11, 1434.

Bryson, R. A., and J. T. Peterson, (1968): Influence of Atmospheric Particulates on the Infra-red Radiation Balance of Northwest India. Proc. Nat. Conf. Weather Mod., Albany, N. Y., April 28 - May 1, 1968, pp. 153-162.

Bryson, R. A., W. M. Wendland (1970): Climatic Effects of Atmospheric Pollution - Global Effects on Environmental Pollution, s. F. Singer, Ed., D. Reidel Pub. Co., 130-138.

Bryson, R. A., C. W. Wilson, and P. Kuhn, (1964): Some Preliminary Results From Radiation Sonde Ascents Over India, Proc. Symp. Trop. Met., Rotorua, New Zealand, 5-13 Nov. 1963, N.Z. Met. Service, 507-516.

Bullrich, K., R. Eiden, G. Eschelbach, K. Fischer, G. Hänel, J. Heintzenberg, (1973): "Scattering and Absorption from Poly-Dispersed Aerosols", The UCLA Conference on Radiation and Remote Probing of the Atmosphere, August 28-30, 1973, Dept. of Met., UCLA, J.G. Kuriyan, Ed., 135-162.

Bursztyn, R., (1974): A Model, for the Computation of Atmospheric Radiative Cooling-Rates in the Thermal Infra-Red, Based on the Exchange Between Atmospheric Layers, M.S. Thesis Dept. Environ. Sci., Tel-Aviv Un.pp. 791.

Carlson, T.N., J.M. Prospero, (1971): The Large-Scale Movement of Saharan Air Outbreaks Over the Northern Equatorial Atlantic. J. App. Met., 11, 283-297.

Carlson, T.N., J.M. Prospero, (1972): Vertical and Areal Distribution of Saharan Dust over the Western Equatorial North Atlantic Ocean, J. Geophys. Res., 77, 5255-5265.

Carlson, T.N., J.M. Prospero, K.J. Hanson, (1973): Attenuation of Solar Radiation by Wind-Borne Saharan Dust Off the West Coast of Africa. U.S. Dept. of Commerce, NOAA Tech. Memo. ERL WMPO-7, 27.

Cox, S. K., (1973): Infra-Red Heating Calculations with a Water Vapour Pressure Broadened Continuum. Quart. J. Roy Met. Soc., 99, 669-679.

Day, K. L., T. R. Steyer and D. R. Huffman, (1974): A Quantitative Study of Silicate Extinction (To be Published in Ap. J.).

Egan, W. G., Becker, J. F., (1968): Determination of the Complex Index of Refraction of Rocks and Minerals, Grumman Aircraft Eng. Co., Bethpage, N. Y. 11714, Annual Meeting Opt. Soc. Am., Pittsburgh, Penn., Oct. 9-12.

Fischer, D., (1972): Private Communication.

Gillette, D. A., I.H. Blifford Jr., C. R. Fenster, (1972): Measurements of Aerosol Size Distributions and Vertical Fluxes of Aerosols on Land Subject to Wind Erosion, J. App. Met., 11, 977-987.

Gillette, D. A., (1974): NCAR Aerosol Project Report for FY-1974.

Goldberg, E. D., (1971): "Atmospheric Dust - the Secimentary Cycle and Man", Comments on Earth Sciences, Geophysics 1, 117-132.

Grams, G. W., I. H. Blifford, Jr., D. A. Gillette and P. B. Russell (1972): Complex Index of Refraction of Airborne Soil Particles, J. Appl. Met., 13, 459-471

Grassl, (1974): Private Communication.

Ing. G.N.T., (1972): A Duststorm Over Central China April 1969, Weather 27, 136-145.

Jackson, M.L., T.W.M. Levelt, J.K. Syers, R.W. Rex, R. N. Clayton, G. D. Sherman, G. Uehara, (1971): Geomorphological Relationships of Tropospherically Derived Quartz in the Soils of the Hawaiian Islands. Soil Sci. Soc. of Am. Proc. 35, 515-526.

Jacobowitz, K.L. Coulson, (1973): Effects of Aerosols on the Determination of the Temperature of the Earth's Surface From Radiance Measurements at 11.2 μm. NOAA Technical Report, NLSS 66. pp. 18.

Joseph, J.H., (1970): Thermal Radiation Fluxes Through Optically Thin Clouds. Isr. J. Earth Sci., 19, 51-67.

Joseph, J. H., (1971): Thermal Radiation Fluxes Near the Sea Surface in the Presence of Marine Haze. Isr. J. Earth Sci., 20, 7-12.

Joseph, J. H., D. Ashbel and A. Eviator (1961): Unpublished Report.

Joseph, J.H., D. Guetta, (1975): The Wave-Length Dependence of the Optical Depth of Khamsinic Aerosol in the Visible and in the Solar Infrared Spectrum, (To be submitted to the J. Atm. Sci.).

Joseph, J.H., A. Manes, (1971): Secular and Seasonal Variations of the Atmospheric Turbidity in Israel at Jerusalem. J. App. Met., 10, 453-462.

Joseph, J. H., A. Manes, D. Ashbell, (1973): Desert Aerosols Transported by Khamsinic Depressions and their Climatic Effects. J. App. Met., 12, 792-797.

Joseph, J.P., N. Wolfson, (1975): The Ratio of Absorption to Back-Scatter of Solar Radiation by Aerosols During Khamsin Conditions and Effects on the Radiation Balance. J. App. Met. (In Press).

Junge, C. E., (1972): Our Knowledge of Physico-Chemistry of Aerosols in the Undisturbed Environment, J. Geophys. Res., 77, 5183-5200.

Kitaoka, T. (1971): Private Communication.

Kondratiev, K. Ya., (1972): Radiation Processes in the Atmosphere, W.M.O. Monograph 309.

Kondratyev, K. Ya., (1973): The Complete Atmospheric Energetics Experiment G.A.R.P. Publ. Series No. 12,W.M.O./I.C.S.U. pp. 43.

Kondratiev, K. Ya., V.F. Malev, L.S. Ivlev, S.P. Malevsky, L.R. Orlenko, O.I. Popov, Yu. I. Rabinovich, N.E. Ter-Markaryants, L.I. Chapevsky, V.I. Shlyakov, (1972): The Preliminary Results of the First Expedition According to the Programme of Complex Atmospheric Energetics Experiment (CAENEX-70) (Unpublished Report)

Kondratyev, K. Ya., O.B. Vassilyev, V.S. Grishechkin, L.S. Ivlev, (1974): Spectral Radiative Flux Divergence and Its Variability in the Troposphere in the 0.4-2.4-μ Region. App. Opt. 13, 478-486.

Lentz, W.J., G.B. Hoidale, (1974): Estimates of the Extinction of Electromagnetic Energy in the 8 to 12 μm Range by Natural Atmospheric Particulate Matter. U.S. Army Electronics. E.C.O.M. - 5528, Fort Monmouth, N.J.

Lindberg, J.D., L.S. Laude, (1975): A Measurement of the Absorption Coefficient of Atmospheric Dust. Appl. Optics. (In Press)

Lindberg, J.D., M.S. Smith, (1974): Visible and Near Infrared Absorption Coefficients of Kaolinite and Related Clays. Am. Miner., 59, 274-279.

Manes, A., D. Guetta, (1973): Unpublished Report, Israel Meteorological Service.

McClatchey, R.A., R. W. Fenn, J.E.A. Selby, J.S. Garing, F.E. Volz, (1970): Optical Properties of the Atmosphere, Envi. Res. Papers, 31, A.F.C.R.L., pp. 85.

Morikofer, W., (1941): Uber die Trübung der Atmosphäre durch Wüsten - Staub und Schnee - treiben. Helv. Phys. Acta. 16, 537-539.

Peterson, J.T., (1968): Measurement of Atmospheric Aerosols and Infrared Radiation Over Northwest India and Their Relationship. UW-Wis., Technical Report No. 38. pp. 165.

Peterson, J. and R.A. Bryson, (1968): Increased Aerosol Concentrations During the Last Decade, Science 162, 3849.

Peterson, J.T., J.A. Weinman, (1969): Optical Properties of Quartz Dust Particles at Infra-Red Wavelengths, J. Geophys. Res., 74, 6947-6952.

Prospero, J.M., (1968): Atmospheric Dust Studies on Barbados. Bull. Am. Met. Soc., 49, pp. 645.

Reynolds, D.W., T.H. Vonder Haar, S.K. Cox, (1973): The Effect of Solar Radiation Absorption in the Tropical Troposphere. Atmosph. Science Paper No. 210, Colo. State University, pp. 43.

Rodgers, C.D., (1967): The Use of Emissivity in Atmospheric Radiation Calculations. Quart. J. of the Roy. Met. Soc., 93, No. 395, 43-54.

Rodgers, C.D., C.D. Walshaw, (1966): The Computation of Infra-Red Cooling Rate in Planetary Atmospheres. Quart. J. Roy. Met. Soc., 92, 67-92.

Sargent, S.L., W.A. Beckman, (1973): A Numerical Model of Thermal Radiation in a Dusty Atmosphere. J. Atm. Sci., 30, 88-94.

Shaw, G.E., J.A. Reagan and B.M. Herman, (1973): Investigation of Atmospheric Extinction Using Direct Solar Radiation Measurements Made with a Multiple Wavelength Radiometer, J. App. Met., 12, 374-380.

SMIC, (1971): Study of Man's Impact on Climate, MIT-Press, pp. 308.

Stevenson, C.M., (1969): The Dust Fall and Severe Storms of 1 July, 1968, Weather, 24, 126-132.

Schutz, L., R. Jaenicke, (1974): Particle Number and Mass Distributions Above 10^{-4} cm Radius in Sand and Aerosol of the Sahara Desert. J. App. Met., 13, 863-870.

Steyer, T.R., Day, K.L. and Huffman, D.R. (1974): Infra-red Absorption by Small Amorphous Quartz Spheres. Appl. Opt., 13, 1586-1590.

Stowe, L.L., Jr., (1971): The Effects of Particulate Matter on the Radiance of Terrestrial Infrared Radiation. Institute of Geophys. and Plan. Physics. pp. 109.

Vittori, O., C. Tomasi, R. Guzzi, (1974): Dessen's Droplets in the Near and Middle Infra-Red Spectrum of the Sun, J. Atm. Sci., 31, 261-270.

Volz, F.E., (1957): Die Spektralene Eigenschaften der Dunstsubstanz - uv Absorption von Niederschlagswasser und der Dunsteinfluss auf die Langwellige Atmosphärische Strahlung, Ann. Met., 8, 34-39.

Volz, F.E., (1970): Spectral Skylight and Solar Radiance Measurements in the Caribbean: Maritime Aerosols and Sahara Dust, J. Atmos. Sci., 27, 1041-1047.

Volz, F.E. and L. Sheehan, (1971): Skylight and Aerosol in Thailand During the Dry Winter Season, App. Opt., 363-366.

Wang, W., G.A. Domoto, (1974): The Radiative Effect of Aerosols in the Earth's Atmosphere. J. App. Met., 13, 521-534.

Whitby, K.T. (1974): Modelling of Multi-modal Aerosol Distributions, Trans. Conf. G.A.F., Bad Goden, F.R.G., Oct. 17, 1974 (Preprint).

2-1 Heating Rates due to Desert Aerosols

2-1-a) General Discussion

The role of aerosols in the general circulation of the atmosphere and in climate has been the subject of extensive discussion. The problem of aerosols arises in two ways:

The first problem is the determination of the impact of aerosols on atmospheric and surface heating. The second problem is the determination of their indirect role on the energy balance of the atmosphere through their effect on the formation and the properties of clouds. We shall concern ourselves solely with the first problem.

2-1-b) Heating Rates for Numerical Models of the General Circulation

Random errors in heating-rates have little effect on General Circulation Models according to Joseph (1966), and Washington (1971). It is important, however, that the heating rate departs systematically from a suitable standard and that its trend is known. Systematic changes in radiative properties of the atmosphere have quite significant effects, see Joseph ibid, Fels and Kaplan (1974), Manabe and Wetherald (1975). For example, systematic perturbations of the heating rate greater than 0.5°K day^{-1} affect the NCAR G.C.M. according to Washington (1974).

An important requirement that any radiative heating rate scheme must satisfy to be useful in numerical modelling of the atmosphere is speed of computation. We address ourselves now to the development of fast and relatively accurate radiative transfer model to compute the heating rate of the desert aerosol in the atmosphere.

2-1-c) Heating Rates in the Solar Spectrum due to Aerosols

Several studies of solar heating due to aerosols are available in the literature e.g. Yamamoto et al., (1974), Dave and Braslau, (1974) and Braslau and Dave (1973, (a), (b)).

An important problem in modelling heating by an aerosol is the variation of its mixing-ratio with height in the atmosphere. This leads to the need for many layers in order to adequately model the variation of the albedo for single scattering with height.

A second problem is the spectral integration of fluxes and heating rates. The extinction of the aerosol usually decreases slowly with wavelength and it is small, in the appropriate spectral ranges, compared to the absorption by water-vapor and other gases' absorption bands. Rayleigh scattering is small compared to absorption in the solar infra-red. We therefore divide the solar spectrum into two regions. One contains the range .3 μm $< \lambda \leq$ .8 μm and all "windows" between gaseous absorption bands; aerosols are assumed to be optically active and Rayleigh scattering by molecules must also be considered. The second region is that of all gaseous absorption bands; there we assume that only gases are optically active.

2-2 The δ-Eddington Approximation

A simple model for atmospheric radiative heating rates due to the presence of aerosols will now be developed:

The direct use of the Eddington approximation in calculating solar fluxes and heating rates leads to large errors for optically thin aerosol laden atmospheres. The reason for this is that single-scattering is usually dominant due to the relatively small total optical depths, $\overset{*}{\tau} < 1$. In this case, the actual phase-function is strongly peaked, while the Eddington approximation assumes that the peak in the scattering function is relatively small. The Eddington phase function is

$$\frac{P(\theta)}{4\pi} \sim 1 + \omega_1 \cos\theta, \qquad 2\text{-}2,1$$

The forward to backward ratio is thus

$$R \equiv \frac{P(0°)}{P(180°)} \sim \frac{1 + \omega_1}{1 - \omega_1} \qquad 2\text{-}2,2$$

Van de Hulst (1971) showed that $\omega_1 = 3g$, where $g = \frac{1}{2}\int_{-1}^{1} P(\theta)\cos\theta \, d(\cos\theta)$ is the asymmetry factor. In the solar spectral range, $g \simeq .7$ for aerosols. Therefore, $R \simeq -2.8$ while its actual value may be of the order of a 1000 and positive.

This difficulty can be reduced if the forward peak of the phase function is replaced by a suitably weighted Dirac delta-function. The phase function can be approximated by:

$$P(\mu) = 4\pi f\delta(\mu - 1)\delta(\phi) + (1 - f)(1 + 3g'\mu) \qquad 2\text{-}2,3$$

where $\mu = \cos\theta$, f is a weighting factor defined below and g' is the asymmetry-factor of the truncated phase function.

The application of this approximation of the phase-function leads to a scaling of the optical depth, albedo for single scattering, and the asymmetry-factor

$$\tau' = (1 - \omega f)\tau$$

$$\omega' = \frac{1 - f}{1 - \omega f}\omega \qquad 2\text{-}2,4$$

$$g' = \frac{g - f}{1 - f}$$

The factor f may be found by

$$\text{Zero Moment:} \quad \int_{4\pi} \frac{P(\theta)}{4\pi} \, d\Omega \equiv 1 \qquad 2\text{-}2,5a)$$

$$\text{First Moment:} \quad \int_{4\pi} \frac{P(\theta)}{4\pi} \cos\theta \, d\Omega \equiv g = f + (1-f)g' \qquad 2\text{-}2,5b)$$

Then the second moment:

$$\int_{4\pi} \frac{P(\theta)}{4\pi} P_2(\cos\theta) d\Omega \equiv f \qquad 2\text{-}2,5c)$$

where $P_2(\cos\theta)$ is the second order Legendre polynomial.

Any phase-function may be approximated by a Henyey-Greenstein function. Van de Hulst (1971) showed that the Henyey-Greenstein function may be expressed as:

$$P(\theta) = \sum_{\ell=0}^{L} (2\ell + 1) g^{\ell} P_{\ell}(\cos\theta). \qquad 2\text{-}2,6$$

Therefore, it follows that

$$f = g^2 \qquad 2\text{-}2,7$$

We can derive fluxes from an Eddington approximation which employs the transformed quantities defined in Eqs. 2-2,4 and 2-2,7. The quantities I_o and I_1 are given by Shettle and Weinman, (1970).

$$I_o = C_1 \exp(-K\tau') + C_2 \exp(K\tau') - \alpha \exp(-\tau'/\mu_o) \qquad 2\text{-}2,8$$

$$I_1 = P[C_1 \exp(-K\tau') - C_2 \exp(K\tau')] - \beta \exp(-\tau'/\mu_o) \qquad 2\text{-}2,9$$

where

$$K = [\, 3(1 - \omega')(1 - \omega' g')]^{\frac{1}{2}}$$

$$P = [\, 3(1 - \omega')/(1 - \omega' g')]^{\frac{1}{2}}$$

$$\alpha = \frac{3\omega'\mu_o^2 \, [1 + g'(1 - \omega')]\hat{I}_o}{4\pi \, (1 - K^2\mu_o^2)}$$

$$\beta = \frac{3\omega'\mu_o \, [1 + 3g' \, (1-\omega')\mu_o^2] \, \hat{I}_o}{4\pi \, (1 - K^2\mu_o^2)}$$

The boundary conditions at the top and bottom of the layer (atmosphere) are

$$(1 + \frac{2P}{3})C_1 + (1 - \frac{2P}{3})C_2 = \alpha + \frac{2}{3}\beta \qquad 2\text{-}2,10$$

$$[1 - \bar{A} - \frac{2P}{3}(1 + \bar{A})]e^{-K\tau^{*}'} C_1 + [1 - \bar{A} + \frac{2P}{3}(1 + \bar{A})]e^{K\tau^{*}'} C_2 =$$

$$[(1 - \bar{A})\alpha - \frac{2\beta}{3}(1 + \bar{A}) + \frac{\bar{A}\mu_o \hat{I}_o}{\pi}]e^{-\tau^{*}'/\mu_o} \qquad 2\text{-}2,11$$

where $\bar{A}$ is the surface albedo, τ^{*}' is the optical depth at the surface and μ_o is the solar zenith angle.

The downward, $F\downarrow(\tau')$, and upward, $F\uparrow(\tau)$, fluxes are equal to

$$F\downarrow(\tau') = \mu_o \hat{I}_o \exp\{-\tau'/\mu_o\} + \pi(I_o + 2/3\ I_1) \qquad 2\text{-}2,12$$

$$F\uparrow(\tau') = \pi(I_o - 2/3\ I_1) \qquad 2\text{-}2,13$$

In order to test the accuracy of this method, the fluxes and flux differences were extensively compared to similar calculations using doubling method, see Hansen and Travis (1974). Table 2-1 shows sample comparisons for the most stringent demands on the δ-Eddington method, namely small optical depths, $\tau^* = .0282$ and $.282$, a surface albedo of zero and a range of solar zenith angles $1.0 > \mu_o > 0.2$. All fluxes and flux differences are given in units of the normal incidence solar incident flux at the top of the aerosol layer, $\tau = 0$.

The total downward flux, computed using the δ-Eddington approximation, is usually equal to that evaluated by the doubling method to two or three significant digits. The same can be said for the diffuse upward and the net fluxes. The net flux differences, which are proportional to the heating-rates at any level, indicate a systematic error in the δ-Eddington method.

Table 2-1 Comparisons Between Fluxes and Flux Differences Computed by the Doubling Method and the δ-Eddington Approximation

Aerosol Parameters	g = .670						a = .971				$\bar{A}$ = 0	
Total Optical Thickness	τ^* = .0282						τ^* = .282					
Cosine of Solar Zenith Angle μ_o	0.2		0.6		1.0		0.2		0.6		1.0	
Total Downward Flux	D.M.[1]	δ-E.[2]	D.M.	δ-E.	D.M.	δ-E.	D.M.	δ-E.	D.M.	δ-E.	D.M.	δ-E.
τ = 0	.2000	.2000	.6000	.6000	1.0000	1.0000	.2000	.2000	.6000	.6000	1.0000	1.0000
$\tau = \tau^*/2$	.1952	.1970	.5974	.5976	.9860	.9984	.1636	.1737	.5761	.5777	.9839	.9841
$\tau = \tau^*$	.1904	.1936	.5947	.5950	.9722	.9965	.1359	.1509	.5473	.5528	.9633	.9691
Diffuse Upward Flux												
τ = 0	.0088	.0057	.0045	.0043	.0026	.0027	.0569	.0428	.0434	.0395	.0275	.0271
$\tau = \tau^*/2$	.0045	.0030	.0023	.0023	.0014	.0014	.0246	.0199	.0243	.0209	.0150	.0150
$\tau = \tau^*$	.0000	.0000	.0000	.0000	.0000	.0000	.0000	.0000	.0000	.0000	.0000	.0000
Net Flux												
τ = 0	.1912	.1943	.5955	.5957	.9974	.9973	.1431	.1572	.5566	.5605	.9725	.9729
$\tau = \tau^*/2$	.1908	.1940	.5951	.5954	.9970	.9970	.1387	.1538	.5518	.5568	.9679	.9691
$\tau = \tau^*$	.1904	.1936	.5947	.5950	.9965	.9965	.1359	.1509	.5473	.5528	.9633	.9649
Net Flux Difference x 10^4												
0 : $\tau^*/2$	4.3	3.7	4.2	3.7	4.2	3.4	43.6	33.8	48.1	36.3	45.8	37.5
$\tau^*/2$: τ^*	4.0	3.8	4.2	3.8	4.2	5.0	28.4	45.3	45.3	40.0	45.8	42.5

(1) Doubling Method

(2) δ-Eddington Method

For the smallest optical depth considered, .0282, it is -15 percent and -11 percent for the upper and lower half of the aerosol layer respectively. In the case of an optical depth ten times larger, namely .282, the same errors are -22 percent and -7 percent respectively. The largest error among those enumerated above, namely -22 percent in the upper half of the aerosol layer with a total optical depth of .282, leads to an error in heating rate of $-.07°K\ day^{-1}$.

It is thus clear that the δ-Eddington method presented in this study is adequate for the calculation of monochromatic fluxes and heating rates in an absorbing and scattering layer of aerosol.

We now treat the parameterization of the monochromatic heating in an atmosphere containing absorbing and scattering aerosols embedded in an ambient Rayleigh-scattering atmosphere.

The scattering phase-function for the mixture of a Rayleigh-scattering molecules with a Mie-scattering aerosol, may be expressed by a weighted sum of the separate phase functions, see Deirmendjian (1969).

$$\bar{P}(\theta) \simeq \frac{s_a^{(h)}}{s_a^{(h)} + s_m^{(h)}} P_a(\theta) + \frac{s_m^{(h)}}{s_a^{(h)} + s_m^{(h)}} P_m(\theta) \qquad 2\text{-}2,14$$

where: $s_a^{(h)}$ is the scattering coefficient of the aerosol;

$s_m^{(h)}$ is the scattering coefficient of the molecules;

and: $P_a(\theta)$, $P_m(\theta)$ are the phase functions for the aerosol and molecules respectively.

The asymmetry factor of the mixture is:

$$\bar{g} = \frac{s_a^{(h)} g_a}{s_a^{(h)} + s_m^{(h)}} \qquad 2\text{-}2,15$$

Because:

$$g_m \equiv 0 \qquad 2\text{-}2,16$$

Consequently, the amount of energy scattered into the forward peak is:

$$\bar{f}(h) = g_a^2 \left(\frac{1}{1 + x(h)} \right)^2 \qquad 2\text{-}2,17a)$$

The albedo for single scattering of the composite medium is:

$$\bar{\omega}(h) = \frac{\bar{\omega}_a (1 + x(h))}{(1 + x(h)\bar{\omega}_a)} \qquad 2\text{-}2,17b)$$

$$x(h) = s_m^{(h)} / s_a^{(h)} \qquad 2\text{-}2.17c)$$

Where $\bar{\omega}_a$ is the albedo for single scattering of the aerosol. The molecular scattering coefficient $s_m^{(h)}$ is proportional to pressure:

$$s_m^{(h)} = s_m^{(o)} \exp \{- h/H_m\} \qquad 2\text{-}2,18$$

The height profile of the aerosol extinction coefficient may be approximated by an exponential profile with a scale height $H_a = 1.0$ km for the case considered by Dave (1975).

$$s_a^{(h)} = s_a^{(o)} \exp \{-h/H_a\} \qquad 2\text{-}2,19$$

We now parameterize this composite atmosphere by evaluating a pressure-weighted average albedo for single-scattering $\bar{\bar{\omega}}$ and asymmetry-factor $\bar{\bar{g}}$:

$$\bar{\bar{\omega}} = \int_0^\infty \bar{\omega}(h)\,\frac{P(h)}{P(o)}\,dh \Big/ \int_0^\infty \frac{P(h)}{P(o)}\,dh \qquad 2\text{-}2,20a)$$

$$\bar{\bar{g}} = g_a \int_0^\infty \frac{1}{1 + x(h)}\,\frac{P(h)}{P(o)}\,dh \Big/ \int_0^\infty \frac{P(h)}{P(o)}\,dh \qquad 2\text{-}2,20b)$$

These equations were evaluated in the two spectral regions 0.3 μm <λ< 0.8 μm and 0.8 μm <λ< 2.5 μm. Only in the first region is this correction of the scattering parameters of importance.

Table 2-2 summarizes the results of this approximation for the scattering parameters for comparison to Dave and Braslau's (1974) work. The molecular scattering coefficient at the surface was taken to be .019 km^{-1}

Table 2-2 The Effect of Molecular Scattering on an Aerosol Laden Atmosphere in Spectral Range 0.3 μm < λ < 0.8 μm.

Aerosol Only Dave C1 (1974)	Aerosol + Molecule
$\beta_a^{(o)} = .096\ km^{-1}$	$\beta_a^{(o)} + \beta_m^{(o)} = .115\ km^{-1}$
$\omega_a = .910$	$\bar{\bar{\omega}} = .978$
$g_a = .700$	$\bar{\bar{g}} = .143$
$f_a = .490$	$\bar{\bar{f}} = .021$

The results of this comparison are shown in Table 2-3.

Table 2-3 - Comparison of 6-Eddington Computations with Those of Dave (1974)

Solar Angle		.3 - .8 μm		.8 - 2.5 μm		.8 - 2.5 (Bands)			
θ_o (degrees)	μ_o	Net Flux Top ($w\text{-}m^{-2}$)	Net Flux Bottom ($w\text{-}m^{-2}$)	Net Flux Top ($w\text{-}m^{-2}$)	Net Flux Bottom ($w\text{-}m^{-2}$)	Net Flux Top ($w\text{-}m^{-2}$)	Net Flux Bottom ($w\text{-}m^{-2}$)	Total Absorption %	Total Absorption (Dave C1) %
		(a) Absorption, Surface Albedo = 0							
0	1	-717.1	-715.8	-64.8	-64.7	-527	-347	13	13
15	.966	-690.0	-688.7	-62.5	-62.4	-509	-334	13	13
30	.866	-610.8	-609.5	-56.0	-55.9	-465	-304	14	14
60	.500	-323.8	-322.6	-31.9	-31.8	-263	-153	16	17
80	.174	- 85.3	- 84.5	-10.4	-10.3	- 91	- 38	22	24
		(b) Absorption, Surface Albedo = .05							
0	1	-686.5	-685.1	-47.4	-47.2	-508.1	-341.0	12	14
80	.174	- 81.7	- 80.9	- 9.3	- 9.7	- 90.9	- 37.0	23	23
		(c) Absorption, Surface Albedo = .20							
0	1.	-592.0	-590.2	-51.8	-51.6	-525.6	-318.8	15	15
80	.174	- 70.6	- 69.7	- 8.7	- 8.6	- 91.0	- 35.0	24	25
		(d) Reflection, Surface Albedo = 0							
0	1.	82.6	799.7	.278	64.7	0.	527.6	5.	

Solar Angle		.3 - .8 μm		.8 - 2.5 μm		.8 - 2.5(bands)		Albedo	
θ_o (degrees)	μ_o	Flux Up Top ($w\text{-}m^{-2}$)	Flux Down Top ($w\text{-}m^{-2}$)	Flux Up Top ($w\text{-}m^{-2}$)	Flux Down Top ($w\text{-}m^{-2}$)	Flux Up Top ($w\text{-}m^{-2}$)	Flux Down Top ($w\text{-}m^{-2}$)	Rayleigh %	Present %	Dave (C1) %
		(e) Reflection, Surface Albedo = 0								
0	1.	82.6	799.7	.278	64.72	0.	527.6	5	6	5
15	.966	82.4	772.5	.294	62.52	0.	509.6	5	6	5
30	.866	81.8	692.6	.336	56.06	0.	456.9	6	7	6
60	.500	76.0	399.9	.483	32.36	0.	263.8	9	10	9
80	.174	53.5	138.9	.776	11.24	0.	91.6	17	22	21
		(f) Reflection, Surface Albedo = .05								
0	1.	113.2	799.7	17.3	64.7	14.5	527.6	9	10	8
80	.174	57.1	138.9	1.9	11.2	1.9	91.6	21	25	23
		(g) Reflection, Surface Albedo = .20								
0	1.	207.7	799.7	3.0	64.7	54.3	527.6	23	20	19
80	.174	147.6	138.9	2.6	11.2	6.0	91.6	33	32	30

Table 2-3(a) shows the results for three separate spectral ranges .3 μm <λ< .8 μm, .8 μm <λ< 2.5 μm between the gaseous absorption bands and .8 μm <λ< 2.5 μm in the gaseous absorption bands. Spectrally averaged net fluxes are expressed in units of watt/m^2, at the top of our atmosphere and at its bottom. From this set of data we calculate the total absorption in units of the incident solar flux to be compared with the exact results of Dave. The gaseous abosrption was modelled by fitting a "best-fit" curve to the absorptivity given by Dave (his Model B), as a function of the solar zenith angle. We used the water-vapor profile given by Dave. The resulting equation for the combined transmissivity of all absorbing gases in a Rayleigh scattering atmosphere for water-vapor amounts up to 6 g/cm^2 and for the whole solar spectrum, is

$$T\left(\frac{u^*}{\mu_o}\right) = .94 \quad \exp\left\{ - .063 \left(\frac{u^*}{\mu_o}\right)^{1/2} \right\} \qquad 2\text{-}2,21$$

where

$$u^*(h_1,h_2) = \int_{h_1}^{h_2} \rho_{water}^{(h)} \left(\frac{p(h)}{p(o)}\right) dh,$$

is the "reduced" water-vapor mass between two altitudes when the sun is at a zenith angle $\cos^{-1}\mu_o$. The transmitted intensity at a given height is

$$F\left(\frac{u^*}{\mu_o}\right) = \hat{I}_o \mu_o \quad T\left(\frac{u^*}{\mu_o}\right) \quad , \qquad 2\text{-}2,22$$

where the incident solar flux is that over the whole spectrum. This transmission function is similar to many other empirical equations derived in the literature, see e.g. Kondratiev (1972) except for being a transmissivity for the whole solar spectrum and the inclusion of the effect of Rayleigh scattering

on the absorption. It is interesting that a square-root dependence is found, even though we modelled the total absorption by all gases throughout the solar spectrum by just that of the water-vapor.

The last step in the approximation of absorption by gases is the assumption

$$\hat{I}_o \text{ (bands)}\mu_o \left(1 - T_{\text{bands}}\left(\frac{u^*}{\mu_o}\right)\right) = \hat{I}_o\mu_o\left(1 - T\left(\frac{u^*}{\mu_o}\right)\right) \qquad 2\text{-}2,23$$

or that the total energy, throughout the solar spectrum, absorbed by the gases may be thought of as being concentrated in the absorbing bands of water-vapor at .8 μm ≤ λ ≤ 2.5 μm.

The net fluxes in the water-vapor absorption bands are calculated with the help of Eq. 2-2,17 by using the following equations

$$F(\text{top})_{\text{bands}} = -\hat{I}_o(\text{bands})\mu_o\left[1 - T\left(\frac{u^*}{\mu_o}\right)T(1.67u^*)\bar{A}\right] \qquad 2\text{-}2,24a)$$

$$F(\text{bottom})_{\text{bands}} = -\hat{I}_o(\text{bands})\,\mu_o\,T\left(\frac{u^*}{\mu_o}\right)[1 - \bar{A}] \qquad 2\text{-}2,24b)$$

where $\bar{A}$ is the surface albedo and $\hat{I}_o(\text{bands}) = .4255\,\hat{I}_o$.

On comparing the last two columns in Table 2-3, (a), (b) and (c), it is seen that atmospheric absorption is accurate enough to be used in a general circulation model.

General circulation models also need fluxes at the top and bottom of the atmosphere to determine energy balances. We therefore also compare the reflection by the aerosol-molecular atmosphere with that of the

more exact results. The results are shown in parts (d),(e) and (f) of Table 2-3.

The application of this method yields albedos that are in good agreement with those obtained from more accurate models as is shown in the last two columns of Table 2-3 (d), (e) and (f).

The same ideas may be applied to the calculation of the downward flux at the surface. A comparison of the δ-Eddington approximation to the "global" flux at the surface with the "accurate" results is given in Table 2-4.

Table 2-4. The Downward Fluxes at the Surface in Units of $\mu_o \hat{I}$ - Comparison with Dave and Braslau (1974) and Dave (1975).

μ_o	$\bar{A}$	Dave Results : Transmission at Surface			Present Corrected Total Down
		Direct	Diffuse	Total	
1.000	0.0	.097	.723	.819	.810
.966		.099	.717	.816	.807
.866		.107	.698	.806	.803
.500		.152	.587	.739	.730
.174		.240	.313	.554	.551
1.000	0.05	.100	.723	.823	.811
.174		.243	.313	.556	.552
1.000	0.25	.112	.723	.835	.863
.174		.250	.313	.563	.544

The comparisons of our computations with more exact computation shown in Tables 2-2, 3 and 4 indicate that it is possible to describe the effect of aerosol on the solar heating rate of a clear atmosphere in a way that is simple, fast and with a predictable systematic error not larger than a few percent.

We now address ourselves to other physical errors in computing heating rates in an atmosphere containing a mixture of absorbers and scatterers throughout the solar spectrum. We defined three spectral intervals .3 μm < λ < -.8μm, .8 μm < λ < 2.5 μm between bands, and .8 μm < λ < 2.5 in bands, and averaged the effect of the Rayleigh atmosphere.

The division into two main spectral regions does not result in large errors, see Joseph (1966), (1971a),Lacis and Hanson (1974), and Dave (1975). The neglect of ozone in the troposphere is not serious. The vertical optical depth of ozone at λ≃0.6 μm, the center of the Chappuis band is of the order of .04 for normal ozone amounts (.384 atm-cm) and more than 90 percent of the ozone is above 10 km. The effect of ozone in the stratosphere on tropospheric fluxes may be modelled by decreasing the solar flux at the tropopause by the ozone transmission, see Joseph (1966).

Molecular scattering in the spectral region 0.8 μm < λ < 2.5 μm can be neglected because it is insignificant. The fact that we do not account for absorbers other than water-vapor in this latter spectral region does not lead to large errors, e.g. Figure 8 of Braslau and Dave (1973) and Table 2-3.

The neglect of the over-lap of the water-vapor and aerosol spectral characteristics in the spectral region .8 μm < λ < 2.5 μm will lead to errors of about 2% in the heating-rate. The error is due to the over-lap in the wings of the water-vapor bands and is small because there is little solar energy in this optical range.

The heating rate is evaluated directly through the use of

$$\frac{dF_n}{d\tau'} = 4\pi(1 - \omega') \left[I_o(\tau') + \frac{\hat{I}_o}{4\pi} e^{-\tau'/\mu_o}\right] \qquad 2\text{-}2,25$$

and

$$\frac{\partial T}{\partial t}(h, \mu_o, A) = -\frac{1}{\rho_m(h)} \frac{1}{c_p} \left(\frac{d\tau'}{d h}\right) \frac{dF_n}{d\tau'}(\tau', \mu_o, A) \qquad 2\text{-}2,26$$

The calculations of the heating-rate have been made by using an "average" optical depth, weighted by the solar spectrum, $\hat{I}_o(\lambda)$,

$$\bar{\tau} = \int_{.3\mu m}^{.8\mu m} \tau(\lambda)\, \hat{I}_o(\lambda) d\lambda \Big/ \int_{.3\mu m}^{.8\mu m} \hat{I}_o(\lambda) d\lambda \qquad 2\text{-}2,27a)$$

in the range 0.3 μm < λ < .8 μm, and

$$\bar{\tau} = \Sigma_i \int_{\Delta\lambda_i} \tau(\lambda) \hat{I}_o(\lambda) d\lambda \Big/ \Sigma_i \int_{\Delta\lambda_i} \hat{I}_o(\lambda) d\lambda \qquad 2\text{-}2,27b)$$

where the $\Delta\lambda$ are all spectral intervals in the solar spectrum between .8 and 2.5 μm where there is no gaseous absorption. (.80-.88, 1.00-1.10, 1.18-1.28, 1.52-1.68 μm).

Models of the general circulation are insensitive to errors in the heating-rates which are less than .5°K -day^{-1}, Washington (1974). The error in our approach is acceptable whereas the additional time required to rigorously compute the heating-rate in an atmosphere with two mixed scatterers would not permit the inclusion of aerosols in a model of the general circulation

2-3 The Atmospheric Heating Rate Models in the Solar Spectral Range for Application to G.C.M.'s and Climate Models.

The technique outlined in the previous section has been applied to models of the desert aerosol over land and over sea.

The optical characteristics at the surface are shown for a "normal" desert aerosol in Table 2-5 as used in our model.

Table 2-5. Optical Characteristics of "NORMAL" Desert Aerosols $\hat{I}_o$ = 1392 w/m^2, Solar Constant ($\delta\hat{I}_o/\hat{I}_o$) in percent.

$\Delta\lambda$ [μm]	.3-.4	.4-.5	.5-.6	.6-.7	.7-.8	.3-.8	.8-2.5
$\beta_a(0)$ [km^{-1}]	.230	.210	.196	.175	.155	.193	.055
ω	.934	.958	.970	.975	.976	.970	.920
g	.670	.670	.670	.670	.670	.670	.670
$\delta\hat{I}/\hat{I}$ (%)	7.8	14.4	13.8	11.8	9.6	57.4	42.6

Several model distributions with height of the desert aerosol were used and these are shown in Table 2-6.

Table 2-6: Desert Aerosol Distributions as a Function Height

Bottom [km]	Top [km]	Scale Height [km]	Notes
0	7.3	1.31	Overland - Normal
0	7.3	2.8	Overland - Dust Storm, Khamsin
2	5	∞	Over Ocean; *$\beta_a(h)$ = const

*This distribution is required as input for G.C.M.s; however, lidar parameters are computed from the overland normal model only.

The inclusion of the effect of Rayleigh scattering on the heating rates over land is similar to that applied to the aerosol model C1 of Dave.

The results are shown in Table 2-7 (a) for 0.3 μm < λ < 0.8 μm and should be compared to those in Table 2-5.

Table 2-7: Optical Characteristics of Atmosphere Containing Desert Aerosol

(a) Overland	Light (BF = .1)	Normal (BF = 1.)	Heavy (BF = 10.)
$\beta_a^{(o)} + \beta_m^{(o)}$ (km^{-1})	.038	.211	1.949
$\bar{\omega}$	.987	.974	.970
$\bar{g}$	.176	.491	.645
(b) Over sea (In layer)			
$\beta_a^{(o)} + \beta_m^{(o)}$ (km^{-1})	.031	.205	1.942
$\bar{\omega}$	.981	.972	.970
$\bar{g}$	.098	.153	.162

Note that BF is defined in section 1-2g).

The analysis of the desert aerosol aloft, in a layer between 2 and 5 km, involves the same averaging technique as before, but applied only in the layer itself. The results are shown in Table 2- 7 (b). The more difficult problem is the adaptation of the boundary conditions, in the δ-Eddington solution necessary to take into account the existence of Rayleigh scattering above and below the aerosol layer. This is handled in the following way:

The downward flux of solar radiation at the top of the aerosol layer at 5 km is modelled by

$$F\downarrow(5) \cong \hat{I}_o \mu_o \left[e^{-\tau_m(5)/\mu_o} + \frac{1 - e^{-1.66\tau_m(5)}}{2} \right] \qquad 2\text{-}3.1$$

$$= \hat{I}_o \mu_o \left[e^{-.07/\mu_o} + .05 \right]$$

where the solar flux incident on the atmosphere is decreased by the direct transmission, $e^{-\tau_m(5)/\mu}$, and enhanced by the diffuse transmission, $\frac{1 - e^{-1.66\tau_m(5)}}{2}$, through a Rayleigh atmosphere down to 5 km.

The lower boundary condition, now applied at 2 km, has to take into account the existence of the Rayleigh scattering between 0 and 2 km. The upward flux at 2 km is approximated by

$$F\uparrow(2) \cong [\mu_o \hat{I}_o \exp(-\tau'(2,5)/\mu_o) \{\exp(-\frac{\Delta\tau_m(0,2)}{\mu_o} + \frac{1 - e^{-1.66\Delta\tau_m(0,2)}}{2})\} \quad 2\text{-}3.2$$

$$+ \pi [I_o(2) + \frac{2}{3} I_1(2)] \{\frac{1 + e^{-1.66\Delta\tau_m(0,2)}}{2}\}] \cdot \bar{A} \cdot \{\frac{1 + e^{-1.66\Delta\tau_m(0,2)}}{2}\}$$

where $\hat{I}_o$, $I_o(2)$ and $I_1(2)$ include the corrected upper boundary condition (Equation 2-3.1) and $\Delta\tau_m(0,2)$ is the spectrally averaged vertical optical depth of the Rayleigh atmosphere between the surface and 2 km, namely .03, $\bar{A}$ is the surface albedo. An analysis of the first two expressions in curly brackets, involving $\Delta\tau_m$, shows that one may equate the two with an error of less than .03, and express the lower boundary condition by

$$F\uparrow(2) = F\downarrow(2) \quad (.975)^{2\bar{A}} \quad 2\text{-}3.3$$

$$A_{effective} \equiv (.975)^{2\bar{A}},$$

where $F\downarrow(2)$ is the downward flux at 2 km.

2-4 Results - Desert Aerosol Over Land

Atmospheric solar heating rates due to desert aerosols were evaluated as a function of height for various values of the solar zenith angle, and the surface albedo in each of the two spectral ranges (.3 μm < λ < .8 μm, .8 μm < λ < 2.5 μm). The height increments were 0.5 km and 1.0 km. The heating due to water-vapor in the same tropical atmosphere was also available, as was the total heating.

We shall only present a few examples of our results: Figure 2-1 compares the heating rates due to aerosol in the solar spectrum with that due to water-vapor. The atmospheric profiles of temperature and humidity

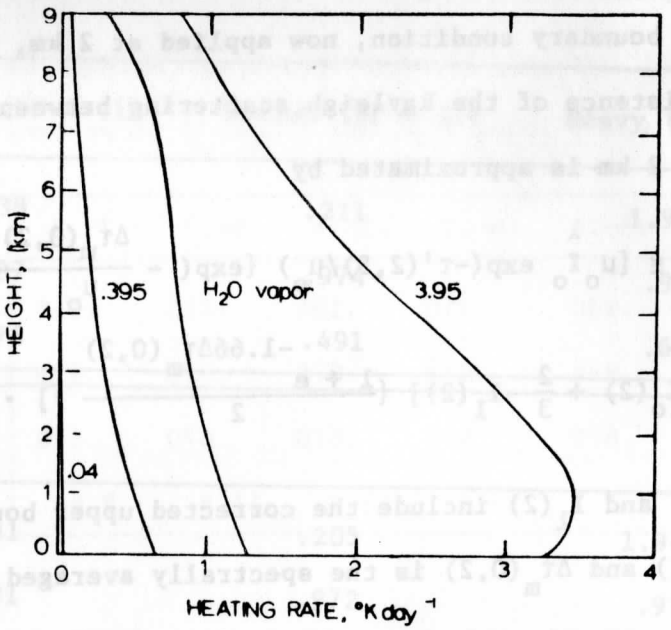

Figure 2-1. Comparison of solar heating rate due to aerosols with that due to absorption by water vapor in the interval 0.3 μm < λ < 2.5 μm. Water vapor absorption function is from Kondratiev (1972). Numbers identify the total optical thickness, τ*. Surface albedo, $\bar{A}$ = .15, μ_o = .6, H_a = 1.3 km.

are taken from Peterson (1968) and they are typical for a desert atmosphere over India. Increasing total amounts of desert aerosols are indicated by the optical depth, τ*, at the surface. The curve marked τ* = .395 is for an average amount of desert aerosol in a clear atmosphere. The average amount of desert aerosol leads to a heating that is about one half of that due to water-vapor at the surface and decreases with height due to the aerosol scale height, namely H_a = 1.3 km, which is for the desert aerosol over the Indian desert. A dense desert aerosol may have a vertical optical depth larger than one. The curve marked τ* = 3.95 illustrates probably the extreme effect of a desert aerosol. In the lower troposphere, the heating due to this amount of aerosol is much larger than that due to water-vapor and a peak in the heating rate develops aloft.

2-5 Desert Aerosol Layer Aloft in a Moist Tropical Atmosphere over the Ocean.

A layer of desert aerosol between about 2 and 5 km over the tropical Atlantic Ocean may significantly affect the transfer of solar radiation, the heating-rate profile, and the stability of the atmosphere. We have therefore modelled the effect of a desert aerosol layer aloft over the ocean. As an example of our results we show here in Figure 2-2 the results for a thin (BF = .1) and a normal (BF = 1.0) desert aerosol. The optically thin model aerosol, with an optical depth at λ = .5 μm of 0.06 has a constant mass-concentration of 30 $\mu g/m^3$ in the layer. For a normal desert aerosol, these quantities should be multiplied by a factor of 10. The ambient tropical atmosphere has a water content of 3.57 g/cm^2 and a mixing-ratio at the surface of .016 g/g.

It is seen that a thin desert aerosol layer aloft has only a minimal effect on the solar heating rate. A normal (BF = 1) desert aerosol increases the heating in the layer by more than .5°K day^{-1} at its bottom and by .83°K day^{-1} at its top. This is a very large change in heating, which will strongly affect atmospheric stability.

In Figure 2-2 Part (b) we compare our theoretical increase in solar heating due to the aerosol over an ocean with the difference between measured and calculated clear-air solar heating rates, as given by Reynolds et al (1973). Unfortunately, the measured data have a large scatter, and comparison of individual days is difficult. The comparison with our results shows that in the aerosol layer, the theoretical differences between the effect of layers containing 30, and a 300 $\mu g/m^3$ cover the measured differences (90 to 160 $\mu g/m^3$). It is seen that the experimental differences reach a maximum near 3 km where the presence of aerosol is usually detected. The difference below 2 km is near zero and in the lowest kilometers there is another relative maximum, which might be due to marine haze or sea-spray.

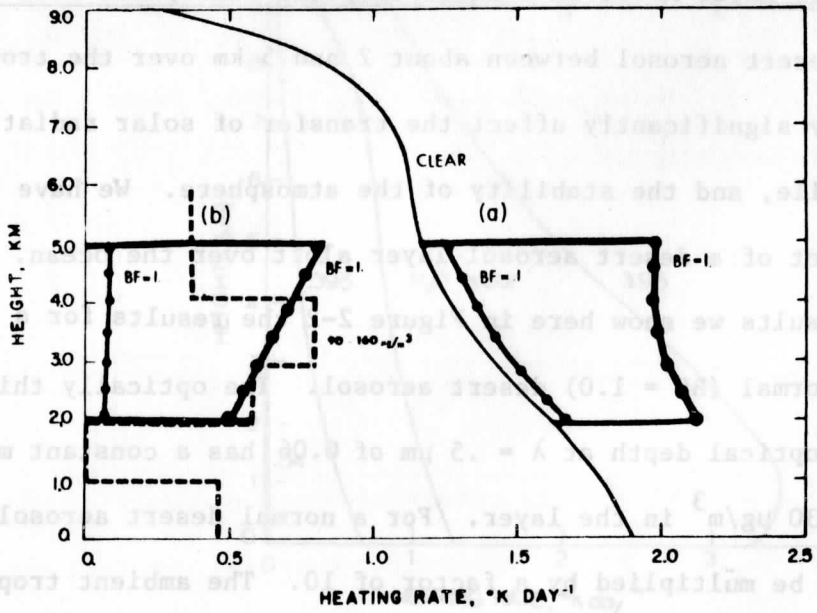

Figure 2-2. Solar heating profile for desert aerosol aloft over the ocean. (—·—·—) Computed BF = 0.1; $\tau(2)$ = .06, mass concentration 30 $\mu g/m^3$ BF = 1.0, $\tau(2)$ = .58, mass concentration 300 $\mu g/m^3$ (——). Tropical atmosphere [McClatchey et al. (1971)], $\bar{A}$ = 0.05, μ_o = 0.6. Part b: Difference between heating in Dusty and Clear Atmospheres. Mean of eight observed profiles, RMS error ± 0.5°K day^{-1} (---).

It thus seems that a desert aerosol aloft over the ocean may significantly affect the distribution of solar heating.

2-6 The Total Daily Solar Radiative Heating Over a Desert

The total daily solar heating over a desert is a quantity of interest for a model of desert climate or of the role of the desert in the general circulation of the atmosphere.

We modelled this quantity by integrating the solar heating of a typical desert over the hour angle of the sun for the case of a desert aerosol with a scale-height of 2.8 km distributed up to 400 mb in a clear atmosphere. The surface albedo was $\bar{A}$ = .25.

The results are shown in Table 2-8 for the dust, the water-vapor and for their sum for three different amounts (BF = .1, 1.0, 10.0).

For a thin layer (BF = .1), the heating due to water is dominant. A normal desert aerosol (BF = 1.0) will add approximately 50 percent of the heating due to water up to a height of three kilometers and be slightly less significant at higher levels. The very dense aerosol case described by BF = 10. will more than triple solar heating.

Table 2-8 . The Daily Solar Heating Rate Over a Desert (°K day^{-1})

ht (km)	H_2O Heating Rate	Aerosol Heating Rate BF = .1	BF = 1.0	BF = 10.	TOTAL (BF=.1)	TOTAL (BF=1.0)	TOTAL (BF=10.)
0	.63	.04	.33	1.65	.67	.96	2.28
.5	.60	.03	.28	1.22	.63	.88	1.82
1.0	.57	.03	.26	1.73	.60	.83	2.40
1.5	.54	.02	.23	1.68	.56	.77	2.22
2.0	.52	.02	.20	1.61	.54	.72	2.13
2.5	.49	.02	.18	1.52	.51	.67	2.01
3.0	.47	.02	.16	1.42	.49	.63	1.89
3.5	.45	.01	.14	1.30	.46	.59	1.75
4.0	.43	.01	.13	1.20	.44	.56	1.63
4.5	.41	.01	.11	1.09	.42	.52	1.50
5.0	.39	.01	.10	.98	.40	.49	1.37
5.5	.37		.09	.88	.37	.46	1.25
6.0	.35		.08	.79	.35	.43	1.14
6.5	.34		.07	.70	.34	.41	1.04
7.0	.32		.06	.63	.32	.38	.95
7.5	.30		.06	.57	.30	.36	.87
8.0	.27		.05	.50	.27	.32	.77
8.5	.22		.04	.45	.22	.26	.67
9.0	.14		.04	.40	.14	.18	.54

2-7 Heating Rates in the Thermal Infra-red Spectrum

2-7-a) Introduction

The calculation of heating rates in an absorbing, scattering and emitting atmosphere in the thermal infra-red poses some problems to the modeller. The main problem is that spectral fluxes and heating rates must be integrated over spectral regions in which the albedo for single scattering varies markedly, see Sargent and Beckman (1973) and Wang and Domoto (1974). Furthermore, the sources of radiation are both inside and outside of the medium. An additional consideration is that the treatment of the fluxes and heating-rate should be as close as possible to that accorded to absorbing gases, in order to avail one-self of the techniques developed over the years for treating the transmission of black-body radiation through the atmosphere. Our aim in this section is to develop a method of calculation that is adequate for use in a numerical model of the general circulation.

2-7-b) The Radiative Transfer Equation in the Thermal Infra-red Spectrum

The complete monochromatic radiative transfer equation in the thermal infra-red is

$$\frac{dI}{d\tau}(\tau, \mu, \phi) = I(\tau, \mu, \phi) - (1 - \omega(\tau))B(\tau)$$

$$- \frac{\omega(\tau)}{4\pi} \int_{4\pi} P(\mu, \phi; \mu', \phi')I(\tau, \mu', \phi')d\Omega' \qquad 2\text{-}7,1$$

where all parameters have the usual meaning and B is the local Planck source function.

The phase-function for aerosols in the thermal infra-red is somewhat peaked with an asymmetry factor $.2 < g_a < .6$, see Peterson & Weinman (1969), Deirmendjian (1969), and Sargeant & Beckman (1973). We shall again reduce the

problem to a more isotropic scattering case by removing the forward peak from the phase function in the manner described in section 2-2.

The radiative transfer equation is thus reduced to:

$$\mu \frac{dI}{d\tau'} = I - \frac{\omega'}{4\pi} \int_{4\pi} P'(\theta) I \, d\Omega' - (1 - \omega')B \qquad 2\text{-}7,2$$

where the albedo for single scattering and optical depth are redefined by Eqs. 2-2,4, and 2-2,7.

Table 2-9 shows typical values of the parameters ω' and τ' for three amounts of aerosol at λ = 8 μm and 11 μm.

Table 2- 9. Typical Values of the Reduced Optical Depth and Albedo for Single Scattering in a Humid Tropical Atmosphere

("top" of aerosol 400 km, scale height:2.8 km)

Pressure (mb)	Light λ=8μm		Light λ=11μm		Normal λ=8μm		Normal λ=11μm		Heavy λ= 8μm		Heavy 11μm	
	τ'	ω'	τ'	ω'	τ'	ω'	τ'	ω'	τ'	ω'	τ'	ω'
1000	1.25	.004	.78	.004	1.47	.040	.90	.033	3.13	.273	1.92	.216
920	.63	.005	.41	.005	.80	.051	.50	.042	2.04	.323	1.27	.250
840	.31	.009	.21	.0070	.43	.081	.28	.063	1.27	.42	.83	.311
760	.15	.014	.11	.010	.23	.122	.15	.089	.80	.509	.54	.366
680	.07	.024	.05	.016	.12	.189	.08	.130	.49	.597	.34	.420
600	.03	.042	.02	.026	.06	.282	.04	.184	.28	.666	.20	.464
520	.01	.074	.01	.043	.02	.400	.02	.253	.14	.716	.10	.498
440	.004	.132	.004	.072	.01	.525	.060	.334	.04	.748	.03	.523

Representative values for g' in the truncated phase function of the desert aerosol in the 8 μm < λ < 12 μm spectral "window" region are given in Table 2-10.

Table 2-10. Values of the Asymmetry Factor in the Infra-red Spectrum

$\Delta\lambda$(μm)	8.00	8.40	8.60	8.80	9.00	9.20	9.40	9.50	10.00	11.30	12.10	12.50
g'	.40	.16	.09	.04	.06	.06	.10	.12	.15	.27	.49	.17

It may be inferred, from the material in Table 2-10 that the truncated phase functions are nearly isotropic.

Sargeant and Beckman (1973) found that the heating rate, even at the surface, was in error by less than .1 out of 1.9°K day^{-1} if they assumed isotropic scattering. Their error decreased strongly in relative value with height for a quartz aerosol over the Indian desert.

For the sake of simplicity, we assume that the truncated phase function is isotropic, i.e. g' = 0. The aerosol is assumed here to be optically active only in the 8 - 12.5 μm region. Outside of this region, $\omega' \equiv 0$.

2-7-c) Solution of the Radiative Transfer Equation

The solution to Eq. 2-7,2 may be separated into two parts - one for the emitted intensity, I_e, and one for that scattered, I_s. Thus

$$I = I_s + I_e \qquad 2\text{-}7,3a)$$

$$\mu \frac{dI_e}{d\tau'} = I_e - (1 - \omega')B \qquad 2\text{-}7,3b)$$

$$\mu \frac{dI_s}{d\tau'} = I_s - \omega' J_o \qquad 2\text{-}7,3c)$$

For later reference let us also define

$$\mu \frac{dI_o}{d\tau'} = I_o - B \qquad 2\text{-}7,3d)$$

where $$J_o(\tau',\mu) = \frac{1}{2}\int_{-1}^{1} P(\mu, \mu')I(\tau', \mu')d\mu' \qquad 2\text{-}7,3e)$$

and $$I_o = I_e \ (\omega' \equiv 0) \qquad 2\text{-}7,3f)$$

The solutions to Eq. 2-7,3b) and 2-7,3d) are immediate, however the equation for the scattered intensity must be solved by an iterative process or by other numerical methods.

We have chosen to approximate the n-th order of scattering in the following way

$$I_{sn}(\tau',\theta) \cong \omega'^{n} I_e(\tau',\theta) \qquad 2\text{-}7.4$$

where $I_e(\tau',\theta)$ is the incident emitted intensity at level τ' from direction θ, Then the total scattered intensity is set equal to

$$I_s(\tau',\theta) = \sum_{n=0}^{\infty} \omega'^{n} I_e\ (\tau',\theta) \cong I_e \frac{(\tau',\theta)}{1-\omega'} \qquad 2\text{-}7.5$$

The equation of transfer for the scattered intensity thus becomes

$$\frac{dI_s}{d}(\tau',\mu) = I_{s\,(\tau',\mu)} - \frac{\omega'}{2}\int_{-1}^{1} I(\tau',\mu')d\mu' = I_s - \frac{\omega'}{(1-\omega)}\ J_o(\tau') \qquad 2\text{-}7.6$$

$$\text{where } J_o(\tau') \equiv \frac{1}{2}\int_{-1}^{1} I_e(\tau',\mu')d\mu' \qquad 2\text{-}7.7$$

The solutions for the upward, $I_s\uparrow$, and downward, $I_s\downarrow$, scattered intensities are

$$I_s^{\uparrow}(\tau',\mu) = \int_{\tau'}^{\tau^*} \frac{\omega'(t')}{1-\omega'(t')}\ J_o(t')e^{-(t'-\tau')/\mu}\ \frac{dt'}{\mu} \qquad 2\text{-}7.8a$$

$$I_s^{\downarrow}(\tau',-\mu) = \int_{0}^{\tau'} \frac{\omega'(t')}{1-\omega'(t')}\ J_o(t')e^{-(\tau'-t')/|\mu|}\ \frac{dt'}{|\mu|} \qquad 2\text{-}7.8b$$

The corresponding fluxes are

$$F_s^{\uparrow}(\tau') = 2\pi \int_{\tau'}^{\tau^*} \frac{\omega'(t')}{1-\omega'(t')} J_o(t')E_2(t'-\tau')dt' \qquad 2\text{-}7.8c$$

$$F_s^{\downarrow}(\tau') = 2\pi \int_{0}^{\tau} \frac{\omega'(t')}{1-\omega'(t')} J_o(t')E_2(\tau'-t')dt' \qquad 2\text{-}7.8d$$

The net flux

$$F_n(\tau') = F_s^{\uparrow}(\tau') - F_s^{\downarrow}(\tau')$$

The function J_o may be expressed

$$2J_o(\tau') = B(\overset{*}{\tau}')\, E_2(\overset{*}{\tau}'-\tau') + \int_{\tau'}^{\tau^*} J(t')E_1(|t'-\tau'|)dt + \int_{0}^{\tau'} J(t')E_1(|\tau'-t'|)dt \qquad 2\text{-}7.9$$

where $J(t') = (1-\omega'(t'))B(t')$

The numerical treatment of $J_o(\tau')$ is accomplished in the following manner:

The main contribution to the integral is from the layers very close to τ itself, due both to the variation in $J(\tau)$ and of $E_1(t-\tau)$. The function $J(\tau)$ varies much more slowly with distance from τ than $E_1(t-\tau)$. We shall therefore approximate the integrals in $J_o(\tau)$ by putting $J(t)$ equal to $J(\tau)$ and removing it from underneath the integral sign. Making use of the relations $E_1(x) = -\frac{dE_2(x)}{dx}$, and $2E_2(x) \cong \delta e^{-\delta x}$, where $\delta = 1.67$, the diffusivity

factor, one then gets for $J_o(\tau)$,

$$J_o(\tau) \simeq \frac{\overset{*}{B}\,\delta}{2} e^{-\delta(\tau_G'-\tau')} + (1-\omega'(\tau'))B(\tau')\left[1 - \frac{\delta}{2}\left(e^{-\delta(\overset{*}{\tau}'-\tau')} + e^{-\delta\tau'}\right)\right] \qquad 2\text{-}7.10$$

The first term represents the surface intensity $\overset{*}{B}$, singly scattered, reaching level τ, the second represents the intensities reaching level τ from the atmosphere below and above level τ, respectively.

2-7-d) Simple Approximation to the Scattering Term

An even simpler approximation to the scattering source function term, $\omega' J_o(\tau')$, may be based on an analysis of the ratio, R, between the scattering source function term, and the source function for emission, $(1 - \omega'(\tau'))B(\tau')$. where:

$$R(\tau') = \omega'(\tau')\{\, 1 + \frac{\delta}{2}\left[e^{-\delta(\overset{*}{\tau}' - \tau')}\left(\frac{\overset{*}{B}}{B}\,\frac{1}{(1-\omega'(\tau'))} - 1\right) - e^{-\delta\tau'}\right]\} \qquad 2\text{-}7.11$$

On substituting representative values for the parameters,

$$1 \le \overset{*}{\tau}' \le 3$$

$$.1 \le \omega'(\tau') \le .8$$

$$.5\overset{*}{B} \le B(\tau') \le \overset{*}{B} ,$$

one finds that

$$R(\tau') = g(\tau')\omega'(\tau')$$

where

$$.8 < g(\tau') < 2.3$$

and $g(\tau')$ is a function of τ' that may be empirically determined.

The complete equation of transfer may be approximated by

$$\mu \frac{dI}{d\tau'}(\tau',\mu) \cong I(\tau',\mu) - (1 - g(\tau')\omega'(\tau))\,(1 - \omega'(\tau'))B(\tau') \qquad 2\text{-}7.12$$

2-7-e) The Integrations with Respect to Height and Wave-Number

Several schemes were tested for use in the integration with respect to height. It was found that an integration in the optical depth, τ, in 26 steps of equal intervals using Simpson's rule gave numerical accuracies of the order of .1 percent in the fluxes. The fluxes were then interpolated parabolically in order to arrive at values for the fluxes at fixed pressures from the surface in 40 mb steps.

The spectral cooling rates at wave number, ν, are evaluated by use of the following equation

$$\frac{\partial T_\nu}{\partial t} = 8.64 * 10^4 \frac{g}{c_p P_o} \frac{\partial F_{n,\nu}(\tau(P))}{\partial (P/P_o)} = 8.34 \times 10^{-6} \frac{\partial F_{n,\nu}(\tau(P))}{\partial (P/P_o)} \quad ^\circ K \text{ day}^{-1} \qquad 2\text{-}7.13$$

The flux divergences are computed numerically.

The integration over the spectrum between 800 and 1250 cm^{-1}, the spectral region where we introduce the desert aerosol, is done numerically using the trapezoidal rule. The results of this integration are then added to those of the non-gaseous atmosphere in other spectral ranges, to obtain the total heating rate.

2-7-f) Comparison of Infra-red Heating Rates with Previous Computations

We now test our approach by comparing our fluxes and heating-rates for a quartz aerosol to those found by Sargeant and Beckman (1973). The latter evaluated theoretically the i.r. heating due to a quartz aerosol embedded in a tropical desert atmosphere over Rajasthan, India. Temperature, humidity and aerosol profiles were all measured by Peterson (1968) on April 24, 1966 over New Delhi as was the total mass.

The comparison is shown for the heating rates in Figure 2-3. The difference in the heating rates for the clear atmosphere between the previous and present results is due almost entirely to the different models for spectral gaseous absorption used. In the previous study of the effect of quartz aerosols it was assumed that in regions of weak gaseous absorption, one could neglect the latter compared to the effect of the quartz aerosol. A comparison of the aerosol and gas optical depths as given in Table 2-11, shows that one should not neglect the gaseous absorption in the "window" regions.

In the present study, we did not neglect the gaseous absorption and most importantly took into account the so-called e-type absorption, supposedly due to dimers, see Cox(1973). This leads to an increase in cooling near the surface and to the relative maximum between 950 and 850 mb. This change in the heating-rate profile is also reflected in the heating of our dusty atmosphere. The relative minimum in the cooling near 800 mb in the dot-dashed curve is due in part to the rapid decay of the effect of e-type absorption of the water-vapor and in part to the presence of the aerosol. The profile of the composite albedo for single-scattering is very different from that of the aerosol alone which is constant with height. These are the reasons that the previous authors could not reproduce this behavior of the heating rate profile, which is shown by the profiles measured by Bryson et. al.(1964), Peterson (1968), and by de Luisi (1975).

At the higher levels, where the effect of water-vapor abosrption is small, our results over-lap those of Sargeant and Beckman and both merge with the cooling of a clear atmosphere above 400 mb.

When we neglect the gaseous absorptions in the 8.0 μm < λ < 12.5 μm region, we get for quartz a curve (dashed in Figure 2-3), which is very close to that of the previous study. This shows that under the same assumptions, our method gives the same result as that of Sargeant and Beckman.

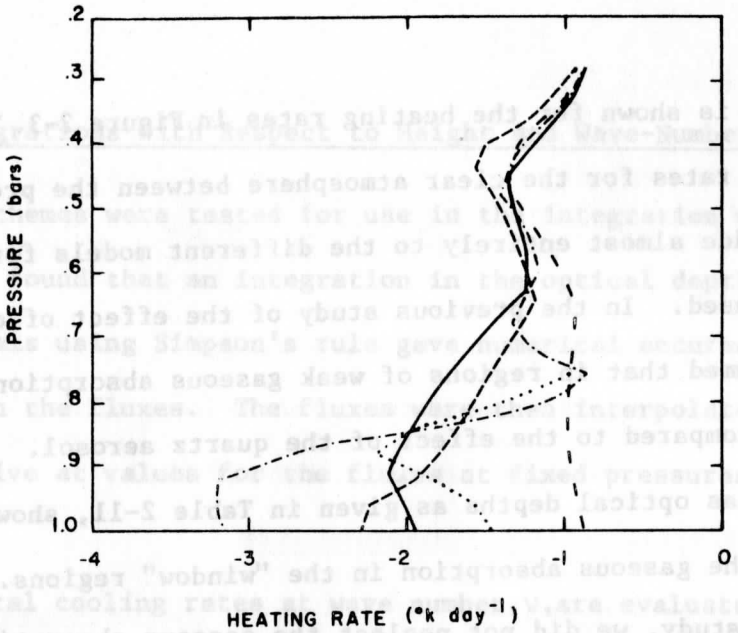

Figure 2-3 Comparison of aerosols on thermal infra-red heating rates found by Sargeant and Beckman (1973). (– –) gaseous absorbers only. (· · ·) gaseous absorption, with e-type water vapor absorption. (———) quartz from Sargeant and Beckman. (— — —) quartz present analysis, no gaseous absorption for 8.0 μm < λ < 12.5 μm_o (— · —) desert aerosol: BF = 1.

Table 2-11. The Optical Depths at the Surface of a "Normal" Atmosphere Containing Desert Aerosols and of the Gaseous Absorbers.

Wavelength [μm]	Aerosol	Gases
8.0	.34	.38
8.6	.29	.30
8.8	.32	.28
9.2	.29	.24
9.4	.28	.25
9.6	.30	.27
9.8	.28	.29
10.2	.22	.24
10.8	.17	.26
11.4	.15	.28
11.6	.12	.29
12.0	.11	.31

The remaining smaller differences between the two models for quartz are due to our different treatment of the forward peak. The previous study assigned the area under the phase-function between $\cos\theta = .75$ and $\cos\theta = 1$ to the forward peak, while we used g^2 for this area. The areas at a wavelength of 10 μm are .40 in the present case and .46 previously. Secondly, we assign a best-fit scale height H_a = 2.8 kilometers and a cut-off at 400 mb to the height-distribution instead of the actual distribution. Thirdly, we assume that the aerosol effect may be neglected outside of the spectral window of water-vapor between $8.0\ \mu m \leq \lambda \leq 12.5\ \mu m$.

In summary then it may be said that our method of computation compares well with the previously described method when applied to the same data.

2-7-g) Infra-red Heating Rates in a Desert Aerosol Layer Aloft Over the Ocean

We have modelled the effect on thermal infra-red heating rates of a desert aerosol overlying a tropical ocean in a layer between 2-5 km. This is close to the situation existing from late spring to late summer over the tropical Atlantic Ocean. The amounts or masses of aerosol that we have used are close to those which have been observed for the light and normal cases (BF = .1 - 30 $\mu g/m^3$ $\beta_a(.5\ \mu m) = .019$; BF = 1. - 299 $\mu g/m^3$, $\beta_a(.5\ \mu m) = .193$) in the Western Atlantic. The heavy desert dust (BF = 10.) may occasionally be found over the eastern tropical Atlantic off the coast of Africa. The heating rates caused by this latter aerosol constitute an upper limit on the possible effects of the desert aerosol.

Figure 2-4 shows the location of the layer between 2 and 5 km. The full line and the dotted line show the cooling in a clear tropical atmosphere with and without e-type absorption, showing the possible importance of this effect in the lowest 200 mb of this humid atmosphere. A thin aerosol

(BF = .1) will reduce cooling by about .1 to .2°K day^{-1} below the aerosol layer and in its lower part, and by about the same amount of additional cooling in the upper-part of the layer. The normal case (BF = 1.) will reduce cooling up to 1°K day^{-1} below 750 mb and increase it up to .75°K day^{-1} in the upper levels of the dust layer. A heavy dust fall (BF = 10) will have a very large effect on the heating rate, leading to strong heating around 800 mb and large cooling in the upper part of the dust layer.

In every case, the resulting cooling profile would lead to a stabilization.

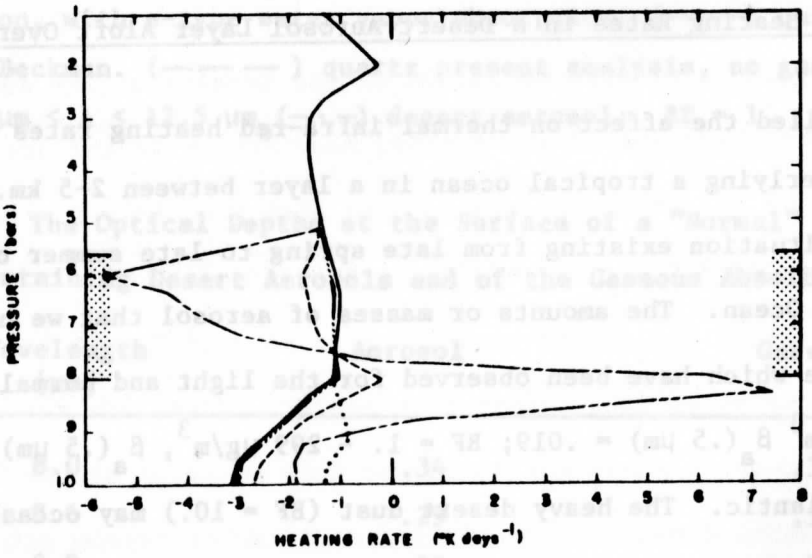

Figure 2-4 Infra-red heating rates for an aerosol cloud over the ocean Desert aerosol aloft between 2 and 5 km indicated by shading. Tropical atmosphere, McClatchey (1971). (——) gaseous absorbers only. (•••) gaseous absorbers only without e-type absorption for water vapor. (—•••—) BF = 0.1 light desert aerosol. (---). BF = 1.0 normal desert aerosol. (— - - —) BF = 10 heavy desert aerosol.

2-8 The Total, Solar and Infra-red, Heating Rates

Combining the considerations presented in sections 2-6 and 2-7 yields the total heating rate due to solar and infra-red radiation. These computations are applied to vertical aerosol distributions described by the parameters cited in Table 2-6.

2-8-a) Desert Aerosol Over Land

Figure 2-5 shows the total daily heating, evaluated for three amounts (BF = .1, 1., 10.) of desert aerosol over New Delhi using the atmospheric and aerosol profiles for April 24, 1966 measured in the evening by Peterson (1968), and for a surface albedo of .25. Most of the effect of the aerosol is to be found in the lowest 3 kms of the atmosphere in the case of a light and a normal desert aerosol. The main result of the presence of a light aerosol is an increase in cooling between 2 and 3 km of the order of .5°K day^{-1}. A normal aerosol will strongly reduce the cooling between .5 and 3 kms by 1.5°K day^{-1} and slightly increase it by .25°K day near the surface. A very large amount of dust will lead to strongly increased cooling near the surface, strong heating between 1 and 4 kms and reduced cooling all the way to 10 kms, leading to a stabilization process.

The average cooling per day for the atmospheric column between 0-10 km is -1.68°K day^{-1} in the clear atmosphere and -1.86, -1.41 and -.18°K day for the case of a light, a normal and a heavy aerosol, respectively. The results show that it is dangerous to make generalized predictions about the effect of aerosols on atmospheric heating. One must take into account not only the surface albedo and the amount of aerosol, but also its vertical distribution and the amounts of the absorbing gases.

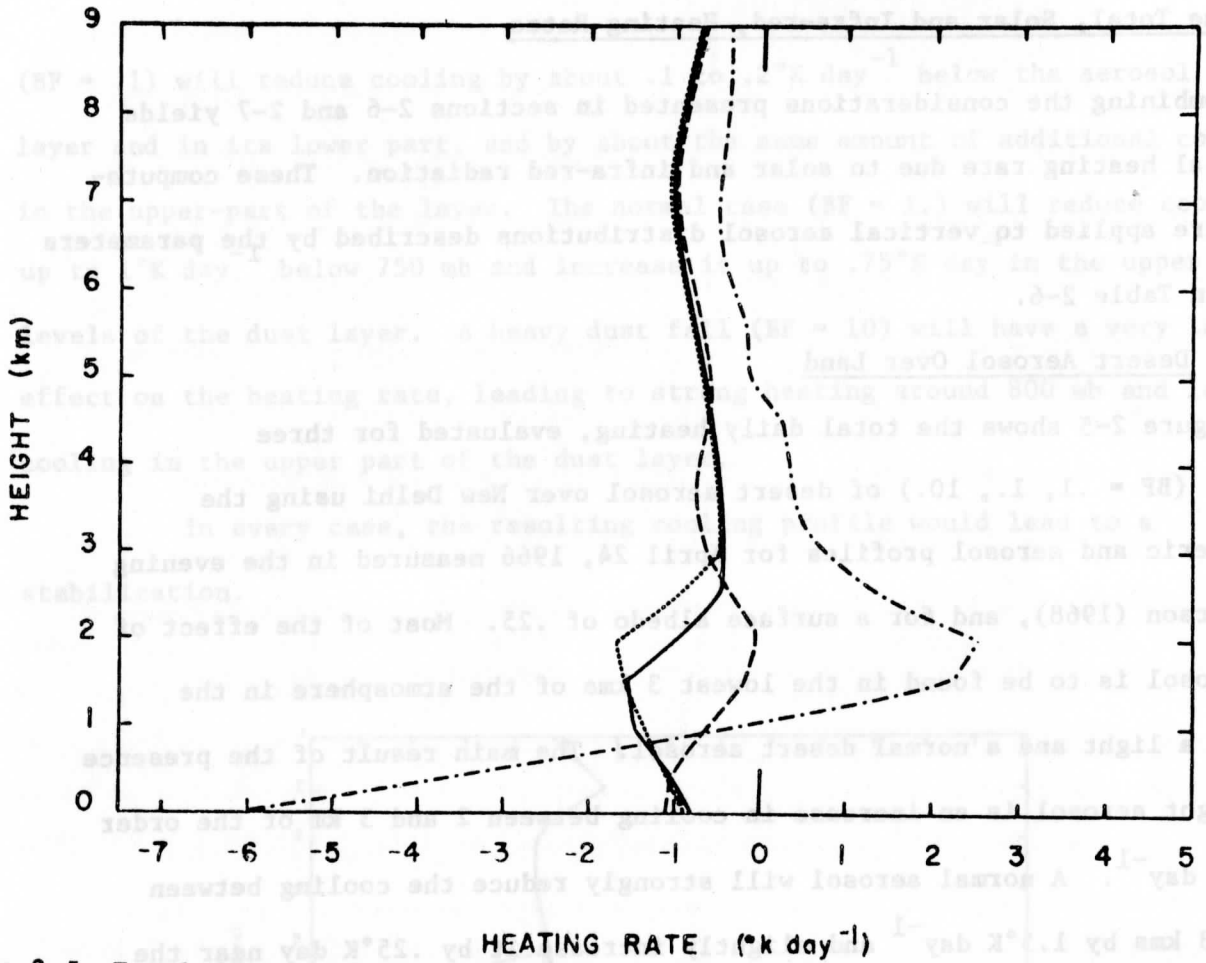

Figure 2-5 Total daily heating rate profile over a desert. New Delhi, April 24, 1966. $\bar{A}$ = 0.25, H_a = 2.8 km (——) clear atmosphere. (••••) BF = 0.1, light aerosol (——) BF = 1.0, normal aerosol. (— • —) BF = 10, heavy aerosol.

2-8-b) Desert Aerosol Over Ocean

Figure 2-6 shows the results of similar calculations for the case of a desert aerosol aloft between 2 and 5 kms overlying a tropical ocean with a surface albedo of .05. Again, the effect of a light (BF = .1) aerosol is small (.15 - 2°K day^{-1}) but systematic. A normal desert aerosol has a much larger effect. The daily cooling is reduced by .5°K day^{-1} in the lowest km, there is an actual heating of .9°K day^{-1} at the bottom of the aerosol layer and a broad increase of cooling of about .4°K day^{-1} in the upper part of the aerosol layer.

The daily cooling from the ocean surface to the bottom of the aerosol layer is $-1.45°K\ day^{-1}$ in the clear case, $-1.36°K\ day^{-1}$ for a light aerosol and $-.78°K\ day^{-1}$ for the normal case. Inside the dust layer itself, the change in cooling is small -.91, -.83, $-.89°K\ day^{-1}$ for the light, normal and heavy aerosol loads respectively. The important effect thus seems to be the reduction in cooling below the dust layer and in the latter's lower part.

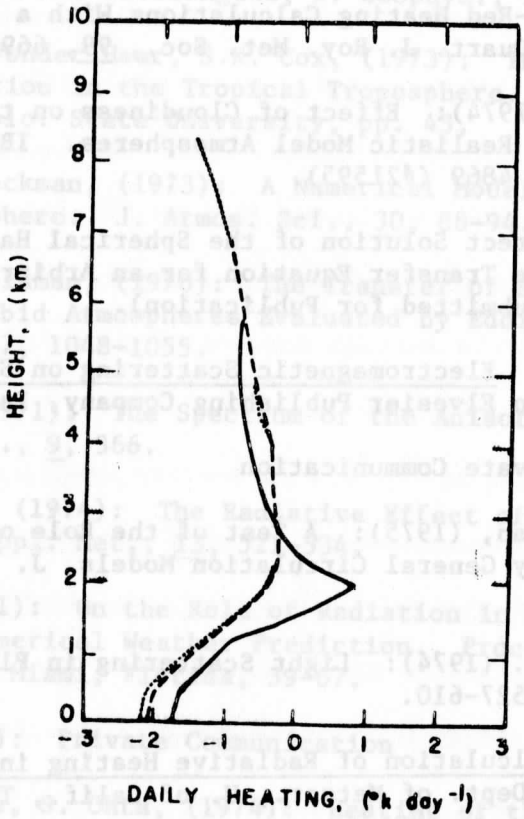

Figure 2-6 Total daily heating rate profile over the ocean. An aerosol layer between 2 and 5 km is designated by shading (••••) clear atmosphere, (---) BF = 0.1 light aerosol. (——) BF = 1.0 normal aerosol.

It is of great interest to measure the aerosol concentration in those regions of the atmosphere where one might expect heating rates that are different by $.5°K\ day^{-1}$ from those of the clear atmosphere. Such measurements can in principle be achieved by a Shuttle-borne lidar.

References, Chapter 2

Braslau, N., J.V. Dave, (1973a): Effect of Aerosols on the Transfer of Solar Energy Through Realistic Model Atmospheres. Part I: Non-Absorbing Aerosols, J. Appl. Met., 12, 601-615.

Braslau, N., J.V. Dave, (1973b): Effect of Aerosols on the Transfer of Solar Energy Through Realistic Model Atmospheres. Part II: Partly Absorbing Aerosols, J. Appl. Met., 12, 616-619.

Bryson, R.A., C.W. Wilson, and P. Kuhn, (1964): Some Preliminary Results From Radiation Sonde Ascents Over India, Proc. Symp. Trop. Met., Rotorua, New Zealand, 5-13 Nov. 1963, N.Z. Met. Service, 507-516.

Cox, S.K., (1973): Infra-Red Heating Calculations With a Water Vapour Pressure Broadened Continuum Quart. J. Roy. Met. Soc., 99, 669-679.

Dave, J.V., N. Braslau, (1974): Effect of Cloudiness on the Transfer of Solar Energy Through Realistic Model Atmospheres. IBM Thomas J. Watson Research Center. RC 4869 (#21595).

Dave, J.V., (1975): A Direct Solution of the Spherical Harmonics Approximation of the Radiative Transfer Equation for an Arbitrary Solar Elevation, Part II - Results (Submitted for Publication).

Deirmendjian, D., (1969): Electromagnetic Scattering on Spherical Polydispersions, American Elvesier Publishing Company, Inc., pp. 290.

de Luisi, J. (1975): Private Communication

Fels, S.B., and L.D. Kaplan, (1975): A Test of the Role of Long Wave Radiative Transfer by General Circulation Models, J. Atmos. Sci., 32, 779-789.

Hansen, J.E., Travis, L.D. (1974): Light Scattering in Planetary Atmospheres Space Sci. Rev. 16, 527-610.

Joseph, J.H., (1966): Calculation of Radiative Heating in Numerical General Circulation Models, Dept. of Meteor., U. of Calif., Tech. Report No. 1, pp. 84.

Joseph, J.H., (1971a): "On the Calculation of Solar Radiation Fluxes in the Troposphere." Solar Energy, 13, 7-16.

Joseph, J.H., (1971b): Thermal Radiation Fluxes Near the Sea Surface in the presence of Marine Haze. Isr. J. Earth Sci., 20, 7-12.

Kondratiev, K. Ya., (1972): Radiation Processes in the Atmosphere, W.M.O. Monograph 309.

Lacis, A.A., J.E. Hansen, (1974): A Parameterization for the Absroption of Solar Radiation in the Earth's Atmosphere, Atmos. Sci., 31, pp. 118-133.

Manabe, S., R.T. Wetherald, (1975): The Effects of Doubling the CO_2 Concentration on the Climate of a General Circulation Model. J. Atmos. Sci., 32, 3-15.

McClatchey, R.A., R.W. Fenn, J.E.A. Selby, J.S. Garing, F.E. Volz, (1971): Optical Properties of the Atmosphere, Envi. Res. Papers, 31, A.F.C.R.L., pp. 85.

Peterson, J.T., (1968): Measurement of Atmospheric Aerosols and Infra-Red Radiation Over Northwest India and Their Relationship. UW-Wis., Technical Report No. 38, pp. 165.

Peterson, J.T., J.A. Weinman, (1969): Optical Properties of Quartz Dust Particles at Infra-Red Wavelengths, J. Geophys., Res., 74, 6947-6952.

Reynolds, D.W., T.H. Vonder Haar, S.K. Cox, (1973): The Effect of Solar Radiation Absorption in the Tropical Troposphere. Atmosph. Science Paper No. 210, Colo. State University, pp. 43.

Sargent, S.L., W.A. Beckman, (1973): A Numerical Model of Thermal Radiation in a Dusty Atmosphere. J. Atmos. Sci., 30, 88-94.

Shettle, E.P., J.A. Weinman, (1970): The Transfer of Solar Irradiance Through Inhomogeneous Turbid Atmospheres Evaluated by Eddington's Approximation. J. Atmos. Sci., 27, 1048-1055.

Van de Hulst, H.C., (1971): The Spectrum of the Anisotropic Transfer Equation. Astron. Astrophys., 9, 366.

Wang, W., G.A. Domoto, (1974): The Radiative Effect of Aerosols in the Earth's Atmosphere. J. Appl. Met., 13, 521-534.

Washington, W.M., (1971): On the Role of Radiation in Dynamical Climate Simulation and Numerical Weather Prediction., Proc. Remote Sensing Workshop 29-31 March 1971, Miami, Florida, 39-67.

Washington, W.M. (1974): Private Communication

Yamamoto, G., M. Tanaka, S. Ohta, (1974): Heating of the Lower Troposphere Due to Absorption of the Visible Solar Radiation by Aerosols. J. Met. Soc. of Jpn., 52, 61-68.

3-0 Sensitivity Requirements for the Determination of Desert Aerosols from a Shuttle-borne Lidar

We will address ourselves to the determination of the accuracy with which the aerosol extinction coefficient must be measured and the vertical resolution with which such measurements must be determined. It may be recalled from the discussion in section 2-1,b) that G.C.M.s are insensitive to heating rate perturbations less than 0.5°K day^{-1}. The aerosol concentration must therefore be determined so that the computed heating rate profiles are defined within those tolerances. The Shuttle-borne lidar will measure profiles of the aerosol extinction coefficient; we assume that such measurements are obtained at $\lambda = 0.5$ μm and that these profiles are uniquely related to aerosol concentration as predicted by the aerosol model defined in Ch. 1.

The aerosol extinction at $\lambda = 0.5$ μm and the accuracy required to stay within the heating rate tolerances were computed as a function of altitude. Although 0.5°K day^{-1} is a tolerable heating rate uncertainty for a G.C.M., we also present results for 0.2°K day^{-1} perturbation. We will show in Ch. 4 that the present state of technology can yield extinction coefficient profiles which are consistent with heating rates defined within 0.5°K day^{-1}. The advance of technology may render it feasible to define heating rates within 0.2°K day^{-1} by the time that the Shuttle is launched; the corresponding extinction coefficients are therefore also presented for that case.

Calculated heating rate profiles are presented as a function of altitude for various aerosol models characterized by parameters cited in Table 2-5. Results are presented for aerosol profiles characterized by scaling factors BF = 0, 0.1, 1, 5 and 10. It is noteworthy that BF = 1 and 5 are similar to the clear and hazy tropical model atmospheres of McClatchey et al. (1971).

These models yield visible ranges at the surface of 22 and 4.5 km. respectively. Although results for total and solar heating rates are presented for various aerosol models in Tables 3-1 and 3-2, the analysis of Ch. 4 will be confined to the BF = 1 and 5 cases.

We carried out another test in order to determine whether a resolution of 1 km in the determination of the extinction coefficient will change the atmospheric heating rate, by more than .2°K day. An example of our results is shown in Fig. 3-1. Part (a) of the Figure shows the heating rates in the solar visible spectrum (.3 μm < λ < .8 μm) for the cases of a light, a normal and a heavy desert aerosol (BF = .1, 1 and 10 respectively). Part (b) of the same Figure shows the error in degrees per day when the average heating rate in successive layers of 1 km thickness is applied at the center of each layer. The error, as typified by the difference between the average heating rate in a one km layer and the actual heating rate at the mid-point of the layer, is larger than 2 percent only very near to the surface for a normal and a heavy desert aerosol. The largest absolute value of the error is only .055°K day^{-1}. It seems therefore that a resolution of one km in the lidar measurements is adequate for the determination of the extinction coefficient with an accuracy that is required by the G.C.M.s.

References: Chapter 3

McClatchey, R.A., R. W. Fenn, J.E.A. Selby, F.E. Volz and J.S. Garing (1971) Optical Properties of the Atmosphere (revised) Env. Res. Papers, 71, AFCRL pp.

Table 3-1-a) Change in β_a at λ = 0.5 μm to Produce a Change of .2°K day^{-1} in Total Daily Heating in a Dusty Atmosphere

Height [km]	BF = 0			BF = .1			BF = 1			BF = 5			BF = 10		
	$\frac{\partial T}{\partial t}$	β_a	$\lvert\Delta\beta_a\rvert$	$\frac{\partial T}{\partial t}$	β_a	$\lvert\Delta\beta_a\rvert$	$\frac{\partial T}{\partial t}$	β_a	$\lvert\Delta\beta_a\rvert$	$\frac{\partial T}{\partial t}$	β_a	$\lvert\Delta\beta_a\rvert$	$\frac{\partial T}{\partial t}$	β_a	$\lvert\Delta\beta_a\rvert$
0	- .87	0	.19	- .83	.020	.05	-1.09	.19	.08	-4.55	.97	.13	-6.03	1.93	1.93
1	- 1.48	0	.20	-1.31	.014	.14	- .57	.14	.06	- .37	.70	.43	- .21	1.35	.88
2	- .98	0	.01	-1.25	.009	.01	- .03	.09	.02	+1.73	.45	.09	+2.53	.94	.19
3	- .48	0	.10	- .48	.007	.06	- .63	.07	.06	+ .35	.35	.13	+ .74	.66	.17
4	- .53	0	.05	- .58	.005	.05	- .70	.05	.04	- .30	.15	.05	+ .32	.46	.14
5	- .66	0	.07	- .62	.003	.03	- .63	.03	.03	- .33	.10	.11	- .12	.33	.20
6	- .90	0	.04	- .89	.002	.02	- .82	.02	.03	- .68	.08	.05	- .36	.23	.14

Notes

Atmos: New Delhi April 24, 1966
Surface Albedo = .25
Scale Height of Desert Aerosol H_a = 2.8 km
Top of Aerosol Layer at 400 mb or 6.7 km

Table 3-1-b) Change in β_a at λ = 0.5 μm to Produce a Change of .5°K day^{-1} in Total Daily Heating in a Dusty Atmosphere.

Height [km]	BF = 0			BF = .1			BF = 1			BF = 5			BF = 10		
	$\frac{\partial T}{\partial t}$	β_a	$\lvert\Delta\beta_a\rvert$	$\frac{\partial T}{\partial t}$	β_a	$\lvert\Delta\beta_a\rvert$	$\frac{\partial T}{\partial t}$	β_a	$\lvert\Delta\beta_a\rvert$	$\frac{\partial T}{\partial t}$	β_a	$\lvert\Delta\beta\rvert$	$\frac{\partial T}{\partial t}$	β_a	$\lvert\Delta\beta_a\rvert$
0	- .87	0	.22	- .83	.020	.19	-1.09	.19	1.1	-4.55	.97	.25	-6.03	1.93	.45
1	-1.48	0	.04	-1.31	.014	.69	- .57	.14	.08	- .37	.70	4.30	- .21	1.35	1.38
2	- .98	0	.04	-1.25	.009	.02	- .03	.09	.11	+1.73	.45	.23	+2.53	.94	.43
3	- .48	0	.19	- .48	.007	.18	- .63	.07	.10	+ .35	.35	.33	+ .74	.66	.58
4	- .53	0	.25	- .58	.005	.21	- .70	.05	.13	- .30	.15	.19	+ .32	.46	.46
5	- .66	0	.20	- .62	.003	.20	- .63	.03	.30	- .33	.10	.45	- .12	.33	1.15
6	- .90	0	2.90	- .89	.002	2.90	- .82	.02	10.00	- .68	.08	10.00	- .36	.23	.74

Notes

Atmos: New Delhi April 24, 1966
Surface albedo = .25
Scale height of desert aerosol H_a = 2.8 km
Top of aerosol layer at 400 mb or 6.7 km

Table 3-2-a) Change in β_a at λ = 0.5 μm to Produce a Change of .2°K day^{-1} in Solar Heating in a Dusty Atmosphere.

Height [km]	BF = 0			BF = .1			BF = 1			BF = 5			BF = 10		
	$\frac{\partial T}{\partial t}$	β_a	$\lvert\Delta\beta_a\rvert$	$\frac{\partial T}{\partial t}$	β_a	$\lvert\Delta\beta_a\rvert$	$\frac{\partial T}{\partial t}$	β_a	$\lvert\Delta\beta_a\rvert$	$\frac{\partial T}{\partial t}$	β_a	$\lvert\Delta\beta_a\rvert$	$\frac{\partial T}{\partial t}$	β_a	$\lvert\Delta\beta_a\rvert$
0	1.26	0		1.34	.020	.09	1.92	.19	.03	3.93	.97	.15	4.82	1.93	1.35
1	1.13	0		1.18	.014	.08	1.66	.14	.02	3.75	.70	.11	4.58	1.35	1.01
2	1.03	0		1.08	.009	.06	1.44	.10	.02	3.33	.45	.08	4.26	.95	.88
3	.94	0		.98	.007	.06	1.26	.07	.02	3.13	.35	.07	3.79	.66	.94
4	.85	0		.88	.005	.05	1.10	.05	.03	2.17	.15	.04	3.24	.46	.07
5	.78	0		.80	.003	.03	.98	.03	.03	1.88	.10	.03	2.74	.33	.05
6	.70	0		.72	.003	.05	.86	.02	.02	1.65	.08	.02	2.28	.23	.04

Notes

μ_o = .6

θ_o = 53°

Table 3-2-b) Change in β_a at λ = 0.5 μm to Produce Change of .5°K day^{-1} in Solar Heating in a Dusty Atmosphere.

Height [km]	BF = 0			BF = .1			BF = 1			BF = 5			BF = 10		
	$\frac{\partial T}{\partial t}$	β_a	$\lvert\Delta\beta_a\rvert$	$\frac{\partial T}{\partial t}$	β_a	$\lvert\Delta\beta_a\rvert$	$\frac{\partial T}{\partial t}$	β_a	$\lvert\Delta\beta_a\rvert$	$\frac{\partial T}{\partial t}$	β_a	$\lvert\Delta\beta_a\rvert$	$\frac{\partial T}{\partial t}$	β_a	$\lvert\Delta\beta_a\rvert$
0	1.26	0	.10	1.34	.020	.13	1.92	.19	.13	3.93	.97	.64	4.82	1.93	.35
1	1.13	0	.14	1.18	.014	.14	1.66	.14	.11	3.75	.70	.31	4.58	1.35	.56
2	1.03	0	.11	1.08	.009	.11	1.44	.10	.07	3.33	.45	.18	4.26	.95	.18
3	.94	0	.08	.98	.007	.08	1.26	.07	.06	3.13	.35	.16	3.79	.66	.29
4	.85	0	.07	.88	.005	.06	1.10	.05	.08	2.17	.15	.08	3.24	.46	.24
5	.78	0	.05	.80	.003	.05	.98	.03	.03	1.88	.10	.08	2.74	.33	.23
6	.70	0	.04	.72	.003	.04	.86	.02	.03	1.65	.08	.08	2.28	.23	.55

Notes

μ_o = .6

θ_o = 53°

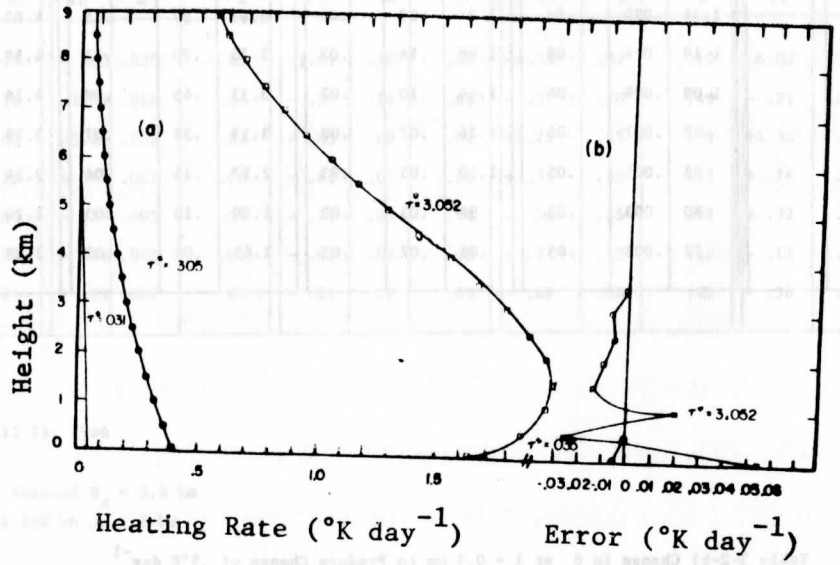

Figure 3-1: (a) Heating rates due to desert aerosol in the solar spectral region .3 - .8 μm. $\tau^* = .031$ - BF = .1; $\tau^* = .305$ - BF = 1.0; $\tau^* = 3.052$ - BF = 10. Surface albedo = .25; Cosine of solar zenith angle = .6; Aerosol Scale Height = 2.8 km.

(b) Difference between heating-rates averaged over layers of 1 km thickness and the heating rates at the mid-point of the layer in degrees per day.

4-0 Lidar Methods to Measure Aerosol Profiles - Introduction

The criteria required to define the spatial distributions of tropospheric aerosols for input into atmospheric general circulation models were identified in Tables 3-1 and 3-2. We will now describe several schemes in which lidar configurations are used to measure the spatial distribution of aerosol optical depth. Error analyses and model atmospheric calculations are presented in an effort to ascertain whether these schemes can provide spatial distributions of aerosol optical depth from Shuttle missions.

4-1 General Discussion of Expected Lidar Signals

4-1-a) Generalized Lidar Equation

The lidar equation for the number of photons collected by the receiver telescope due to single backscattering from a horizontally homogeneous atmosphere in the presence of J distinct extinction components β_j (j = 1, J) at an angle θ to the vertical is

$$\frac{2}{c}\frac{dN_j(x)}{dt} = \frac{E_o A_r}{hc\sigma}\frac{\mathbb{P}_j(\pi)}{4\pi}\frac{\beta_j \cdot \omega_j}{\sec^2\theta \cdot x^2}\exp\left(-2\sec\theta\int_o^x \sum_{j'=1}^{J}\beta_{j'}\,dx'\right) \qquad 4\text{-}1,1$$

where x = equivalent vertical path length as measured from the lidar platform

c = speed of light

E_o = energy of optical output

$hc\sigma$ = photon energy, where $\sigma = 1/\lambda$ is the optical wavenumber and h is Planck's constant

A_r = receiver area

$\omega_j = s_j/(s_j + a_j)$ = albedo for single scattering, where s_j and a_j denote extinction due to scattering and absorption, respectively

$\frac{P_j(\pi)}{4\pi}$ = normalized backscattering phase function and

$\beta_j = s_j + a_j$ = the extinction coefficient of the jth component.

$P_j(\pi)$ and β_j are general functions of equivalent vertical path length x.

The geometry of Eq. 4-1,1 is shown in Figure 4-1.

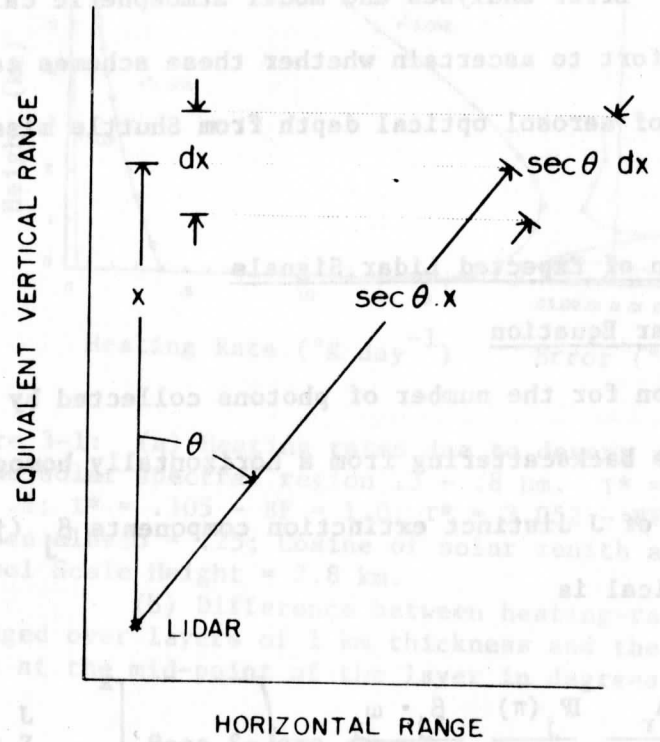

Figure 4-1 Lidar equation geometry for the case of a horizontally homogeneous atmosphere.

A lidar detection system integrates this signal over a finite time interval $\tilde{\Delta t}$, so that the number of singly scattered photons collected by the receiver telescope from the equivalent vertical range x_o to $x_o + u$ is

$$N_j(x_o,u) = \int_{x_o}^{x_o + u} \frac{2}{c} \frac{dN_j(x)}{dt} \sec\theta \, dx \qquad 4\text{-}1,2$$

$$= \frac{E_o A_r}{hc\sigma \sec\theta} \int_{x_o}^{x_o + u} \frac{\mathrm{I\!P}_j(\pi)}{4\pi} \frac{\beta_j \omega_j}{x^2} \exp\left(-2\sec\theta \int_o^{x_o} \sum_{j'=1}^{J} \beta_{j'} dx' \right) dx$$

where $u = \frac{c\tilde{\Delta t}}{2 \sec\theta}$. The number of photons collected by the receiver telescope $\frac{dN_j(x)}{dt}$ is approximately constant in the range interval u if u is sufficiently small. Equation 4-1, 2 then reduces to the more common form

$$N_j(x_o, u) = \frac{E_o A_r \, u}{hc\sigma \sec\theta} \frac{\mathrm{I\!P}_j(\pi)}{4\pi} \frac{\beta_j \omega_j}{x_o^2} \exp\left(-2\sec\theta \int_o^{x_o} \sum_{j'=1}^{J} \beta_{j'} dx' \right) \qquad 4\text{-}1,3$$

This chapter presents investigations of lidar returns from an atmosphere composed of Rayleigh (molecular) and Mie (aerosol) scatterers, which are referred to by the subscripts m and a, respectively.

4-1-b) Lidar Returns from a Model Atmosphere

Lidar returns are presented for a downward viewing lidar using the Clear and Hazy Tropical atmospheres of McClatchey et al. (1971). Example height profiles of β_m and β_a for two Tropical model atmospheres at 4880Å are plotted in Figure 4-2. The height profiles of β_a for the cases of Clear and Hazy model atmospheres differ only in the lowest 5 km.

Figures 4-3a and 4-3b present lidar returns from the McClatchey Clear and Hazy Tropical model atmospheres, respectively, for a lidar platform height h_o of 185 km. The lidar platform is located at a height of 185 km to simulate a Shuttle borne lidar system. The returns are given in units of photons per millijoule output at the wavelengths 3371, 4880 and 6238Å. The returns are

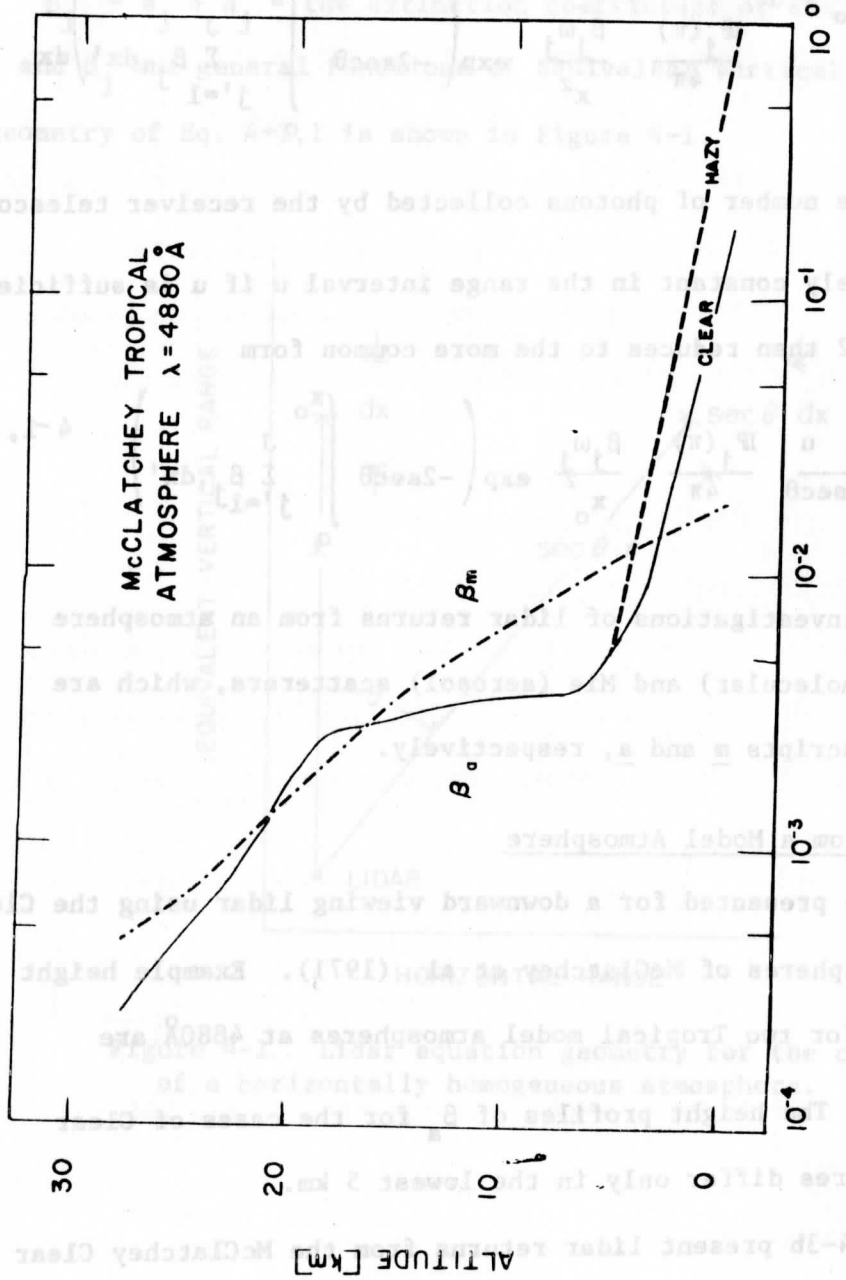

Figure 4-2 Height profiles of β_m and β_a, from the Clear and Hazy Tropical atmospheres of McClatchey et al. (1971) at 4880 Å.

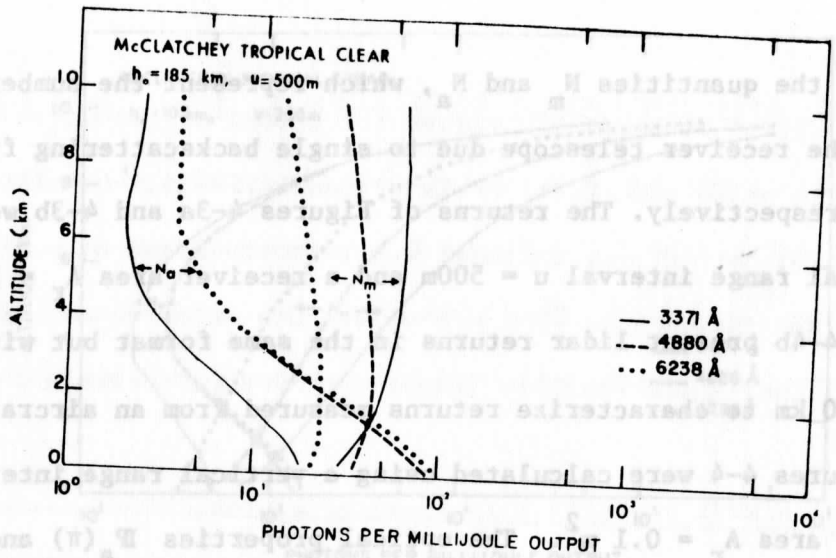

Figure 4-3a Lidar returns N_m and N_a from the Clear Tropical model atmosphere of McClatchey et al. (1971) at 3371, 4880, and 6238 Å. The lidar platform is located at a height of 185 km to simulate a Shuttle-borne lidar system. The receiver area $A_r = 1.0\ m^2$.

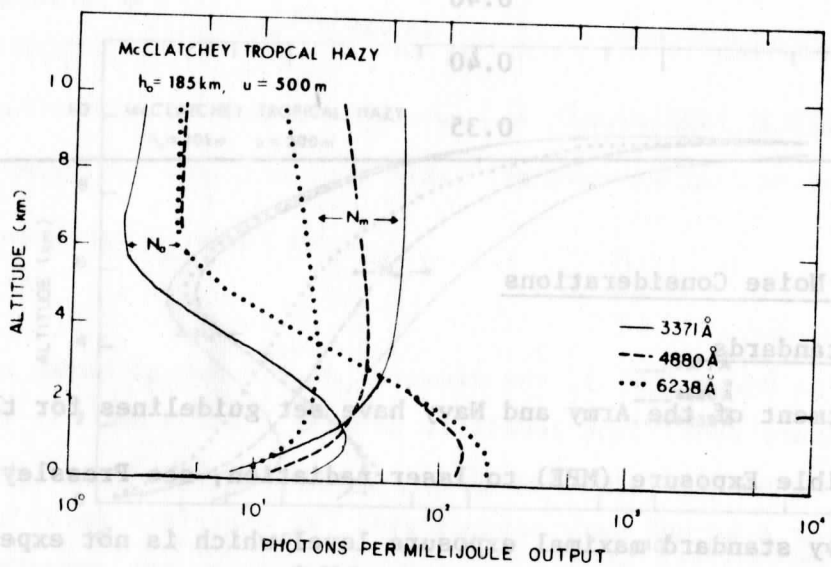

Figure 4-3b Lidar returns N_m and N_a from the Hazy Tropical model atmosphere of McClatchey et al. (1971) at 3371, 4880, and 6238 Å. The lidar platform is located at a height of 185 km to simulate a Shuttle-borne lidar system. The receiver area $A_r = 1.0\ m^2$.

separated into the quantities N_m and N_a, which represent the number of photons collected by the receiver telescope due to single backscattering from molecules and aerosols, respectively. The returns of Figures 4-3a and 4-3b were calculated using a vertical range interval u = 500m and a receiver area $A_r = 1.0\ m^2$. Figures 4-4a and 4-4b present lidar returns in the same format but with a platform height h_o of 10 km to characterize returns measured from an aircraft. The returns of Figures 4-4 were calculated using a vertical range interval u = 200m and a receiver area $A_r = 0.1\ m^2$. The optical properties $\mathbb{P}_a(\pi)$ and ω_a used for these calculations are given in Table 4-1.

Table 4-1 The Model Atmosphere Properties $\mathbb{P}_a(\pi)$ and ω_a for Figures 4-3 and 4-4

Wavelength	$\mathbb{P}_a(\pi)$	ω_a
3371 Å	0.40	1.0
4880 Å	0.40	1.0
6238 Å	0.35	.98

4-2 Signal and Noise Considerations

4-2-a) Safety Standards

The Department of the Army and Navy have set guidelines for the Maximum Permissible Exposure (MPE) to laser radiation, see Pressley (1971). The Army and Navy standard maximal exposure level which is not expected to cause detectable ocular injury (measured at the cornea) is about 1×10^{-7} j cm^{-2} for a Q-switched laser at all wavelengths between 0.4 and 1.5 μm. A safety factor of 2 is recommended for use in field evaluation.

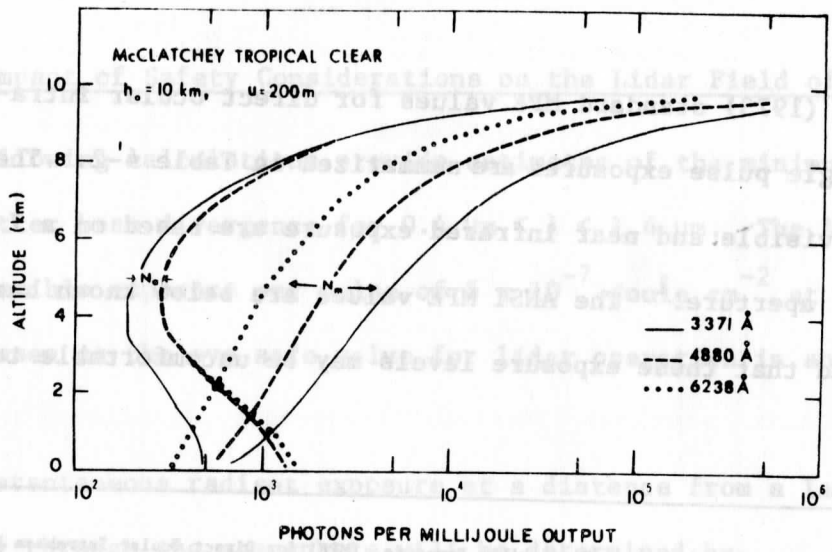

Figure 4-4a Lidar returns N_m and N_a from the Clear Tropical model atmosphere of McClatchey et al. (1971) at 3371, 4880, and 6238 Å. The lidar platform is located at a height of 10 km to simulate an aircraft-borne lidar system. The receiver area $A_r = 0.1\ m^2$.

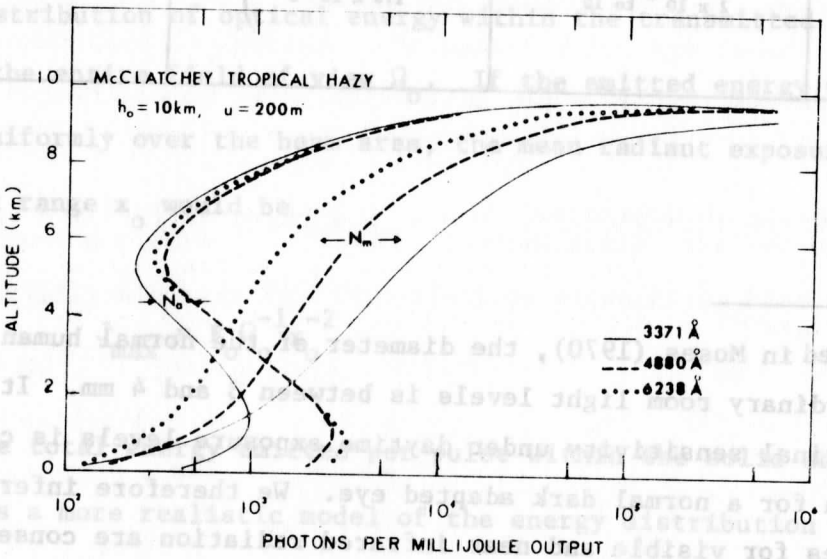

Figure 4-4b Lidar returns N_m and N_a from the Hazy Tropical model atmosphere of McClatchey et al. (1971) at 3371, 4880, and 6238 Å. The lidar platform is located at a height of 10 km to simulate an aircraft-borne lidar system. The receiver area $A_r = 0.1\ m^2$.

The ANSI (1973) standard MPE values for direct ocular intra-beam viewing of single pulse exposures are summarized in Table 4-2. The ANSI standards for visible and near infrared exposure are based on a 7 mm diameter limiting aperture.[1] The ANSI MPE values are below known hazard levels, yet it is noted that these exposure levels may be uncomfortable to view.

Table 4-2 The ANSI (1973) Maximum Permissible Exposure (MPE) for Direct Ocular Intrabeam Viewing

Wavelength $\lambda(\mu m)$	Exposure time t(sec)	MPE J_o(joule cm^{-2})	Notes
.32 to .40	10^{-2} to 10^{3}	1.	1 mm limiting aperture (in no case shall the total irradiance, over all wavelengths within the UV region, be greater than 1 watt cm^{-2})
.40 to 1.4	10^{-9} to 2×10^{-5}	5×10^{-7}	7 mm limiting aperture
	2×10^{-5} to 10	$1.8 \times 10^{-3} t^{3/4}$	

[1] As stated in Moses (1970), the diameter of the normal human adult pupil under ordinary room light levels is between 3 and 4 mm. It is further noted that retinal sensitivity under daytime exposure levels is considerably less than for a normal dark adapted eye. We therefore infer that the ANSI MPE values for visible and near infrared radiation are conservative for daytime laser exposure in the outdoor environment. However, the ANSI Standard section 8.5.1 states that no corrections are to be made for the intrabeam viewing MPE when the limiting aperture (pupil) size differs from 7 mm.

4-2-b) The Impact of Safety Considerations on the Lidar Field of View

The following calculations provide estimates of the minimum allowable laser transmitter beam divergence for 0.4 μm < λ < 1.4 μm. The ANSI (1973) maximum permissible exposure per pulse of 5×10^{-7} joule cm^{-2} at the Earth's surface is chosen as the eye safe value for lidar operation in an outdoor environment.

The instantaneous radiant exposure at a distance from a laser transmitting energy through the atmosphere will be determined by

1) atmospheric attenuation due to scattering and absorption,

2) the distribution of optical energy within the transmitted beam,

and 3) atmospheric scintillation, which cause random and possibly hazardous radiant exposure maxima.

Atmospheric attenuation can be neglected for the purpose of obtaining a worst case estimate of surface radiant exposures.

The distribution of optical energy within the transmitted beam is not uniform over the entire field of view Ω_o. If the emitted energy were distributed uniformly over the beam area, the mean radiant exposure per pulse J_{max} at range x_o would be

$$J_{max} = E_o \Omega_o^{-1} x_o^{-2} \qquad 4\text{-}2,1$$

where E_o is the total energy emitted per pulse within the solid angle Ω_o. The Gaussian is a more realistic model of the energy distribution within the beam area, see Figure 4-5. The Gaussian energy distribution $E(\zeta)$, where ζ is the half-angle from the transmitter optic axis, is specified by the requirement that the full beam divergence is that solid angle

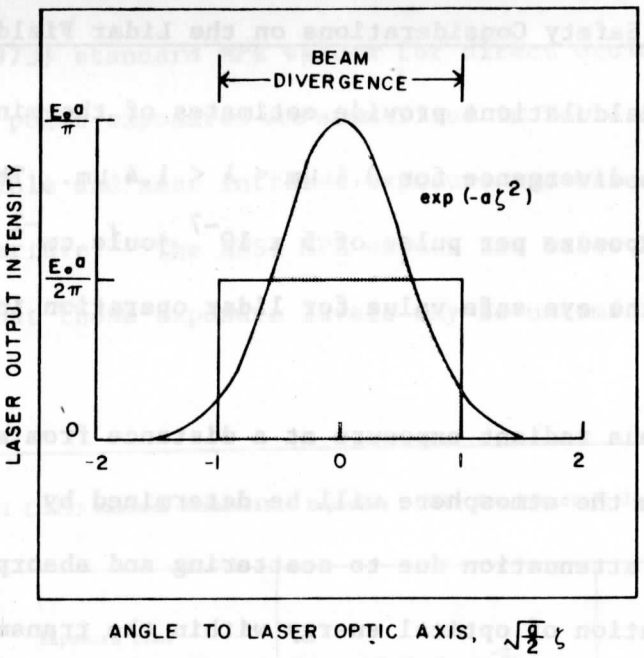

Figure 4-5 A comparison of the uniform and Gaussian models for the angular distribution of output laser energy. The shaded area represents that portion of the Gaussian distribution (86.5%) which falls within the full angle beam divergence.

which contains ∿86.5% of the transmitted energy. $E(\zeta)$ is then given by

$$E(\zeta) = \frac{E_o a}{\pi} \exp(-a\zeta^2) \qquad 4\text{-}2,2$$

for $$a = \frac{2\pi}{\Omega_o} \qquad 4\text{-}2,3$$

The energy per unit solid angle at the center of this distribution is

$$J_{max} = \lim_{\zeta_o \to 0} \frac{\int_0^{2\pi} d\phi \int_0^{\zeta_o} E(\zeta) \cdot \zeta d\zeta}{\int_0^{2\pi} d\phi \int_0^{\zeta_o} \zeta d\zeta} x_o^{-2} = 2E_o \Omega_o^{-1} x_o^{-2} \qquad 4\text{-}2,4$$

A comparison of Eqs. 4-2,1 and 4-2,4 shows that the more realistic Gaussian energy distribution gives a peak mean radiant exposure which is twice as great as that due to the uniform energy distribution.

The instantaneous radiant exposure will depart significantly from its mean value due to scintillation of the beam during transmission through the atmosphere. A useful estimate of the probabilities for encountering hazardous radiant exposures due to random beam fluctuations is given by Dabbert and Johnson (1971). Their experimental work determined the effect of range, laser wavelength, atmospheric thermal turbulence intensity and path geometry on the magnitude of laser scintillation. Figure 38 of Dabbert and Johnson, which is itself a conservative estimate, shows that the instantaneous probability for eye damage will be less than 10^{-2} when the mean radiant exposure is an order of magnitude less than the eye safe value. The results of Dabbert and Johnson are given in Table 4-3. We conclude that a radiant exposure which is a factor of ten below the ANSI (1973) MPE limit is adequate for eye safety.

Table 4-3 Worst Case Instantaneous Probability for Eye Damage due to Atmospheric Scintillation as Calculated by Dabbert and Johnson (1971).†

Ratio of eye safe to mean value of radiant exposure	Instantaneous probability for exceeding the eye safe value
$\gtrsim 10$	$\lesssim 10^{-2}$
25	10^{-3}
50	10^{-4}
100	10^{-5}
200	10^{-6}

†These results are based on a 5 mm limiting aperture

We conclude from the above that the instantaneous radiant exposure which is eye safe at the Earth's surface is

$$J_{sfc} = 2E_o\Omega_o^{-1}h_o^{-2} \leq J_{safe} \times 10^{-1} \qquad 4\text{-}2,5$$

Using the ANSI MPE value $J_{safe} = 5 \times 10^{-7}$ joule cm^{-2} (See Table 4-2), we find that the laser transmitter beam divergence must exceed the following minima:

$$\Omega_{o,min}E_o^{-1} \geq 20J_{safe}^{-1}h_o^{-2} \simeq 1.2 \times 10^{-7} \text{ sterad joule}^{-1} \text{ for } h_o = 185 \text{ km} \qquad 4\text{-}2,6a$$

$$\simeq 4 \times 10^{-5} \text{ sterad joule}^{-1} \text{ for } h_o = 10 \text{ km} \qquad 4\text{-}2,6b$$

The practical limit for laser transmitter beam divergence is $\Omega^*_{o,min} = 1 \times 10^{-9}$ ster, which occurs at

$$E_o^* \simeq 8.3 \text{ mj for } h_o = 185 \text{ km} \qquad 4\text{-}2,6c$$

$$\simeq 0.025 \text{ mj for } h_o = 10 \text{ km} \qquad 4\text{-}2,6d$$

Note that Eqs. 4-2,6 imply a safety factor which is two times safer than the Army and Navy field evaluation criterion given in section 4-2-a).

Assuming that the laser output is axially symmetric, the full angle divergence equivalents to Eqs. 4-2,6 are

$$\zeta_{full,min} \simeq .38\sqrt{\frac{E_o}{1 \text{ joule}}} \text{ mrad} \quad \text{for } h_o = 185 \text{ km} \qquad 4\text{-}2,7a$$

$$\simeq 7.1\sqrt{\frac{E_o}{1 \text{ joule}}} \text{ mrad} \quad \text{for } h_o = 10 \text{ km} \qquad 4\text{-}2,7b$$

The practical limit for the full angle divergence of the laser output is

$$\zeta^*_{full,min} \simeq 0.036 \text{ mrad} \qquad 4\text{-}2,7c$$

which is independent of transmitter altitude.

The area per unit energy of the illuminated "spot" on the Earth's surface is

$$A_{surface}E_o^{-1} = \Omega_{o,min}h_o^2E_o^{-1} = 20J_{safe}^{-1} \simeq 4 \times 10^3 \text{ m}^2\text{joule}^{-1} \qquad 4\text{-}2,8a$$

which is independent of transmitter altitude. The practical limit for the area of the "spot" is

$$\Omega^*_{o,min}h_o^2 = 34 \text{ m}^2 \text{ for } h_o = 185 \text{ km} \qquad 4\text{-}2,8b$$

$$= 0.1 \text{ m}^2 \text{ for } h_o = 10 \text{ km} \qquad 4\text{-}2,8c$$

4-2-c) The Solar Background and Signal to Noise Ratio

The worst case daytime solar signal can be estimated by scattering all of the available solar radiation from a Lambertian surface which completely fills the receiver field of view Ω_r. The worst case solar signal estimate, given in number of solar photons collected by the receiver telescope, is

$$N_s = \frac{\bar{A}}{\pi} \left(\frac{\hat{I}_\lambda \Delta\lambda}{hc\sigma} \cos\theta_s\right) A_r \, \Omega_r \tilde{\Delta t} \qquad 4\text{-}2,9$$

where $\hat{I}_\lambda$ is the solar spectral irradiance at 1AU, $\Delta\lambda$ is the receiver band pass at wavenumber σ, θ_s is the solar zenith angle, $\tilde{\Delta t}$ is the range gated signal averaging time, $\bar{A}$ is the albedo of the Lambertian scattering surface, c is the speed of light, and h is Planck's constant. Atmospheric attenuation of solar radiation has been neglected. A tabulation of the solar spectral irradiance at 1AU is given in Table 4-4.

The backscattered signal N is estimated by subtracting an independent measurement of N_s from the total lidar signal. The signal to noise ratio (SNR), considering statistical variations in the backscattered and solar signals but neglecting noise contributions due to system electronics and optical processing, is given by $N \cdot (N + N_s)^{-\frac{1}{2}}$. Since $N \propto E_o$ and $N_s \propto \Omega_{o,min} \propto E_o$ for $\Omega_{o,min} \geq \Omega^*_{o,min}$ when the lidar is operated at the worst case eye safe limit, the signal to noise ratio is effectively proportional to $E_o^{\frac{1}{2}}$.

Table 4-4 Solar Spectral Irradiance at 1 AU, from Table V of NASA SP-8005, May, 1971.

Solar Spectral Irradiance at 1 AU
(Solar Constant of 135.30mWcm-2)

Wavelength, λ (μm)	Average Irradiance, P_λ (W cm^{-2} μm^{-1})	Area under curve, 0 to λ, A_λ (mW cm^{-2})	Portion of solar constant with wavelength λ, D_λ (%)
0.120	0.000010	0.00059993	0.00044
0.140	0.000003	0.00073000	0.00054
0.150	0.000007	0.00077000	0.00058
0.160	0.000023	0.00093000	0.00069
0.170	0.000063	0.00135000	0.00101
0.180	0.000125	0.00230000	0.00170
0.190	0.000271	0.00428000	0.00316
0.200	0.00107	0.010985	0.0081
0.210	0.00279	0.027785	0.0205
0.220	0.00575	0.067985	0.0502
0.225	0.00669	0.090585	0.0729
0.230	0.00667	0.113485	0.0977
0.235	0.00593	0.162985	0.1205
0.240	0.00630	0.193560	0.1430
0.245	0.00773	0.227385	0.1681
0.250	0.00704	0.263060	0.1945
0.255	0.0104	0.306660	0.2268
0.260	0.0138	0.365160	0.2701
0.265	0.0185	0.443910	0.328
0.270	0.0222	0.548160	0.405
0.275	0.0284	0.657160	0.486
0.280	0.0272	0.763860	0.5644
0.285	0.0315	0.877910	0.6488
0.290	0.0482	0.09716	0.811
0.295	0.0584	1.36366	1.008
0.300	0.0514	1.63816	1.211
0.305	0.0653	1.91741	1.417
0.310	0.0689	2.20661	1.636
0.315	0.0764	2.60366	1.924
0.320	0.0938	3.00216	2.219
0.325	0.0975	3.45341	2.552
0.330	0.1049	3.96191	2.928
0.335	0.1081	4.44691	3.324
0.340	0.1074	5.03866	3.722
0.345	0.1069	5.57141	4.118
0.350	0.1093	6.11191	4.517
0.355	0.1083	6.65591	4.919
0.360	0.1068	7.19366	5.317
0.365	0.1132	7.74366	5.723
0.370	0.1181	8.32191	6.151
0.375	0.1157	8.98641	6.583
0.380	0.1128	9.47566	7.003
0.385	0.1098	10.0382	7.413
0.390	0.1098	10.5792	7.819
0.395	0.1108	11.1309	8.243
0.400	0.1439	11.8066	8.725
0.405	0.1644	12.5737	9.292
0.410	0.1751	13.4726	9.958
0.415	0.1774	14.3837	10.572
0.420	0.1747	15.1889	11.222

Wavelength, λ (μm)	Average Irradiance, P_λ (W cm^{-2} μm^{-1})	Area under curve, 0 to λ, A_λ (mW cm^{-2})	Portion of solar constant with wavelength λ, D_λ (%)
0.425	0.1693	16.0439	11.858
0.430	0.1639	16.8769	12.474
0.435	0.1663	17.7024	13.084
0.440	0.1810	18.5707	13.728
0.445	0.1922	19.5037	14.415
0.450	0.2008	20.4657	15.41
0.455	0.2057	21.5014	15.892
0.460	0.2066	22.5322	16.653
0.465	0.2048	23.5607	17.414
0.470	0.2033	24.5809	18.168
0.475	0.2044	25.6002	18.921
0.480	0.2074	26.6297	19.682
0.485	0.1996	27.6472	20.430
0.490	0.1930	28.6237	21.156
0.495	0.1960	29.6012	21.879
0.500	0.1962	30.5767	22.599
0.505	0.1920	31.5422	23.313
0.510	0.1882	32.4927	24.015
0.515	0.1833	33.4214	24.702
0.520	0.1833	34.3359	25.379
0.525	0.1852	35.2592	26.060
0.530	0.1842	36.1827	26.743
0.535	0.1818	37.0977	27.419
0.540	0.1783	37.9979	28.081
0.545	0.1754	38.8822	28.728
0.550	0.1725	39.7519	29.381
0.555	0.1728	40.6132	30.017
0.560	0.1693	41.4669	30.648
0.565	0.17[illegible]	42.3169	31.276
0.570	0.[illegible]12	43.1712	31.908
0.575	0.1719	44.0288	32.542
0.580	0.1715	44.8874	33.176
0.585	0.1712	45.7462	33.809
0.590	0.1708	46.5972	34.440
0.595	0.1682	47.4427	35.065
0.600	0.1665	48.2797	35.683
0.605	0.1662	49.1079	36.296
0.610	0.1658	49.9284	36.902
0.620	0.1652	51.5469	38.098
0.630	0.1578	53.1289	39.270
0.640	0.1566	54.6899	40.425
0.650	0.1511	56.2174	41.560
0.660	0.1488	57.7159	42.688
0.670	0.1456	59.1809	43.768
0.680	0.1427	60.6284	44.840
0.690	0.1402	62.0439	45.886
0.700	0.1368	63.4384	46.888
0.710	0.1366	64.7849	47.882
0.720	0.1314	66.1139	48.865
0.730	0.1298	67.4189	49.827

Wavelength, λ (μm)	Average Irradiance, P_λ (W cm^{-2} μm^{-1})	Area under curve, 0 to λ, A_λ (mW cm^{-2})	Portion of solar constant with wavelength λ, D_λ (%)
0.740	0.1288	68.6909	50.784
0.750	0.1235	69.9284	51.691
0.800	0.1192	75.7924	56.019
0.850	0.0988	81.8359	59.898
0.900	0.0889	85.7724	63.358
0.950	0.0835	90.0334	66.544
1.000	0.0746	93.9859	69.465
1.100	0.0592	100.676	74.409
1.200	0.0484	106.056	78.388
1.300	0.0396	110.456	81.638
1.400	0.0336	114.116	84.343
1.500	0.0287	117.231	86.645
1.600	0.0244	119.886	88.602
1.700	0.0202	122.116	90.256
1.800	0.0159	123.921	91.590
1.900	0.0126	125.346	92.643
2.000	0.0103	126.491	93.489
2.100	0.0090	127.456	94.202
2.200	0.0079	128.301	94.827
2.300	0.0068	129.026	95.378
2.400	0.0064	129.696	95.858
2.500	0.0054	130.286	96.294
2.600	0.0048	130.796	96.671
2.700	0.0043	131.251	97.008
2.800	0.00390	131.661	97.3104
2.900	0.00350	132.031	97.5838
3.000	0.00310	132.361	97.8277
3.100	0.00280	132.656	98.0364
3.200	0.00250	132.889	98.2108
3.300	0.00192	133.098	98.3724
3.400	0.00166	133.277	98.5047
3.500	0.00146	133.433	98.6200
3.600	0.00128	133.573	98.7239
3.700	0.00113	133.702	98.8192
3.800	0.00111	133.819	98.9057
3.900	0.00103	133.926	98.9848
4.000	0.00093	134.025	99.0580
4.100	0.00087	134.116	99.1252
4.200	0.00078	134.199	99.1862
4.300	0.00071	134.273	99.2412
4.400	0.00066	134.341	99.2915
4.500	0.00059	134.403	99.3373
4.600	0.00053	134.459	99.3787
4.700	0.00048	134.510	99.4160
4.800	0.00045	134.556	99.4584
4.900	0.00041	134.599	99.482795
5.000	0.0003838	134.63906	99.511388
6.000	0.0001738	134.91886	99.717709
7.000	0.0000990	135.05606	99.818865
8.000	0.0000600	135.13456	99.877734

Wavelength, λ (μm)	Average Irradiance, P_λ (W cm^{-2} μm^{-1})	Area under curve, 0 to λ, A_λ (mW cm^{-2})	Portion of solar constant with wavelength λ, D_λ (%)
9.000	0.0000380	135.18356	99.913939
10.000	0.0000258	135.21306	99.935721
11.000	0.0000170	135.23606	99.952742
12.000	0.0000120	135.25056	99.963459
13.000	0.0000087	135.26091	99.971109
14.000	0.0000065	135.26891	99.976356
15.000	0.0000049	135.27521	99.980200
16.000	0.0000038	135.27956	99.983415
17.000	0.0000031	135.28181	99.985063
18.000	0.0000024	135.28376	99.987497
19.000	0.0000020	135.28596	99.989073
20.000	0.0000016	135.28776	99.990393
25.000	0.0000006 90	135.29328	99.990837
30.000	0.0000003 00	135.29536	99.992318
35.000	0.0000001 60	135.29671	99.993368
40.000	0.0000000 94	135.29735	99.993838
50.000	0.0000000 38	135.29801	99.994315
60.000	0.0000000 19	135.29829	99.994518
80.000	0.0000000 07	135.29855	99.994708
100.000	0.0000000 03	135.29865	99.994802
1000.000	0.0000000 00	135.30000	100.000000

Worst case estimates for N_s at representative wavelengths are given in Table 4-5. Since $\Omega_{o,min}$ is proportional to E_o, these N_s estimates are given in units of numbers of photons per millijoule output. The High Spectral Resolution Lidar system has a bandpass $\delta\lambda_D$ or $\delta\sigma_D = \delta\lambda_D \cdot \lambda^{-2}$. Values for $\delta\lambda_D$ at an atmospheric temperature T = 250°K, and the solar signal which is passed by such a filter are also given in Table 4-5. For $E_o \leq E_o^*$, $\Omega_{o,min}$ cannot be reduced beyond the practical operating limit $\Omega^*_{o,min}$ and the solar signal assumes its minimum value $N_{s,min}$. Shuttle case values for the worst case solar signal at minimum practical beam divergence $\Omega^*_{o,min}$ are also given in Table 4-5.

4-2-d) Reduction of the Solar Signal through Lidar Operation in a Fraunhofer Line.

The Table 4-5 values for the solar signal can be reduced through lidar operation within a Fraunhofer line. A partial list of suitable Fraunhofer lines is given in Table 4-6. Included in this table are:

1) peak line depths in percent of the solar continuum, as measured at the Earth's surface for direct solar radiation, and

2) the line width measured at twice the peak line depth.

Figure 4-6 presents the location of several of these lines with respect to the output of a commercially available dye laser.

Table 4-5 Typical Values for the Solar Signal at Representative Wavelengths - Shuttle Case[1]

	λ [Å]	$\hat{I}_\lambda$[2] [joule $sec^{-1} cm^{-2} \mu m^{-1}$]	$N_s \cdot \Delta\lambda^{-1}$ [photons $mj^{-1} Å^{-1}$]	$N_s \cdot \Delta\lambda^{-1} \cdot \delta\lambda_D$ [photons mj^{-1}]	$\delta\lambda_D$[3] [mÅ]	$\delta\sigma_D$ [cm^{-1}]	$N_{s,min}$[4] [photons]
N_2	3371	.108	23	0.3	14.2	.125	13
Coumarin 2 1350-4750 Å	4500	.201	58	1.1	18.9	.093	46
Ar^+	4880	.195	61	1.2	20.5	.086	50
Ar^+	5145	.183	60	1.3	21.6	.082	55
Rhodamine 6G 4500-6500 Å	5500	.173	61	1.4	23.1	.076	58
HeNe	6238	.160	64	1.7	26.2	.067	71
Ruby	6943	.140	62	1.8	29.2	.061	76

(1) The solar signal values are calculated for minimum eyesafe beam divergence, and are given in units of photons per millijoule of transmitted laser energy. The solar signal is that number of solar photons collected by the receiver telescope. The calculations use the following Shuttle case values:

$\cos\theta_s = 1$ $\quad \Omega_r = 1.2 \times 10^{-7}$ ster $joule^{-1}$ output (Eq. 4-2,6a)

$A_r = 1 m^2$ $\quad \tilde{\Delta t} = 0.33 \times 10^{-5}$ sec $(\frac{c\tilde{\Delta t}}{2} = 500m)$

$h_o = 185$ km $\quad \bar{A} = 1$

The values for $N_s \cdot \Delta\lambda^{-1}$ and $N_s \cdot \Delta\lambda^{-1} \cdot \delta\lambda_D$ are based on single samples for eye safe operation at 1 mj laser output. For total solar signal based on an average of N samples with a laser output of E_o [joules], multiply these values by $NE_o/1$ mj. The following values are used for the aircraft case:

$h_o = 10$ km $\quad \Omega_r = 4 \times 10^{-5}$ ster $joule^{-1}$ output (Eq. 4-2,6b)

$A_r = 0.1 m^2$

For the aircraft case, divide the solar signal values by 3. Lidar operation in a Fraunhofer line may reduce the solar signal by an order of magnitude.

(2) From Table V of NASA SP-8005, May, 1971. $\int_0^\infty \hat{I}_\lambda d\lambda = 1353$ watts m^{-2}.

(3) The Doppler width (FWHM) for photons which are backscattered by molecules is

$$\delta\lambda_D = 4\sqrt{.693}\ \frac{\lambda}{c}\sqrt{\frac{2kT}{\bar{m}}}$$

where k is Boltzmann's constant, $\bar{m}$ is the mean molecular mass and T is the atmospheric temperature (T was chosen to be 250°K). Note that $\delta\sigma_D = \delta\lambda_D \cdot \lambda^{-2}$.

(4) The transmitter beam divergence and receiver field of view have the practical limit $\Omega^*_{o,min} = \Omega_{r,min} = 5 \times 10^{-9}$ ster. This limit is reached when $E_o \leq 42$ mj for the Shuttle case, and when $E_o \leq .13$ mj for the aircraft case. For the aircraft case, divide the $N_{s,min}$ values by 10.

Table 4-6 A Partial List of Deep Fraunhofer Lines with Peak Depths and Line Width Estimates for Direct Solar Radiation[1]

Identification	Wavelength [Å]	Minimum[2] Intensity (%)	Line Width[3] [mÅ]
FeI	4005.3	4.0	60
MnI	4030.8	2.7	80
MnI	4033.1	2.9	80
FeI	4045.8	2.8	70
FeI	4063.6	3.1	70
CaI	4226.8	2.6	80
CrI	4254.4	3.7	70
FeI	4307.9	4.0	80
FeI	4383.6	3.7	80
FeI	4404.8	4.5	80
BaII	4554.0	6.0	70
HgI	5183.6	6.0	120
NaI (D2)	5890.0	4.6	140

(1) Data are taken from the Kitt Peak Solar Atlas (1975).

(2) Minimum intensity is given in percent of the adjacent solar continuum at the wavelength of the Fraunhofer line. These values represent peak intensities in direct solar radiation.

(3) The line width as measured from the Kitt Peak Solar Atlas spectra of each line at an intensity level which is twice the minimum intensity.

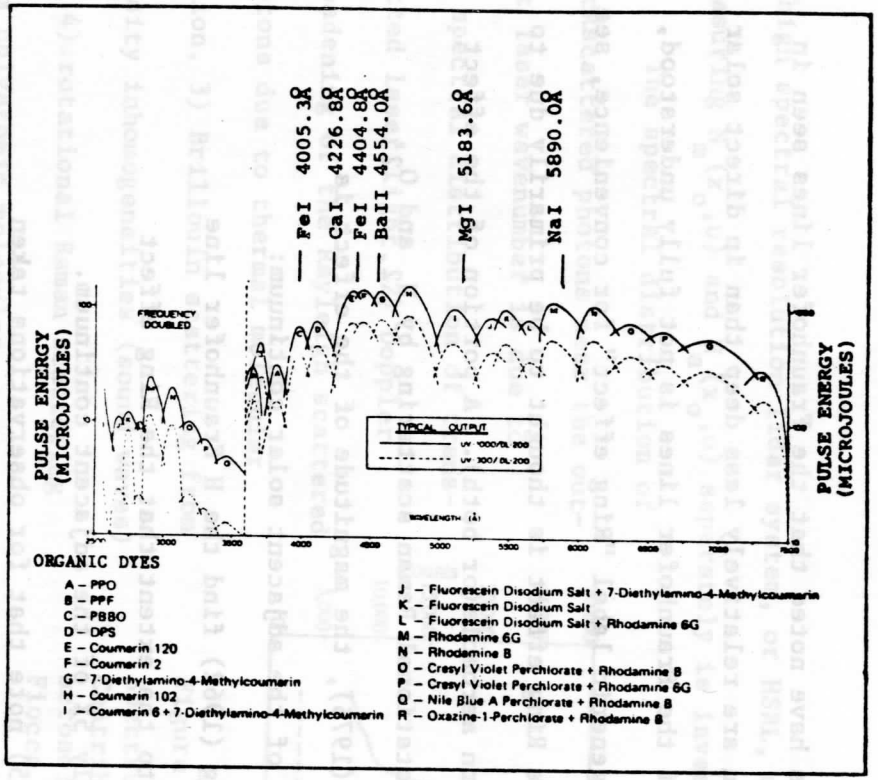

Figure 4-6 Locations of several deep Fraunhofer lines with respect to the spectral output of a commercially available dye laser. Example for the Molectron DL-Series dye laser with a UV-Series super-radiant N_2 laser pump.

A number of observers have noted that the Fraunhofer lines seen in atmospheric diffuse radiation are relatively less deep than in direct solar radiation. The filling-in of the Fraunhofer lines is not fully understood, and the effect is given the generic label "Ring effect" for convenience, see Grainger and Ring (1962). The Ring effect is thought to be primarily due to flourescence of air or airborn aerosols (or both). A portion of the effect could also be explained by rotational Raman scattering by N_2 and O_2.

As cited by Barmore (1975), the magnitude of the effect is reported to be a few percent of the adjacent solar continuum:

> Grainger and Ring (1962) find the H Fraunhofer line at 3968 Å filled in to the extent that the Ring effect would be approximately 5% of the adjacent continuum. Noxon and Goody (1965) note that for observations taken near noon, the Ring effect is about 3% at 4300 Å and 1.5% at 6563 Å.[1]

The Ring effect shows variations with wavenumber, solar zenith angle, the day and time of observation, and the surface albedo, see Hunten (1970). To our knowledge, measurements of the Ring effect with downward viewing spectrometers have not been conducted. In the absence of measurements, we assume that the Ring effect is comparable in magnitude in both the upward and downward directions. We conclude that the solar background radiation can be reduced by at most a factor of 10 through the operation of lidars within Fraunhofer lines.

4-3 High Spectral Resolution Lidar

4-3-a) Introduction

The conventional elastic backscatter lidar measures

$$N_m(x_o,u) + N_a(x_o,u).$$

[1] Barmore (1975), pp. 1491-1492.

A high spectral resolution lidar system, or HSRL, which is capable of measuring $N_m(x_o,u)$ and $N_a(x_o,u)$ separately is investigated.

The spectral distribution of backscattered photons near the output laser wavenumber is due to 1) spectral distribution of transmitted laser light, 2) Doppler broadening of the Rayleigh scattered photons due to thermal molecular motion, 3) Brillouin scattering from density inhomogeneities (sound waves) and 4) rotational Raman scattering from polyatomic molecules.

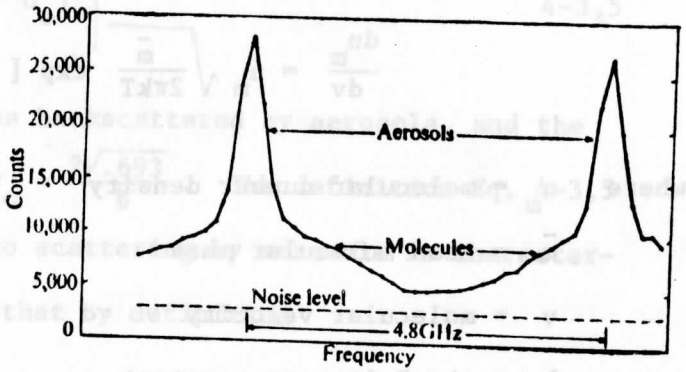

Figure 4-7
Spectrum of echoes from air. Contributions of molecules from aerosols can be separated, from Fiocco et al. (1971).

Figure 4-7 shows the elastically scattered aerosol return maximum, and the Doppler broadened return from atmospheric molecules. This data was obtained by Fiocco et al. (1971), who measured the spectral distribution of laser echoes about the output laser frequency using an Ar^+ laser (λ = 4880 Å). The Ar^+ laser output was stable to ± 50 MHz (± .0016 cm^{-1}) at 0.5 watts. The piezoelectrically scanned Fabry-Perot interferometer had a free spectral range Q of 4.8 GHz (0.16 cm^{-1}) and a finesse n_r of about 12,[1] see Mack et al. (1963).

---

[1] The resolving width (full width at half maximum, or FWHM) is therefore $\delta\sigma = Q/n_r \simeq .013\ cm^{-1}$, i.e. about 8 times the output wavenumber stability.

4-3-b) Characterization of Atmospheric Scattering of Laser Light

The distribution in one dimension of molecular velocity for a gas at atmospheric pressures is approximately Maxwellian, such that

$$\frac{dn_m}{dv} = n_m \sqrt{\frac{\bar{m}}{2\pi kT}} \exp\left[- \frac{\bar{m}v^2}{2kT} \right] \qquad 4\text{-}3,1$$

where n_m = molecular number density

$\bar{m}$ = mean molecular mass

v = molecular velocity

k = the Boltzmann constant

and T = atmospheric temeprature.

According to Fiocco and DeWolf (1968), Eq. 4-3,1 holds throughout the atmosphere as an approximation with about a 4% correction needed at surface molecular densities due to Brillouin scattering. The Doppler shift for backscattering is

$$\frac{1}{\sigma_o} (\sigma - \sigma_o) = 2 \frac{v}{c} \qquad 4\text{-}3,2$$

such that

$$\frac{dv}{d\sigma} = \frac{1}{2} \cdot \frac{c}{\sigma_o} \qquad 4\text{-}3,3$$

where c is the speed of light, σ is the backscattered signal wavenumber and σ_o is the wavenumber of maximum emission by the laser. The spectral distribution of photons scattered by molecules is therefore

$$\frac{1}{N_m} \frac{dN_m}{d\sigma} = \frac{1}{\sqrt{\pi}} \sqrt{\frac{\bar{m}c^2}{8\sigma_o^2 kT}} \exp\left[- \frac{\bar{m}c^2}{8\sigma_o^2 kT} (\sigma - \sigma_o)^2 \right] \qquad 4\text{-}3,4$$

where N_m is the total number of photons backscattered by molecules.

For purposes of this discussion, the laser output is assumed to follow a gaussian distribution in wavenumber, such that the spectral distribution of photons elastically scattered by aerosols is

$$\frac{1}{N_a}\frac{dN_a}{d\sigma} = \frac{b}{\sqrt{\pi}} \exp\left[-b^2(\sigma - \sigma_o)^2\right] \qquad 4\text{-}3,5$$

where N_a is the total number of photons backscattered by aerosols, and the full spectral width of the laser is $\delta\sigma_o = \frac{2\sqrt{.693}}{b}$. The definition Eq. 4-3,5 assumes that spectral dispersion due to scattering by aerosols is characterized by a Dirac delta function. Note that by definition

$$\int_o^\infty \frac{1}{N_m}\cdot\frac{dN_m}{d\sigma}\cdot d\sigma = \int_o^\infty \frac{1}{N_a}\cdot\frac{dN_a}{d\sigma}\cdot d\sigma = 1 \qquad 4\text{-}3,6$$

where $\frac{1}{N_m}\frac{dN_m}{d\sigma}$ and $\frac{1}{N_a}\frac{dN_a}{d\sigma}$ are defined by Eqs. 4-3,4 and 4-3,5, respectively.

Maximal tropospheric aerosol vertical velocities may typically be $\sim$1 m sec^{-1}. This corresponds to a Doppler shift which is approximately 1/100 of the laser output resolution of a typical HSRL, see Table 4-9. Therefore, the Dirac delta function approximation for the spectral dispersion due to scattering by aerosols is good for the case of a nadir pointing HSRL. Caution must be exercised, however, that the HSRL does not operate at some non-zero angle to the nadir, or that there is a sizable vertical velocity in the platform trajectory.

4-3-c) Brillouin Scattering

The spectral intensity of light scattered by a gas assumes the characteristic Doppler gaussian shape whenever the interactions between gas molecules can be disregarded. In this case (pressure << 1 atm), the molecular velocity distribution is dominated by the diffusion of thermal energy, giving rise to a central component in the scattered energy spectrum. As the gas pressure is increased, molecular velocity correlations arise from molecular interactions which spectrally redistribute the scattered energy. In this case (pressure > 1 atm),

the propagation of pressure waves through the scattering medium gives rise to a symmetrically shifted Brillouin doublet.

Yip and Nelkin (1964) have calculated the spectral response of a fluid model in which particle number, momentum and energy is conserved. The shape of the fluid model response is a function of the parameter

$$y = \frac{\alpha}{2\pi K}\left(\frac{2kT}{\bar{m}}\right)^{-\frac{1}{2}} \qquad 4\text{-}3,7$$

which represents the ratio of the fluctuation wavelength to the collision mean free path. K is the wavenumber associated with the momentum transfer in the scattering

$$K = 2\,\sigma_o \sin(\theta/2) \qquad 4\text{-}3,8a$$

where σ_o is the wavenumber of the incident radiation and θ is the scattering angle. The effective collision frequency α can be approximated by

$$\alpha = \frac{5}{4}\,\rho\,\frac{2k^2T}{\bar{m}k_T} \qquad 4\text{-}3,8b$$

where ρ is molecular density (cm^{-3}) and k_T is thermal conductivity of the gas (erg cm^{-1} sec^{-1} $°K^{-1}$).

In terms of the parameter y, the pressure fluctuations are collision dominated hydrodynamic processes when $y \gg 1$. For $y \ll 1$, collisions are no longer important and the fluid behaves as a system of independent particles. The results of Yip and Nelkin for the spectral intensity of light scattering from an ideal gas are presented in Figure 4-8. Values for the parameter y at several altitudes for the McClatchey et al. (1971) Tropical model atmosphere are given in Table 4-7.

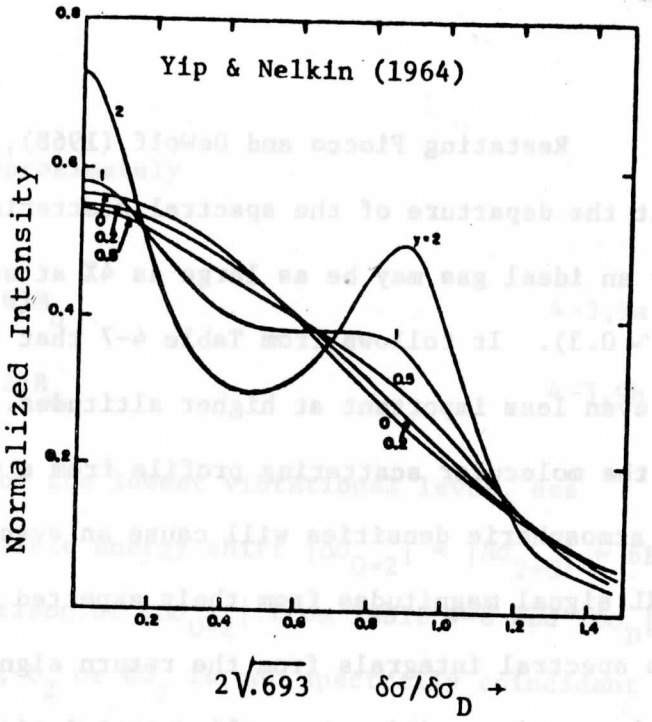

Figure 4-8.

The spectral intensity of light scattered from an ideal gas for various values of the parameter y. The abscissa is expressed in terms of a normalized wavenumber shift $\delta\sigma/\delta\sigma_D$, where $\delta\sigma_D$ is the wavenumber FWHM for pure Doppler scattering. The parameter $y \sim 0.3$ at surface atmospheric densities.

Table 4-7 Values for the Parameter y at Several Altitudes for the Model Tropical Atmosphere of McClatchey et al. (1971), $\lambda = 4880\text{Å}$ (1)

altitude [km]	pressure [mb]	temperature [°K]	parameter y (2)
0	1013	300	.273
2	805	288	.229
5	559	270	.173
10	286	237	.105
20	57	207	.025

(1) To compute the parameter y at other wavelengths, note that Eqs. 4-3,7 and 4-3,8a give $y \propto \lambda$.

(2) The thermal conductivity for air can be approximated by $k_T = \bar{m}\rho c_p D$, where c_p is the specific heat at constant pressure and the self-diffusion coefficient $D \simeq 0.18\ \text{cm}^2\text{sec}^{-1}$ for air at 0°C and 1000 mb. D varies with temperature and pressure by the relation $D \propto T^{1.81} p^{-1}$, see Smithsonian Meteorological Tables (1949), Table 113.

Restating Fiocco and DeWolf (1968), Yip and Nelkin's results indicate that the departure of the spectral scattering profile from a Gaussian profile for an ideal gas may be as large as 4% at surface atmospheric densities ($y \sim 0.3$). It follows from Table 4-7 that the effect of Brillouin scattering is even less important at higher altitudes. The relatively small departure of the molecular scattering profile from a Gaussian due to Brillouin scattering at atmospheric densities will cause an even less significant departure of HSRL signal magnitudes from their expected values. The HSRL system derives two spectral integrals from the return signal. The values of these integrals are insensitive to small uncertainties in the shape of the molecular return. This is shown in Figure 4-14 (Section 4-3-g), where an uncertainty in atmospheric temperature of ± 25°K results in a measurement error which is less than 1%.

Even though the impact on HSRL operation is insignificant, the spectral intensity departures due to Brillouin scattering can be accounted for by theoretical corrections. Yip (1971) has incorporated kinetic models for polyatomic molecules into the Brillouin scattering theory. The results of Yip agree with the experimental results of Greytak and Benedek (1966) for scattering by polyatomic molecules at atmospheric pressures.

4-3-d) Rotational Raman Scattering

Recent experimental work by Penney et al. (1974) and Fenner et al. (1973) has established the absolute cross sections for rotational Raman scattering (RRS) from atmospheric gases, particularly for N_2, O_2 and CO_2. The RRS for these simple linear molecules is determined by the allowed transitions $J \rightarrow J \pm 2$ where J is the initial rotational-angular-momentum quantum number.

The RRS spectral shifts $\Delta\sigma_{J\to J'}$ are approximately

$$\Delta\sigma_{J\to J+2} = -(4J+6)B_o \qquad 4\text{-}3,9a$$

$$\Delta\sigma_{J\to J-2} = +(4J-2)B_o \qquad 4\text{-}3,9b$$

where B_o is the rotational constant for the lowest vibrational level, see Table 4-8. Values for the lowest possible energy shift $|\Delta\sigma_{0\to 2}| = |\Delta\sigma_{2\to 0}| = 6B_o$ are also given in Table 4-8. A comparison of $|\Delta\sigma_{0\to 2}|$ from Table 4-8 and $|\delta\sigma_D|$ from Table 4-5 shows that RRS from N_2, O_2 or CO_2 is not spectrally coincident with the Rayleigh spectral scattering region of interest, and will therefore not be a concern for the HSRL system.

Table 4-8 Values of the Rotational Constant for the Lowest Vibrational Level for N_2, O_2, and CO_2, from Penney et al. (1974)

gas	$B_o(cm^{-1})$	$\lvert\Delta\sigma_{0\to 2}\rvert = 6B_o(cm^{-1})$
N_2	1.990	11.94
O_2	1.438	8.64
CO_2	0.390	2.34

4-3-e) The HSRL Polyetalon Receiver System

The HSRL receiver system is diagramed in Figure 4-9. To achieve the high contrast needed for an operational HSRL, a three Fabry-Perot etalon train (FP1, FP2, FP3 in Figure 4-9) is used to suppress background radiation outside of its passband of full width at half maximum (FWHM) $\delta\sigma_{123}$ at σ_r, the wavenumber

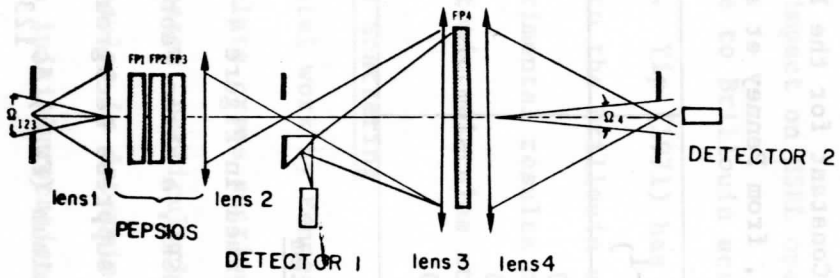

Figure 4-9 A schematic representation of an HSRL receiver system incorporating a PEPSIOS high resolution spectrometer.

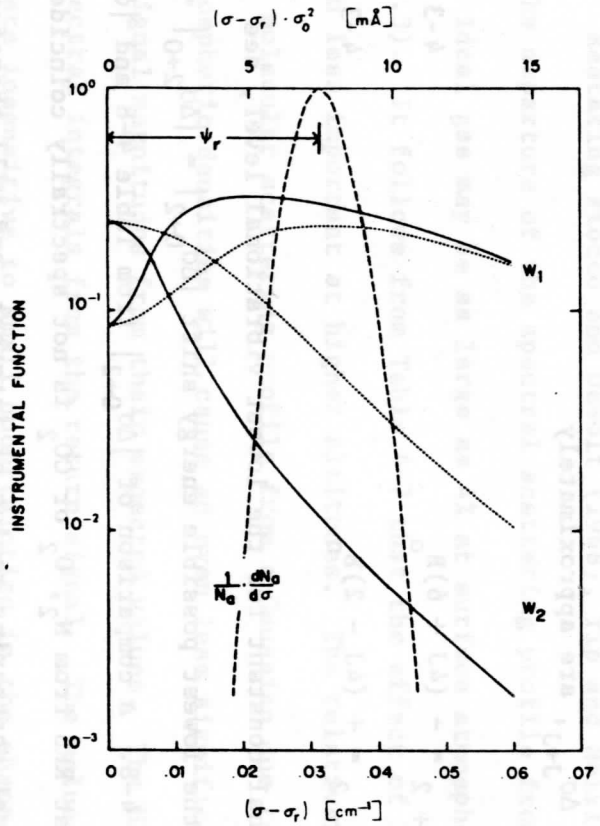

Figure 4-10 The instrumental functions W_1 and W_2 for the high (solid line) and low (dotted line) resolution example HSRL systems. The laser output spectral distribution is shown as a dashed line.

of maximum receiver transmission. The etalon FP4 is used to achieve very high resolution with FWHM $\delta\sigma_4$ at σ_r. When $\sigma_r = \sigma_o$, where σ_o is the laser output wavenumber maximum, most of those photons scattered by aerosols reach detector #2, and a large fraction of those photons scattered by molecules (Doppler shifted) reach detector #1.

As cited in Mack et al. (1963), the instrumental functions[1] W_1 and W_2 for detectors #1 and #2 are

$$W_1(\sigma) = W_{123}(\sigma)\cdot\{(1-A')\cdot[1 - W_4(\sigma)] + \frac{A'^2R'}{(1-R')^2}\cdot W_4(\sigma)\}\cdot\left(1- \frac{A'}{1-R'}\right)^6 \qquad 4\text{-}3,10$$

and

$$W_2(\sigma) = W_{123}(\sigma)\cdot W_4(\sigma)\left(1 - \frac{A'}{1-R'}\right)^8 \qquad 4\text{-}3,11$$

where

$$W_{123}(\sigma) = \frac{1}{\delta\sigma_{123}}\int_{\sigma-\frac{1}{2}\delta\sigma_{123}}^{\sigma+\frac{1}{2}\delta\sigma_{123}} a_1 a_2 a_3\cdot d\sigma' \qquad 4\text{-}3,12a$$

$$W_4(\sigma) = \frac{1}{\delta\sigma_4}\int_{\sigma-\frac{1}{2}\delta\sigma_4}^{\sigma+\frac{1}{2}\delta\sigma_4} a_4 d\sigma' \qquad 4\text{-}3,12b$$

and $$a_i(\sigma) = \left\{1 + \frac{4R'}{(1-R')^2}\sin^2(2\pi n'\ell_i\sigma\cos\theta)\right\}^{-1} \qquad 4\text{-}3,12c$$

The notation is as follows:

A' = etalon coating absorption coefficient

R' = etalon coating reflection coefficient

---

[1]The term "instrumental function" denotes the receiver spectral transmission function as seen by each detector.

n' = refractive index of etalon gap

ℓ_i = i^{th} etalon gap spacing

θ = angle of ray path to the optic axis

$\mathcal{A}_i(\sigma)$ = the "Airy" function.

$\delta\sigma_{123}$ and $\delta\sigma_4$ are the theoretical resolutions of the PEPSIOS (Poly Etalon Pressure Scanned Interferometric Optical Spectrometer.) spectrometer and the high resolution etalon, respectively. The integrals in Eqs. 4-3,12 account for the decrease in resolution caused by the finite instrumental apertures. Any effects due to etalon surface defects have been neglected.

The maximum angular receiver field of view is given by $\sqrt{8/(1.31R)}$, where $R = \sigma/\delta\sigma$ is the effective (actual) resolution of the polyetalon system. The solid angle field of view of the PEPSIOS (FP1, FP2, FP3 in Fig. 4-9) is therefore

$$\Omega_{123} = 2\pi R^{-1} = 2\pi\left(\frac{\delta\sigma_{123}}{\sigma_r}\right) \qquad 4\text{-}3,13$$

The high resolution etalon must have a smaller field of view to secure operation within one free spectral range, such that

$$\Omega_4 = 2\pi\left(\frac{\delta\sigma_4}{\sigma_r}\right) \qquad 4\text{-}3,14$$

The effective receiver field of view can be decreased without a corresponding sacrifice in signal luminance by the addition of a receiver telescope of area A_r. The final "telescopic" receiver solid angle Ω_r is then defined by the constraint that etendue is conserved, such that

$$\Omega_r = \Omega_{123} \cdot \frac{A_e}{A_r} \qquad 4\text{-}3,15$$

where A_e is the area of the etalon plates.

4-3-f) Signal Calculation and Solutions

Let $\bar{N}_m$ and $\bar{N}_a$ represent the total number of laser photons which are backscattered by molecules and aerosols, respectively, and gathered by the receiver telescope. Also let $\bar{N}_s$ represent the total number of solar photons which are gathered by the receiver telescope. The quantities $\bar{N}_m$, $\bar{N}_a$ and $\bar{N}_s$ are integrated over the range gated time interval $\tilde{\Delta t}$. The signals $\bar{S}_1$ and $\bar{S}_2$ at detectors #1 and #2, respectively, are linear combinations of $\bar{N}_m$, $\bar{N}_a$ and $\bar{N}_s$ such that

$$\bar{S}_1 = \mu_{1m}\bar{N}_m + \mu_{1a}\bar{N}_a + \mu_{1s}\bar{N}_s \qquad 4\text{-}3,16a$$

$$\bar{S}_2 = \mu_{2m}\bar{N}_m + \mu_{2a}\bar{N}_a + \mu_{2s}\bar{N}_s \qquad 4\text{-}3,16b$$

where[1]

$$\mu_{1m} = \int_0^\infty W_1 q_e \cdot \left(\frac{1}{N_m}\frac{dN_m}{d\sigma} * \frac{1}{N_a}\frac{dN_a}{d\sigma}\right) \cdot d\sigma \qquad 4\text{-}3,17a$$

$$\mu_{2m} = \int_0^\infty W_2 q_e \cdot \left(\frac{1}{N_m}\frac{dN_m}{d\sigma} * \frac{1}{N_a}\frac{dN_a}{d\sigma}\right) \cdot d\sigma \qquad 4\text{-}3,17b$$

$$\mu_{1a} = \int_0^\infty W_1 q_e \cdot \left(\frac{1}{N_a}\frac{dN_a}{d\sigma}\right) \cdot d\sigma \qquad 4\text{-}3,17c$$

$$\mu_{2a} = \int_0^\infty W_2 q_e \cdot \left(\frac{1}{N_a}\frac{dN_a}{d\sigma}\right) \cdot d\sigma \qquad 4\text{-}3,17d$$

---

[1] The operator * denotes "convolution product," such that

$$X(\sigma_o) = Y * Z = \int_0^\infty Y(\sigma) \cdot Z(\sigma - \sigma_o) \cdot d\sigma$$

and

$$\mu_{1s} = \int_0^\infty W_1 q_e \cdot d\sigma \qquad 4\text{-}3,17e$$

$$\mu_{2s} = \int_0^\infty W_2 q_e \cdot d\sigma \qquad 4\text{-}3,17f$$

The instrumental functions W_1 and W_2 are defined in Eqs. 4-3,10 and 4-3,11, respectively, and q_e is the detector quantum efficiency.

$\frac{1}{N_m}\frac{dN_m}{d\sigma} * \frac{1}{N_a}\frac{dN_a}{d\sigma}$ and $\frac{1}{N_a}\frac{dN_a}{d\sigma}$ represent the spectral distributions of photons scattered by molecules and aerosols, respectively, which are gathered by the receiver telescope. Since the aerosols are considered to be elastic scattering centers, the spectral dispersion due to scattering by aerosols is characterized by a Dirac delta function and the spectral distribution of the laser output is identically $\frac{1}{N_a}\frac{dN_a}{d\sigma}$.

Let the signals measured at detectors #1 and #2 in the time interval $\tilde{\Delta t}$ be denoted by $\hat{S}_1$ and $\hat{S}_2$, respectively. In general, $\hat{S}_1 \neq \bar{S}_1$ and $\hat{S}_2 \neq \bar{S}_2$ due to statistical fluctuations in the photon count. Estimates $\hat{N}_m$ and $\hat{N}_a$ of the quantities $\bar{N}_m$ and $\bar{N}_a$ can be derived from the measurements $\hat{S}_1$ and $\hat{S}_2$ by means of Eqs. 4-3,16 as follows:

$$\hat{N}_m = c_{1m}\hat{S}_1' + c_{2m}\hat{S}_2' \qquad 4\text{-}3,18a$$

$$\hat{N}_a = c_{1a}\hat{S}_1' + c_{2a}\hat{S}_2' \qquad 4\text{-}3,18b$$

for

$$\hat{S}_1' = \hat{S}_1 - \mu_{1s}\hat{N}_s \qquad 4\text{-}3,18c$$

$$\hat{S}_2' = \hat{S}_2 - \mu_{2s}\hat{N}_s \qquad 4\text{-}3,18d$$

where

$$c_{1m} = +\mu_{2a}\cdot\xi^{-1} \qquad 4\text{-}3,19a$$

$$c_{2m} = -\mu_{1a}\cdot\xi^{-1} \qquad 4\text{-}3,19b$$

$$c_{1a} = -\mu_{2m}\cdot\xi^{-1} \qquad 4\text{-}3,19c$$

$$c_{2a} = +\mu_{1m}\cdot\xi^{-1} \qquad 4\text{-}3,19d$$

and

$$\xi = \mu_{1m}\mu_{2a} - \mu_{2m}\mu_{1a} \qquad 4\text{-}3,19e$$

Note that for best results, we require that the crosstalk terms c_{2m} and c_{1a} should be much less than both c_{1m} and c_{2a}. The quantities $\mu_{1s}\hat{N}_s$ and $\mu_{2s}\hat{N}_s$ can be estimated by time averaged values of $\hat{S}_1$ and $\hat{S}_2$ during the periods between laser firings.

The estimates $\hat{N}_m$ and $\hat{N}_a$ are not equal to the actual values $\bar{N}_m$ and $\bar{N}_a$ due to two types of error when $\hat{N}_m$ and $\hat{N}_a$ are derived by means of Eqs. 4-3,18. These are:

I) error due to a change or uncertainty in an HSRL system parameter. Uncertainty in sampled volume temperature (T), uncertainty in laser transmitter spectral width (FWHM $\psi_o = \delta\sigma_o = \sqrt{.693}/b$ (see Eq. 4-3,5), and uncertainty in transmitter-receiver peak detuning ($\psi_r = \sigma_o - \sigma_r$) will affect the transmittances μ_{im} and μ_{ia} and hence the inversion coefficients c_{im} and c_{ia}, i = 1,2.

Type I error is calculated below in the following manner: If T, ψ_o and ψ_r are perfectly known, then signals $\hat{S}_1$ and $\hat{S}_2$ (no statistics) can be inverted exactly to original a priori photon inputs $\bar{N}_a$ and $\bar{N}_m$. Given change in the parameters T, ψ_o and/or ψ_r, the inverted quantities are calculated using the unchanged parameter values, and the departures of these calculated values $\hat{N}_a$, $\hat{N}_m$ from the a priori values $\bar{N}_a$, $\bar{N}_m$ are found. The sensitivity of $\hat{N}_a$, $\hat{N}_m$ to uncertainty in T, ψ_o and ψ_r is thereby found.

II) error due to independent statistical fluctuations in the photon count at each detector.

Type II error is calculated by first finding the total mean number of photons incident on each detector. These totals are then given statistical noise which is the square root of the total signal, and the corresponding maximal departure of $\hat{N}_a$, $\hat{N}_m$ from the a priori values $\bar{N}_a$, $\bar{N}_m$ is found. This is sensitivity to number of photons in signal, and this sensitivity is a function of the ratio $\phi = \bar{N}_a/\bar{N}_m$ and the a priori solar signal $\bar{N}_s$.

Type I Error - Uncertainty in T, ψ_o and ψ_r

The following analysis considers deviations of $\hat{N}_m$, $\hat{N}_a$ from $\bar{N}_m$, $\bar{N}_a$ due to an uncertainty in the temperature T. The sensitivities of $\hat{N}_m$ and $\hat{N}_a$ due to uncertainties in the width of the emitted spectral line ψ_o, or the detuning of the laser with respect to the receiver ψ_r, are also given by the following analysis by simply replacing T with ψ_o or ψ_r.

The departure of $\hat{N}_m$ from $\bar{N}_m$ is defined by $\delta\hat{N}_m$, and the departure of $\hat{N}_a$ from $\bar{N}_a$ is defined by $\delta\hat{N}_a$. The departures $\delta\hat{N}_m(T)$ and $\delta\hat{N}_a(T)$ due to an uncertainty in T can be found by partial differentiation of Eqs. 4-3,18 such that

$$\delta\hat{N}_m(T) = \hat{S}_1' \cdot \frac{\partial c_{1m}}{\partial T}\,\delta T + \hat{S}_2' \cdot \frac{\partial c_{2m}}{\partial T}\,\delta T \qquad 4\text{-}3,20a$$

and

$$\delta\hat{N}_a(T) = \hat{S}_1' \cdot \frac{\partial c_{1a}}{\partial T}\,\delta T + \hat{S}_2' \cdot \frac{\partial c_{2a}}{\partial T}\,\delta T \qquad 4\text{-}3,20b$$

Approximating $\hat{S}_1'$ and $\hat{S}_2'$ by $(\bar{S}_1 - \mu_{1s}\bar{N}_s)$ and $(\bar{S}_2 - \mu_{2s}\bar{N}_s)$, and substituting Eqs. 4-3, 16 into Eqs. 4-3, 20

$$\delta\hat{N}_m(T) = (\mu_{1m}\frac{\partial c_{1m}}{\partial T}\,\delta T + \mu_{2m}\frac{\partial c_{2m}}{\partial T}\,\delta T)\bar{N}_m + (\mu_{1a}\frac{\partial c_{1m}}{\partial T}\,\delta T + \mu_{2a}\frac{\partial c_{2m}}{\partial T}\,\delta T)\bar{N}_a \qquad 4\text{-}3,21a$$

and

$$\delta\hat{N}_a(T) = (\mu_{1m}\frac{\partial c_{1a}}{\partial T} + \mu_{2m}\frac{\partial c_{2a}}{\partial T}\,\delta T)\bar{N}_m + (\mu_{1a}\frac{\partial c_{1a}}{\partial T}\,\delta T + \mu_{2a}\frac{\partial c_{2a}}{\partial T}\,\delta T)\bar{N}_a \qquad 4\text{-}3,21b$$

where it should be noted that actual values $\bar{N}_m$ and $\bar{N}_a$ are functions of atmospheric properties, and are not functions of T, ψ_o or ψ_r. The <u>fractional</u> error in the measurements due to an uncertainty in T can be estimated by dividing Eqs. 4-3,21 by $\bar{N}_m$ and $\bar{N}_a$, such that

$$\frac{\delta\hat{N}_m(T)}{\bar{N}_m} = (\mu_{1m}\frac{\partial c_{1m}}{\partial T}\,\delta T + \mu_{2m}\frac{\partial c_{2m}}{\partial T}\,\delta T) + \phi\cdot(\mu_{1a}\frac{\partial c_{1m}}{\partial T}\,\delta T + \mu_{2a}\frac{\partial c_{2m}}{\partial T}\,\delta T) \qquad 4\text{-}3,22a$$

and

$$\frac{\delta\hat{N}_a(T)}{\bar{N}_a} = (\mu_{1m}\frac{\partial c_{1a}}{\partial T}\,\delta T + \mu_{2m}\frac{\partial c_{2a}}{\partial T}\,\delta T)\cdot\phi^{-1} + (\mu_{1a}\frac{\partial c_{1a}}{\partial T}\,\delta T + \mu_{2a}\frac{\partial c_{2a}}{\partial T}\,\delta T) \qquad 4\text{-}3,22b$$

where $\phi = \bar{N}_a/\bar{N}_m$. Eqs. 4-3,22 allow us to estimate fractional errors in the measurements due to system parameter uncertainties <u>independent</u> of the absolute values of the signals $(\bar{S}_1 - \mu_{1s}\bar{N}_s)$ and $(\bar{S}_2 - \mu_{2s}\bar{N}_s)$.

The total type I error due to uncertainty in all three parameters T, ψ_o and ψ_r can be estimated by

$$\frac{\delta\hat{N}_m^I}{\bar{N}_m} = \left\{ \left(\frac{\delta\hat{N}_m(T)}{\bar{N}_m}\right)^2 + \left(\frac{\delta\hat{N}_m(\psi_o)}{\bar{N}_m}\right)^2 + \left(\frac{\delta\hat{N}_m(\psi_r)}{\bar{N}_m}\right)^2 \right\}^{1/2} \qquad 4\text{-}3,23a$$

and

$$\frac{\delta\hat{N}_a^I}{\bar{N}_a} = \left\{ \left(\frac{\delta\hat{N}_a(T)}{\bar{N}_a}\right)^2 + \left(\frac{\delta\hat{N}_a(\psi_o)}{\bar{N}_a}\right)^2 + \left(\frac{\delta\hat{N}_a(\psi_o)}{\bar{N}_a}\right)^2 \right\}^{1/2} \qquad 4\text{-}3,23b$$

The detector quantum efficiency q_e, and the solar signal $\bar{N}_s$ do not enter into either Eqs. 4-3,22 or 4-3,23.

Type II Error - Photon Statistics

The number of photons incident on detectors #1 and #2 have mean values $\bar{S}_1$ and $\bar{S}_2$ given by Eqs. 4-3,16. We can expect that the measured signals $\hat{S}_1$ and $\hat{S}_2$ reflect statistical fluctuations from these means, such that

$$\delta\hat{S}_1 \simeq \sqrt{\bar{S}_1} \qquad 4\text{-}3,24a$$

and $$\delta\hat{S}_2 \simeq \sqrt{\bar{S}_2} \qquad 4\text{-}3,24b$$

The effect of these statistical fluctuations on the measurements $\hat{N}_m$ and $\hat{N}_a$ can be found by taking the differential of Eqs. 4-3,18 as follows:

$$(\delta\hat{N}_m)^2 = (c_{1m}\delta\hat{S}_1)^2 + (c_{2m}\delta\hat{S}_2)^2 + (c_{1m}^2\,\mu_{1s}^2 + c_{2m}^2\,\mu_{2s}^2)\cdot(\delta\hat{N}_s)^2 \qquad 4\text{-}3,25a$$

and $$(\delta\hat{N}_a)^2 = (c_{1a}\delta\hat{S}_1)^2 + (c_{2a}\delta\hat{S}_2)^2 + (c_{1a}^2\,\mu_{1s}^2 + c_{2a}^2\,\mu_{2s}^2)\cdot(\delta\hat{N}_s)^2 \qquad 4\text{-}3,25b$$

The coefficients of the solar terms in Eqs. 4-3,25 are a sum of squares since the statistical fluctuations of solar photons at the two detectors are independent of each other. Substituting Eqs. 4-3,16 and 4-3,24 into Eqs. 4-3,25, it follows that

$$(\delta\hat{N}_m^{II})^2 = c_{1m}^2\cdot(\mu_{1m}\bar{N}_m + \mu_{1a}\bar{N}_a) \quad + c_{2m}^2\cdot(\mu_{2m}\bar{N}_m + \mu_{2a}\bar{N}_a) \qquad 4\text{-}3,26a$$

$$+[c_{1m}^2\mu_{1s}(1+\mu_{1s})+ c_{2m}^2\mu_{2s}(1+\mu_{2s})]\cdot\bar{N}_s$$

and

$$(\delta\hat{N}_a^{II})^2 = c_{1a}^2\cdot(\mu_{1m}\bar{N}_m + \mu_{1a}\bar{N}_a) + c_{2a}^2\cdot(\mu_{2m}\bar{N}_m + \mu_{2a}\bar{N}_a) \qquad 4\text{-}3,26b$$

$$+[c_{1a}^2\mu_{1s}(1+\mu_{1s})+ c_{2a}^2\mu_{2s}(1+\mu_{2s})]\cdot\bar{N}_s$$

Again letting $\phi = \bar{N}_a/\bar{N}_m$, the <u>fractional</u> error in the measurements due to rms statistical fluctuations can be estimated by dividing Eqs. 4-3,26 by $\bar{N}_m$ and $\bar{N}_a$, such that

$$\left(\frac{\delta\hat{N}_m^{II}}{\bar{N}_m}\right)^2 = \left\{(c_{1m}^2\,\mu_{1m} + c_{2m}^2\,\mu_{2m}) + \phi\cdot(c_{1m}^2\,\mu_{1a} + c_{2m}^2\,\mu_{2a}) \right. \qquad 4\text{-}3,27a$$

$$\left. + \frac{\bar{N}_s}{\bar{N}_m}\cdot[c_{1m}^2\,\mu_{1s}(1+\mu_{1s}) + c_{2m}^2\,\mu_{2s}(1+\mu_{2s})]\right\}\cdot(\bar{N}_m)^{-1}$$

$$= \frac{1}{\bar{N}_m}\cdot \mathrm{Deg}_m^2(\phi) + \frac{\bar{N}_s}{\bar{N}_m^2}\cdot \mathrm{Deg}_{ms}^2$$

$$\left(\frac{\delta\hat{N}_a^{II}}{\bar{N}_a}\right)^2 = \left\{(c_{1a}^2\mu_{1a} + c_{2a}^2\mu_{2a}) + \phi^{-1}\cdot(c_{1a}^2\mu_{1m} + c_{2a}^2\mu_{2m}) \right. \qquad 4\text{-}3,27b$$

$$\left. + \frac{\bar{N}_s}{\bar{N}_a}\cdot[c_{1a}^2\mu_{1s}(1+\mu_{1s}) + c_{2a}^2\mu_{2s}(1+\mu_{2s})]\right\}\cdot(\bar{N}_a)^{-1}$$

$$= \frac{1}{\bar{N}_a}\cdot \mathrm{Deg}_a^2(\phi) + \frac{\bar{N}_s}{\bar{N}_a^2}\cdot \mathrm{Deg}_{as}^2$$

The factors $Deg_m(\phi)$, $Deg_a(\phi)$ can be interpreted as those proportions to which the "natural" fractional statistical fluctuations $\bar{N}_m^{-\frac{1}{2}}$, $\bar{N}_a^{-\frac{1}{2}}$ are changed (increased) by the HSRL signal inversion process. The factors $Deg_m(\phi)$, $Deg_a(\phi)$ are both proportional to the inverse square root of the detector quantum efficiency q_e. The factors Deg_{ms}, Deg_{as} take into account the statistical degradation due to a solar background continuum.

4-3-g) A Study of Two Example HSRL Systems

This section presents calculations of HSRL system parameters c_{im} and c_{ia}, i = 1,2, and estimates of the sensitivity of the solutions to the parameters T, $\psi_o = \delta\sigma_o$ and $\psi_r = \sigma_o - \sigma_r$. The theory for these calculations was presented in sections 4-3-e) and 4-3-f). The calculations are performed for two HSRL systems which differ only in the fourth etalon spectral resolution, see Figure 4-9. The characteristics of both systems are given in Table 4-9. Drawings of the spectral profiles of the laser output and the two receiver system passbands as seen by both detectors are given in Figure 4-10.

The expected values $\hat{N}_m$ and $\hat{N}_a$ are calculated from the measurements $\hat{S}_1$ and $\hat{S}_2$ by means of Eqs. 4-3,18. The inversion coefficients c_{im} and c_{ia}, i = 1,2 are functions of T, ψ_o and ψ_r only. The inversion coefficient values are plotted versus departures of T from 250°K in Figure 4-11, versus departure of ψ_o from $\delta\sigma_o = 1/10\ \delta\sigma_D$ in Figure 4-12, and versus departures of $\psi_r = |\sigma_o - \sigma_r|$ from zero in Figure 4-13. All four inversion coefficients are given for both example systems. It should be noted from Figure 4-11 that these coefficients are relatively insensitive to changes in atmospheric temperature.

Estimates of Type I error versus uncertainty in T, ψ_o and ψ_r are given in Figures 4-14 through 4-16. The ordinates of Figures 4-14 through 4-16 are given in fractional error in measurement as given by Eqs. 4-3,22.

Table 4-9 Characteristics of the Two Example HSRL Receiver Systems

Wavelength	4880 Å
PEPSIOS FWHM High resolution etalon FWHM:	$\delta\sigma_{123} = \delta\sigma_D$(at 250°K) = .086 cm^{-1} ($\delta\lambda \sim 20$ mÅ)
System one	$\delta\sigma_4 = 1/5\ \delta\sigma_D$ = .017 cm^{-1} ($\delta\lambda \sim 4$mÅ)
System two	$\delta\sigma_4 = 1/2\ \delta\sigma_D$ = .043 cm^{-1} ($\delta\lambda \sim 10$mÅ)
Laser output FWHM	$\delta\sigma_o = 1/10\ \delta\sigma_D$ = .009 cm^{-1} ($\delta\lambda \sim 2$ mÅ)
Etalon coating absorption coefficient	A' = .01
Etalon coating reflection coefficient	R' = .91
Detector transmission coefficients	
System one	μ_{1m} = .24 μ_{2m} = .06
	μ_{1a} = .11 μ_{2a} = .22
System two	μ_{1m} = .17 μ_{2m} = .11
	μ_{1a} = .09 μ_{2a} = .24
Solar degradation coefficients†	
System one	Deg_{ms} = 5.0 Deg_{as} = 2.8
System two	Deg_{ms} = 6.8 Deg_{as} = 4.9

†The solar signal transmission coefficients μ_{1s} and μ_{2s} are approximated by μ_{1m} and μ_{2m}, respectively.

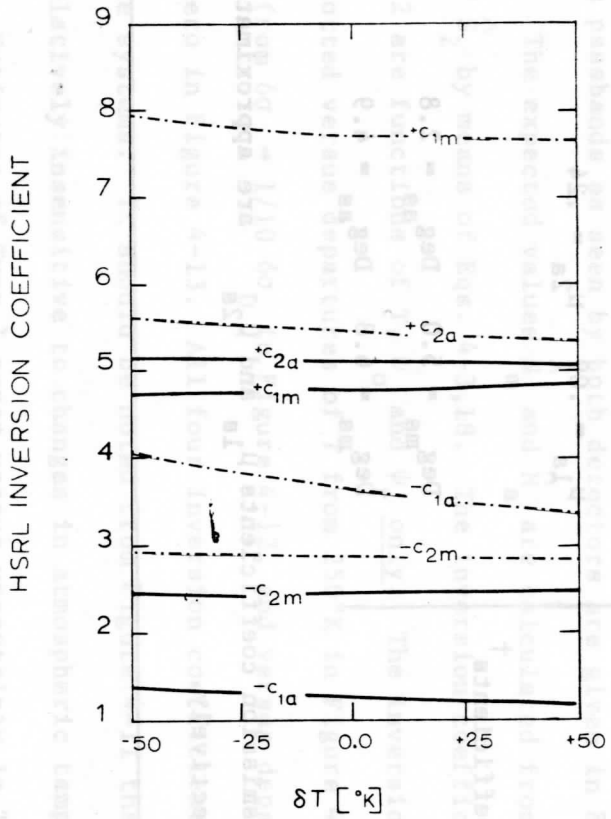

Figure 4-11 HSRL inversion coefficient values for system one (solid) and system two (dash) versus uncertainty in atmospheric temperature T.

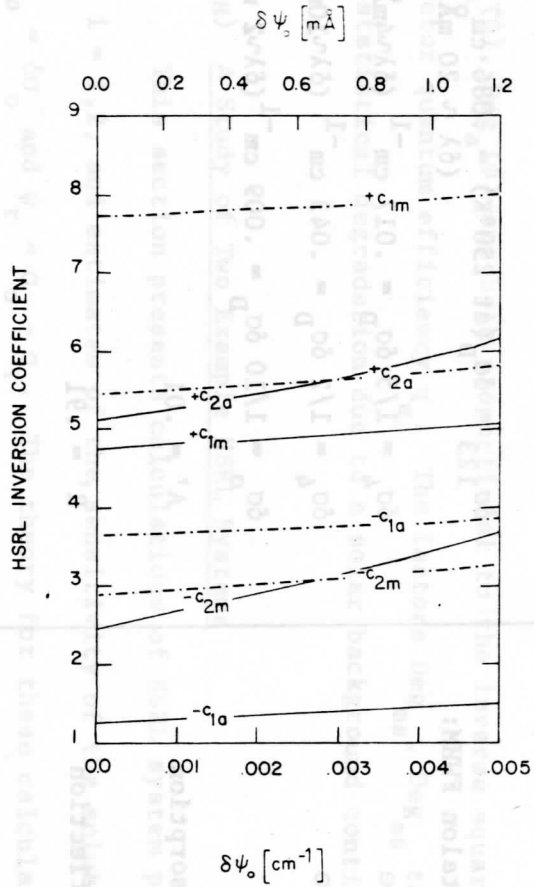

Figure 4-12 HSRL inversion coefficient values for system one (solid) and system two (dash) versus uncertainty in laser output resolution $\psi_o = \delta\sigma_o$.

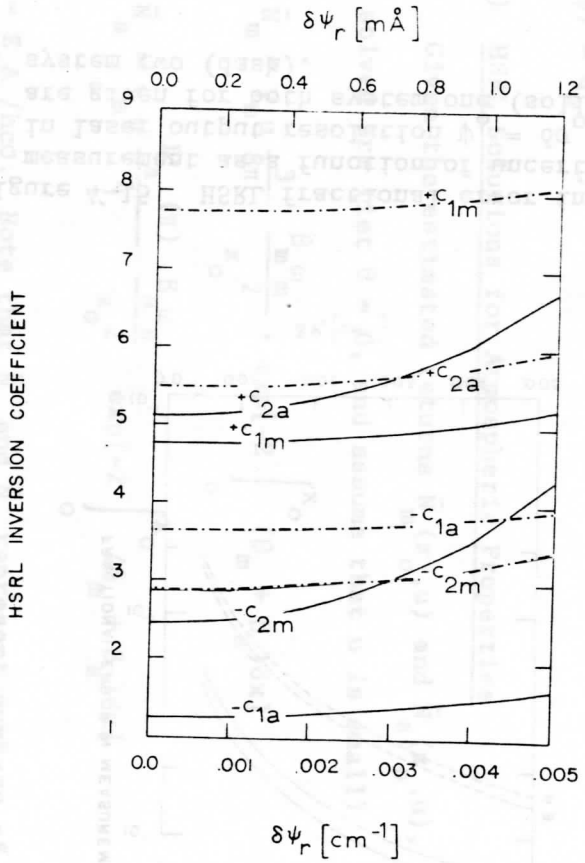

Figure 4-13 HSRL inversion coefficient values for system one (solid) and system two (dash) versus laser-receiver detuning $\psi_r = \sigma_o - \sigma_r$.

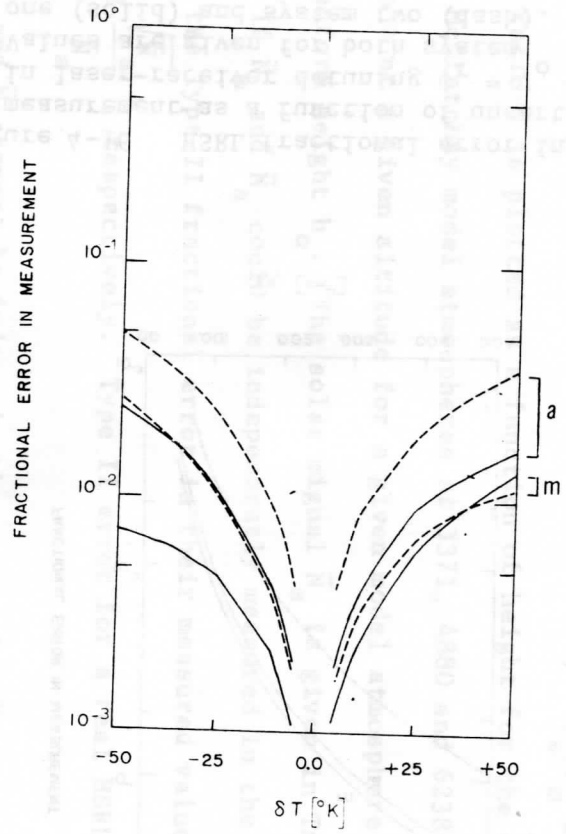

Figure 4-14 HSRL fractional error in measurement as a function of uncertainty in atmospheric temperature T. Values are given for both system one (solid) and system two (dash).

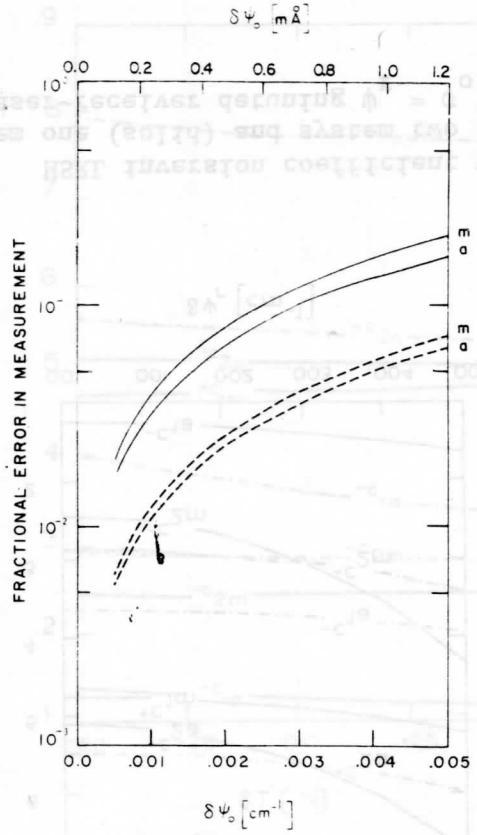

Figure 4-15 HSRL fractional error in measurement as a function of uncertainty in laser output resolution $\psi_o = \delta\sigma_o$. Values are given for both system one (solid) and system two (dash).

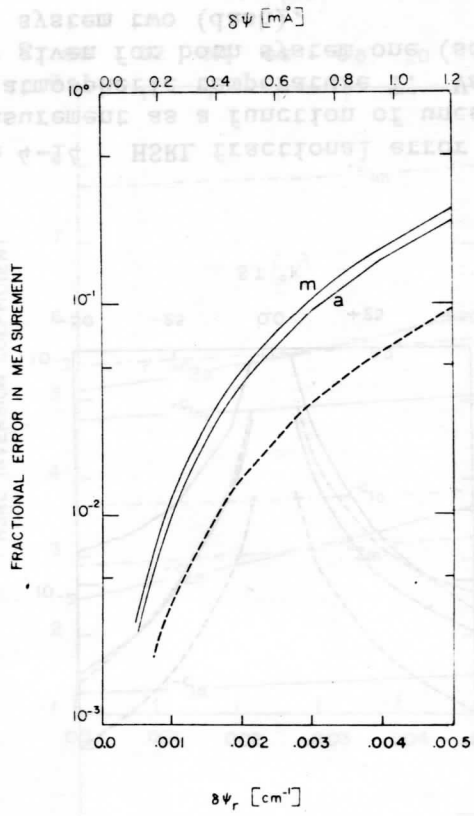

Figure 4-16 HSRL fractional error in measurement as a function of uncertainty in laser-receiver detuning $\psi_r = \sigma_o - \sigma_r$. Values are given for both system one (solid) and system two (dash).

Type I error estimates are given for both example systems. The total type I error due to uncertainty in T, ψ_o and ψ_r can be found by means of Eqs. 4-3,23.

Type II error is a function of the ratio $\phi = \bar{N}_a/\bar{N}_m$ and the solar signal $\bar{N}_s$. The ratio ϕ is plotted as a function of height for the Clear and Hazy Tropical McClatchey model atmospheres at 3371, 4880 and 6238 Å in Figure 4-17. The ratio ϕ at a given altitude for a given model atmosphere is independent of lidar platform height h_o. The solar signal $\bar{N}_s$ is given in Table 4-5.

If $\bar{N}_m$ and $\bar{N}_a$ could be independently measured in the absence of a solar signal, the Type II fractional error in their measured values would be $\frac{\sqrt{\bar{N}_m}}{\bar{N}_m}$ and $\frac{\sqrt{\bar{N}_a}}{\bar{N}_a}$, respectively. Type II error for a real HSRL is larger, however, since $\bar{N}_m$ and $\bar{N}_a$ cannot be independently measured. The factors $Deg_m(\phi)$, $Deg_a(\phi)$ by which the fractional error in the estimates $\hat{N}_m$, $\hat{N}_a$ are greater than $\frac{\sqrt{\bar{N}_m}}{\bar{N}_m}$, $\frac{\sqrt{\bar{N}_a}}{\bar{N}_a}$ are plotted in Figure 4-18 for the two example HSRL systems versus ϕ for $q_e = 1$. These factors are given by Eqs. 4-3,27, and note that $Deg(\phi) \propto q_e^{-1/2}$.

4-3-h) HSRL Solutions for Atmospheric Properties

Given the estimated returns $\bar{N}_m(x_o,u)$ and $\bar{N}_a(x_o,u)$, the lidar equations to be solved are (let $\theta = 0$, and assume that u is small)

$$\bar{N}_m = \gamma_m u \frac{3}{8\pi} \frac{\beta_m \omega_m}{x_o^2} \cdot \exp[-2\int_o^{x_o} (\beta_m + \beta_a)dx] \qquad 4\text{-}3,28a$$

$$\bar{N}_a = \gamma_a u \frac{\mathbb{P}_a(\pi)}{4} \frac{\beta_a \omega_a}{x_o^2} \exp[-2\int_o^{x_o} (\beta_m + \beta_a)dx] \qquad 4\text{-}3,28b$$

for $\gamma = E_o A_r/hc\sigma$. Note that $\bar{N}_m$ and $\bar{N}_a$ represent numbers of photons intercepted by the receiver, and that γ_m and γ_a are calibration constants. Various optical properties can be derived as follows:

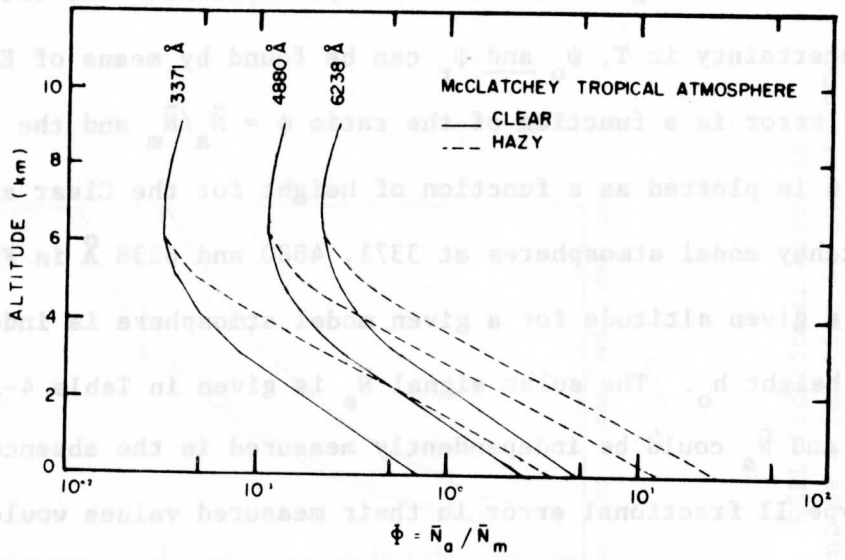

Figure 4-17 The ratio $\phi = \bar{N}_a/\bar{N}_m$ as a function of altitude for the McClatchey et al. (1971) Clear and Hazy model Tropical atmospheres. The ratio ϕ is independent of lidar platform height h_o.

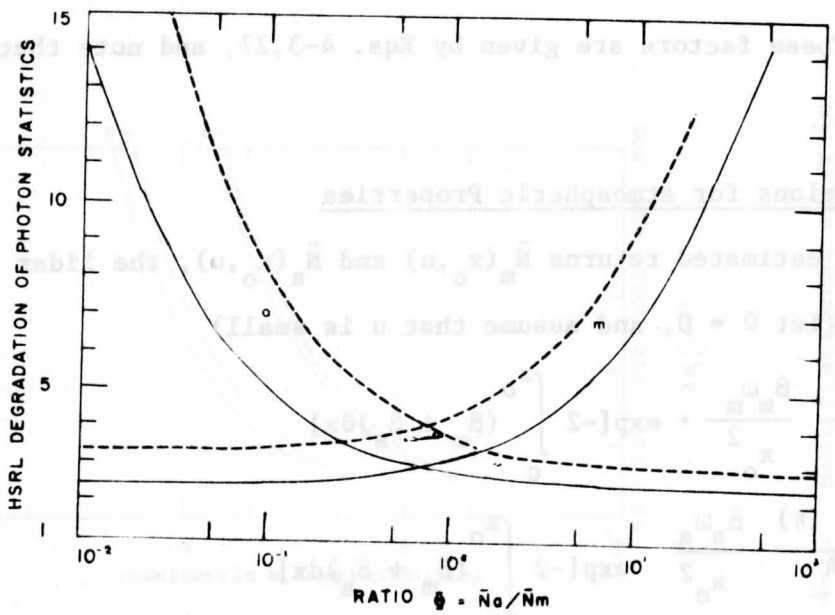

Figure 4-18 The HSRL statistical degradation factors $\mathrm{Deg}_m(\phi)$ and $\mathrm{Deg}_a(\phi)$ for system one (solid) and system two (dash) as a function of the ratio $\phi = \bar{N}_a/\bar{N}_m$ where $q_e = 1$. Note that $\mathrm{Deg}(\phi) \propto q_e^{-\frac{1}{2}}$.

i) average slab aerosol extinction coefficient

$$\overline{\beta_a}^{ij} = \frac{\tau_a(0,x_i) - \tau_a(0,x_j)}{x_i - x_j} \qquad 4\text{-}3,29a$$

ii) aerosol optical depth

$$\tau_a(0,x_o) = \int_o^{x_o} \beta_a \, dx = \tau(0,x_o) - \int_o^{x_o} \beta_m \, dx \qquad 4\text{-}3,29b$$

iii) integrated optical depth

$$\tau(0,x_o) = \int_o^{x_o} (\beta_m + \beta_a) dx = \frac{1}{2}\left[\ell n \frac{3}{8\pi} \gamma_m - \ell n \bar{N}_m \, x_o^2 + \ell n(\beta_m \omega_m \, u) \right] \qquad 4\text{-}3,29c$$

iv) scattering ratio

$$S = 1 + \left[\frac{I\!P_a(\pi)}{4\pi} \beta_a \, \omega_a \Big/ \frac{3}{8\pi} \beta_m \, \omega_m \right] = 1 + \frac{\bar{N}_a \, \gamma_m}{\bar{N}_m \, \gamma_a} \qquad 4\text{-}3,29d$$

v) aerosol volume backscattering coefficient

$$\frac{B_a(\pi)}{4\pi} = \frac{I\!P_a(\pi)}{4\pi} \beta_a \, \omega_a = (S-1) \frac{3}{8\pi} \beta_m \, \omega_m \qquad 4\text{-}3,29e$$

vi) average slab aerosol phase function for backscattering

$$\frac{\overline{I\!P_a(\pi)}^{ij}}{4\pi} = \frac{B_a(\pi)}{4\pi} \left[\omega_a \, \overline{\beta_a}^{ij} \right]^{-1} \qquad 4\text{-}3,29f$$

The albedo for single scattering is approximately 1 at visible wavelengths, but departs significantly from 1 due to O_3 absorption in the UV. Typical values for $1 - \omega_m$ as a function of altitude for $\lambda = 3371\text{Å}$ are given in Figure 4-19. The data of Figure 4-19 were computed using the McClatchey Tropical model atmosphere. Assuming that the albedo for single scattering for aerosols and Rayleigh scatterers is a sufficiently well known quantity below 10 km, then the above solutions (Eqs. 4-3,29) determine three unknowns (β_m, β_a, $I\!P_a(\pi)$) from two measurements ($\hat{N}_m$, $\hat{N}_a$). A third measurement is required to solve these equations, and we therefore require

that an independently measured temperature profile T be provided as a function of height. As shown in Appendix 4-I, the profile of β_m can be determined from T in a dry atmosphere with an accuracy $\frac{\delta\beta_m}{\beta_m} \lesssim 2\,\frac{\delta T}{T}$. The uncertainty in the calculated value for Rayleigh optical depth

$$\tau_m\,(0,x_o) = \int_o^{x_o} \beta_m\, dx \qquad 4\text{-}3,30$$

is

$$[\delta\tau_m\,(0,x_o)]^2 = (\frac{\delta\beta_m}{\beta_m})^2 \cdot (\int_o^{x_o} \beta_m\, dx)^2 \cong 4(\frac{\delta T}{T})^2 \cdot [\tau_m\,(0,x_o)]^2$$

where it has been assumed that $(\frac{\delta\beta_m}{\beta_m})$ is a constant independent of height.

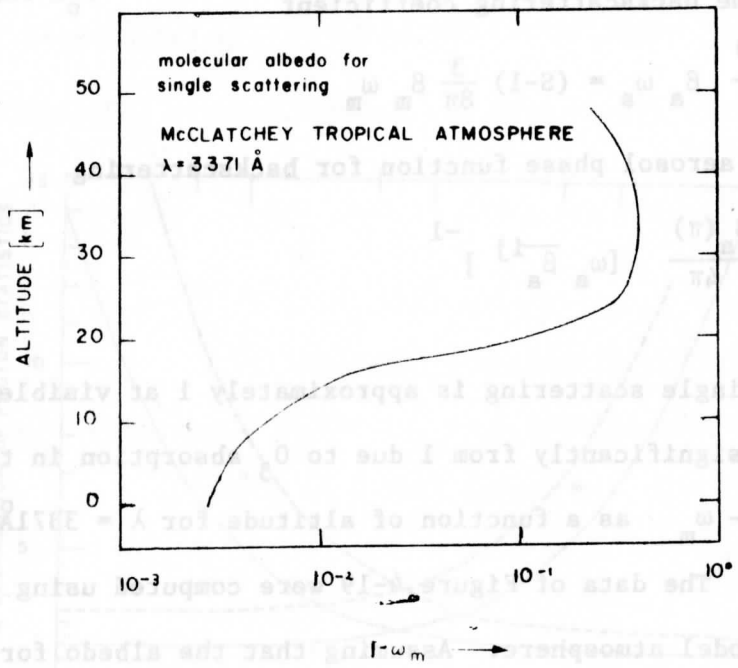

Figure 4-19 Typical values for the molecular albedo for single scattering $1 - \omega_m$ as a function of altitude, from the McClatchey et al. (1971) Tropical model atmosphere at 3371 Å.

The errors are as follows:

i) average slab aerosol extinction coefficient (from 4-3,29a)

$$[\delta\bar{\beta}_a^{ij}]^2 = \frac{1}{(x_i - x_j)^2}\{[\delta\tau_a(0,x_i)]^2 + [\delta\tau_a(0,x_j)]^2\} \qquad 4\text{-}3,31a$$

ii) aerosol optical depth (from 4-3,29b)

$$[\delta\tau_a(0,x_o)]^2 = [\delta\tau(0,x_o)]^2 + [\delta\tau_m(0,x_o)]^2 \qquad 4\text{-}3,31b$$

iii) integrated optical depth (from 4-3,29c)

$$[\delta\tau(0,x_o)]^2 = \frac{1}{4}\left[\left(\frac{\delta\gamma_m}{\gamma_m}\right)^2 + \left(\frac{\delta\bar{N}_m}{\bar{N}_m}\right)^2 + \left(\frac{\delta\beta_m}{\beta_m}\right)^2 + \left(\frac{\delta\omega_m}{\omega_m}\right)^2\right] \qquad 4\text{-}3,31c$$

iv) scattering ratio (from 4-3,29d)

$$\left(\frac{\delta S}{S}\right)^2 = \left(\frac{\delta\bar{N}_m}{\bar{N}_m}\right)^2 + \left(\frac{\delta\bar{N}_a}{\bar{N}_a}\right)^2 + \left(\frac{\delta\gamma_m}{\gamma_m}\right)^2 + \left(\frac{\delta\gamma_a}{\gamma_a}\right)^2 \qquad 4\text{-}3,31d$$

v) aerosol volume backscattering coefficient (from 4-3,29e)

$$\left(\frac{\delta B_a(\pi)}{B_a(\pi)}\right)^2 = \left(\frac{\delta S}{S}\right)^2 + \left(\frac{\delta\beta_m}{\beta_m}\right)^2 + \left(\frac{\delta\omega_m}{\omega_m}\right)^2 \qquad 4\text{-}3,31e$$

vi) average slab aerosol phase function for backscattering (from 4-3,29f)

$$\left(\frac{\delta\overline{P_a(\pi)}^{ij}}{\overline{P_a(\pi)}^{ij}}\right) = \left(\frac{\delta B_a(\pi)}{B_a(\pi)}\right)^2 + \left(\frac{\delta\bar{\beta}_a^{ij}}{\bar{\beta}_a^{ij}}\right)^2 + \left(\frac{\delta\omega_a}{\omega_a}\right)^2 \qquad 4\text{-}3,31f$$

Substituting Eqs. 4-3,30, 4-3,31b and 4-3,31c into 4-3,31a, and letting $\frac{\delta\beta_m}{\beta_m} = 2(\frac{\delta T}{T})$ and $(x_i - x_j) = u$, then Eq. 4-3,31a can be written

$$\overline{\delta\beta_a^{ij}} = \frac{1}{u\sqrt{2}} \left\{ (\frac{\delta\gamma_m}{\gamma_m})^2 + (\frac{\delta N_m}{N_m})^2 + (\frac{\delta\omega_m}{\omega_m})^2 + 4[1 + 4\tau_m^2(o,x_o)] \cdot (\frac{\delta T}{T})^2 \right\}^{\frac{1}{2}} \qquad 4\text{-}3,32a$$

where we substitute $(\frac{\delta\bar{N}_m}{\bar{N}_m})^2 = (\frac{\delta\hat{N}_m^I}{\bar{N}_m})^2 + (\frac{\delta\hat{N}_m^{II}}{\bar{N}_m})^2$ from section 4-3-f). The factor $\tau_m(o,x_o)$ can be neglected since $4\tau_m(o,x_o)^2 << 1$. Letting $\frac{\delta\gamma_m}{\gamma_m} = \frac{\delta\omega_m}{\omega_m}$, then $\overline{\delta\beta_a^{ij}}$ is a function of u, $\frac{\delta\bar{N}_m}{\bar{N}_m}$ (or $\frac{\delta\hat{N}_m}{\bar{N}_m}$), $\frac{\delta\gamma_m}{\gamma_m}$ and $\frac{\delta T}{T}$, such that

$$(\overline{\delta\beta_a^{ij}})^2 = \frac{1}{2u^2}\left[(\frac{\delta\hat{N}_m^I}{\bar{N}_m})^2 + (\frac{\delta\hat{N}_m^{II}}{\bar{N}_m})^2 + 2(\frac{\delta\gamma_m}{\gamma_m})^2 + 4(\frac{\delta T}{T})^2\right] \qquad 4\text{-}3,32b$$

The HSRL instrumental error $\frac{\delta\hat{N}_m^I}{\bar{N}_m}$, given by Eq. 4-3,23a, is due to the uncertainry in the parameters T, ψ_o and ψ_r. Partial errors due to uncertainty in T, ψ_o and ψ_r are given for the example HSRL systems in Figures 4-14 through 4-16. For example, these figures show the following errors for Systems one and two (4880Å):

$\frac{\delta\hat{N}_m(T)}{\bar{N}_m}$ = 0.10% (one), = 0.15% (two)

for $\delta T = \pm 5°K$

$\frac{\delta\hat{N}_m(\psi_o)}{\bar{N}_m}$ = 2.0% (one), = 0.5% (two)

for $\delta\psi_o = 5 \times 10^{-4} cm^{-1}$ ($\simeq$ 0.1 mÅ)

$\frac{\delta\hat{N}_m(\psi_r)}{\bar{N}_m}$ = 0.5% (one), = 0.1% (two)

for $\delta\psi_r = 5 \times 10^{-4} cm^{-1}$ ($\simeq$ 0.1 mÅ)

The HSRL calibration constant can be determined accurately, such that

$$\frac{\delta\gamma_m}{\gamma_m} \simeq 0.5\% \ .$$

Temperature profiles averaged over a 1 km vertical resolution interval can be determined to a one percent accuracy from the inversion of infrared and microwave satellite radiometer data, see Westwater and Strand (1972). Hence, the uncertainty in atmospheric temperature is

$$\frac{\delta T}{T} \simeq 1.0\%$$

The quantity $\delta\bar{\beta}_a^{ij}$ is given for various values of u and $\frac{\delta\hat{N}_m^{II}}{\bar{N}_m}$ in Table 4-10, given the above values for $\frac{\delta\hat{N}_m^{I}}{\bar{N}_m}$, $\frac{\delta\gamma_m}{\gamma_m}$ and $\frac{\delta T}{T}$.

Table 4-10 Typical Values for $\delta\bar{\beta}_a^{ij}$ (km^{-1}) as a Function of $u = (x_i - x_j)$ and $\frac{\delta\hat{N}_m}{\bar{N}_m}$.

$\frac{\delta\hat{N}_m}{\bar{N}_m}$	u = 100 m	200 m	500 m	1 km
1%	.235 km^{-1}	.117 km^{-1}	.047 km^{-1}	.023 km^{-1}
3%	.308	.154	.062	.031
10%	.742	.371	.148	.074

Error due to statistical fluctuations is a function of the ratio $\phi = \bar{N}_a/\bar{N}_m$, the number of photons which are backscattered by molecules $\bar{N}_m$, and the number of solar photons $\bar{N}_s$. The ratio ϕ can be determined as a function of height from Figure 4-17, the total number of collected photons which are scattered by molecules can be determined from either Figures 4-3 or 4-4, and the solar signal can be determined from Table 4-5. The statistical degradation factor $Deg_m(\phi)$ can be determined from Figure 4-18. The factor Deg_{ms} is given in Table 4-9. The error due to statistical fluctuations is then

$$\left(\frac{\delta\hat{N}_m^{II}}{\bar{N}_m}\right)^2 = \frac{1}{\bar{N}_m} \cdot Deg_m^2(\phi) + \frac{\bar{N}_s}{\bar{N}_m^2} \cdot Deg_{ms}^2 \qquad 4\text{-}3,33$$

Letting $\bar{N}_m = \frac{d\bar{N}_m}{dt} \cdot \Delta t_m$, the signal integration time required to obtain a specified statistical precision in the molecular return is

$$\Delta t_m = \frac{1}{\frac{d\bar{N}_m}{dt}} \cdot \frac{Deg_m^2(\phi) + (\bar{N}_s/\bar{N}_m) \cdot Deg_{ms}^2}{\left(\frac{\delta\hat{N}_m^{II}}{\bar{N}_m}\right)^2} \qquad 4\text{-}3,34$$

The type II or statistical error $\left(\frac{\delta\hat{N}_m^{II}}{\bar{N}_m}\right)^2$ can be determined as a function of $\delta\bar{\beta}_a^{ij}$ from Eq. 4-3,34.

The precision to which $\delta\bar{\beta}_a^{ij}$ must be determined in a 1 km vertical interval in order to obtain an accuracy of ± 0.2 °K day^{-1} and ± 0.5 °K day^{-1} in the total daily heating over land was estimated in Tables 3-1 and 3-2, respectively. These results are used to obtain estimates of the HSRL signal integration time for the model HSRL systems one and two (Table 4-9) located at h_o = 185 km (Shuttle case) and h_o = 10 km (aircraft case). The signal integration times are given as a function

of height in Table 4-11 for the cases of a McClatchey Tropical Clear (BF = 1) and Hazy (BF = 5) model atmosphere. The signal integration time, Δt_m, is most sensitive to the statistical degradation factor $Deg_m(\phi)$. The HSRL model system one is defined to a greater spectral resolution than system two, and it has a correspondingly lower value for $Deg_m(\phi)$. System one can therefore operate at lower laser power levels to attain a specified statistical precision in the molecular return signal. The calculations of Table 4-11 were performed using the worst case solar background as given in Table 4-5. The solar background was reduced an order of magnitude for the Shuttle case to characterize HSRL operation within a Fraunhofer line. The values for Δt_m calculated without a solar signal are also given in Table 4-11. The length of this sample path on the Earth's surface, assuming that the Shuttle orbit is circular and that the aircraft speed is 800 km/hr, is also given in Table 4-11.

4-4 Lidar Methods to Measure Aerosol Profiles

4-4-a) System I: High Spectral Resolution Lidar

The High Spectral Resolution Lidar (or HSRL) concept was presented in Section 4-3. An envisioned HSRL system would employ an N_2 laser to pump a dye cell, which is tuned to yield a narrow spectral line by means of Fabry-Perot etalons. A high resolution receiver which employs Fabry-Perot etalons is also required. Independently derived temperature profiles are required to provide vertical profiles of the Rayleigh scattering cross section. Eqs. 4-3,32 suggest that temperature profiles derived from the inversion of data from passive satellite borne sensors will suffice for this purpose.

Source: N_2 superadiant (3371Å) laser pumping a dye (4000-5000 Å) in a laser-etalon-amplifier configuration with an on-axis etalon. Spectral width of 0.002 Å. Energy per pulse ≃ 50 μJ. Repetition rate = 60 Hz. Pulse duration = 7ns. Energy conversion efficiency = (0.1% N_2 conversion) x (30% N_2-dye conversion) ≃ 0.03%.

Table 4-11 Signal Integration Time and Sample Path Length for Model HSRL System ONE Located at Shuttle and Aircraft Altitudes.[1]

Altitude (km)	± 0.2°K day^{-1} Accuracy[2] Shuttle (h_o = 185 km)[3] Δt_m(sec)	Δs(km)	Aircraft (h_o = 10 km)[4] Δt_m(sec)	Δs(m)	± 0.5°K day^{-1} Accuracy[2] Shuttle (h_o = 185 km)[3] Δt_m(sec)	Δs(km)	Aircraft (h_o = 10 km)[4] Δt_m(sec)	Δs(m)
With Worst Case Solar Signal[5]								
McClatchey Tropical Clear Model Atmosphere (BF = 1)								
0	8.31	62.8	.077	17.1	.375	2.83	.003	.668
1	9.36	70.7	.138	30.7	49.1	371.	.614	136.
2	47.0	355.	1.15	256.	18.5	140.	.372	82.7
3	5.95	45.0	.235	52.1	20.3	153.	.635	141.
4	16.0	120.	.781	173.	11.7	88.8	.445	98.8
5	41.5	313.	1.86	414.	2.22	16.8	.076	16.9
McClatchey Tropical Hazy Model Atmosphere (BF = 5)								
0	23.7	179.	.058	12.9	57.3	433.	.123	27.2
1	.467	3.53	.002	.406	.041	.313	.001	.032
2	4.83	36.5	.035	7.72	6.55	49.5	.040	8.97
3	1.46	11.0	.019	4.30	2.15	16.2	.023	5.17
4	9.73	73.5	.233	51.7	5.73	43.3	.107	23.8
5	1.68	12.7	.061	13.5	1.01	7.66	.028	6.19
Without Solar Signal[5]								
McClatchey Tropical Clear Model Atmosphere (BF = 1)								
0	7.74	58.5	.077	17.0	.302	2.28	.003	.664
1	8.63	65.2	.137	30.3	38.3	290.	.608	135.
2	42.4	321.	1.12	250.	13.7	103.	.364	80.8
3	5.29	40.0	.225	49.9	14.3	108.	.609	135.
4	14.0	106.	.737	163.	7.98	60.3	.420	93.2
5	36.0	272.	1.76	391.	1.47	11.1	.072	16.0
McClatchey Tropical Hazy Model Atmosphere (BF = 5)								
0	22.2	168.	.058	12.9	46.9	354.	.122	27.2
1	.442	3.34	.002	.405	.035	.264	.001	.032
2	4.49	33.9	.035	7.69	5.22	39.4	.040	8.93
3	1.32	9.98	.019	4.24	1.58	12.0	.023	5.11
4	8.57	64.8	.226	50.3	3.95	29.9	.104	23.2
5	1.46	11.0	.058	12.9	.668	5.04	.027	5.90

Table 4-11 (cont.)

(1) The model HSRL systems are defined in Table 4-9 (λ = 4880 Å). Additional model parameters are as follows:

$q_e = 0.25$

$A_r = 1.0\ m^2$ (Shuttle)

$= 0.1\ m^2$ (Aircraft)

$\pm 0.2°K\ day^{-1}$ accuracy:

$E_o = 10\ mj\ sec^{-1}$ (System one) @ 60 Hz repitition rate

$= 20\ mj\ sec^{-1}$ (System two) @ 60 Hz repitition rate

$u = 1.0\ km$

$\pm 0.5°K\ day^{-1}$ accuracy:

$E_o = 3\ mj\ sec^{-1}$ (System one) @ 60 Hz repitition rate

$= 6\ mj\ sec^{-1}$ (System two) @ 60 Hz repitition rate

$u = 0.75\ km$

The worst case solar signal from Table 4-5 is included.

(2) Values for $|\Delta\beta_a|$ are taken from Tables 3-1 and 3-2, and correspond to an uncertainty of $\pm 0.2°K\ day^{-1}$ and $\pm 0.5°K\ day^{-1}$ in the total daily heating over land. The model atmosphere parameter BF = 1 and BF = 5 correspond to the McClatchey Clear and Hazy model atmospheres, respectively. The values for $|\Delta\beta_a|$ and $\phi = \bar{N}_a/\bar{N}_m$ are as follows:

	McClatchey Tropical Clear			McClatchey Tropical Hazy		
Altitude (km)	ϕ	$\lvert\Delta\beta_a\rvert^a$ (km^{-1})	$\lvert\Delta\beta_a\rvert^b$ (km^{-1})	ϕ	$\lvert\Delta\beta_a\rvert^a$ (km^{-1})	$\lvert\Delta\beta_a\rvert^b$ (km^{-1})
0	2.4	.08	1.1	10.	.13	.25
1	1.3	.06	.08	4.4	.43	4.3
2	.62	.03	.11	1.8	.09	.23
3	.31	.06	.10	.73	.13	.33
4	.18	.04	.13	.29	.05	.19
5	.13	.03	.30	.14	.11	.45

[a] $\pm 0.2°K\ day^{-1}$ accuracy

[b] $\pm 0.5°K\ day^{-1}$ accuracy

(3) For the Shuttle case, the sample path length along the Earth's surface is $\Delta s = \bar{R}_E \dot{\theta} \Delta t$, where the angular velocity for a circular orbit is $\dot{\theta} = \frac{GM_E}{a^3}$

and $a = \bar{R}_E + h_o$

$\bar{R}_E$ = mean Earth radius = 6.4×10^3 km

G = gravitational constant = $6.67 \times 10^{-20}\ km^3 sec^{-2} kg^{-1}$

M_E = mass of the Earth = 5.98×10^{24} kg .

for h_o = 185 km, $\dot{\theta} = 7.56\ km\ sec^{-1}$.

(4) The aircraft velocity over the Earth's surface is assumed to be 800 km hr^{-1}.

(5) Solar signal values are derived from Table 4-5 (λ = 4880 Å). Solar signal values for the Shuttle case were reduced an order of magnitude to characterize HSRL operation within a Fraunhofer line.

Receiver: Four etalon system for high resolution (0.002 Å) notch and spike and high rejection of scattered solar continuum. Transmittance of instrument ≃ 35%. Quantum efficiency of photomultipliers ≃ 30%.

Overall Efficiency ≃ .003%.

In order to achieve stable wavelength outputs as narrow as a few milli-angstroms at high power it appears necessary to use low feedback in the laser system in order to avoid being locked into laser cavity modes. The wavelength of the cavity modes depends critically on inhomogeneities in the dye cell and the separation of the laser cavity mirrors. The separation needed between laser cavity mirrors is generally so large that a linewidth much narrower than needed is produced.

Wallerstein and Hänsch (1975) recently reported that an N_2 pumped dye laser-amplifier system is capable of linewidths as narrow as 0.006 cm^{-1} (1.5 mÅ at 4800 Å) with pulse energies of 500 μj when pumped by a 10 mj, 10 nsec pulse from the N_2 laser pump. Projecting this conversion efficiency to the case of a 0.3 watt N_2 laser (average power for 10 nsec pulse lengths at a 60 Hz repetition rate), it appears that high resolution (1.5 mÅ) output from the dye laser-amplifier may be feasible with an average power of 15 mw. This would be adequate for the proposed HSRL system.

The envisioned laser system is configured as follows: The original design of Hänsch (1972) for an N_2 pumped dye laser is employed. This design consists of a dye cell enclosed in a cavity which includes an uncoated flat end window, the N_2 laser pumped circulating dye cell, a beam-expanding telescope, an intracavity etalon and a high blaze-angle echelle grating end reflector. The output of the dye laser is coupled through a wide-spaced confocal Fabry-Perot etalon into two amplifier dye cells in succession. Each

dye cell does not require a resonant cavity and each is pumped by a fraction of the same N_2 laser pulse which initiated the dye laser operation. The output of this system has a spectral width determined largely by the width of the transmission peak of the external wide-spaced etalon, and by the effects of Heisenberg broadening due to the extremely short duration of N_2 pump excitation. An attractive feature of this system is the absence of cavity modes other than those of the external resolving etalon, and precise tuning of the laser-amplifier output to the high resolution PEPSIOS receiver appears feasible.

Preliminary work has been carried out at the University of Wisconsin Physics Department to investigate the possibility of using such a laser-amplifier system for the HSRL project. Several dye laser-amplifier configurations have been tested. The most promising configuration employs an N_2 pumped dye laser of essentially the original Hänsch design, with the output coupled through an air-spaced plane Fabry-Perot etalon to a single dye amplifier cell. The output of this dye laser amplifier configuration is shown in Figure 4-20. The resolving (external) etalon used an etalon spacing of 9 mm with a coating finesse of 30. An amplified output of 3.5 mwatt (average power with a 10 nsec pulse length at 60 Hz operation) was obtained using a 0.12 watt (average power) N_2 laser pump. The spectral profile of the output closely follows the transmission profile of the 9 mm spaced resolving etalon which has a measured width of 5 mÅ at 4800 Å. We expect that future work with a resolving etalon of wider spacing (higher spectral resolution) will allow a reduction of the spectral width to the requirements of the HSRL system.

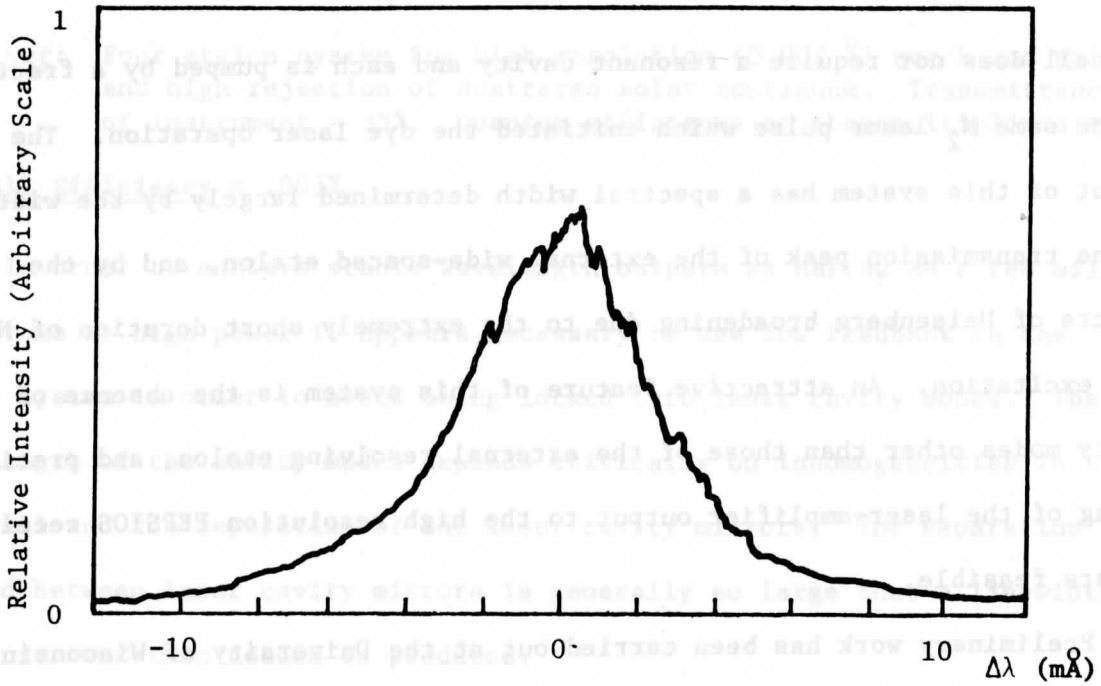

Figure 4-20. High resolution interferometer scan of N_2 pumped dye laser output, showing spectral width of 5 mÅ (FWHM) at 4880 Å. Average power of the amplified output was 3.5 mwatt with a 10 nsec pulse length at a 60 Hz repitition rate.

We have not had an opportunity to investigate flashlamp pumped dye systems to determine whether our requirements could be achieved with them. Their generally much longer pulses (100ns or more compared to $\sim$ 3 ns) may make it difficult to attain efficient operation while avoiding ultra-narrow but unstable cavity modes. Generally, the overall efficiency of conventional flashlamp-pumped dye systems is higher than for N_2 laser-pumped systems.

Some considerations regarding this technique:

Pro:

1) The aerosol extinction coefficient β_a is uniquely determined at a particular wavelength.

2) The instrumental requirements have been demonstrated in the laboratory.

3) The science of laser remote sensing of the atmosphere by means of ground and aircraft based lidars is promoted by research in this area.

4) Solar heating rate computations require information about β_a over a broad wavelength range. If multispectral imagery with high spatial resolution is available, then the technique described in Appendix IV-2 can be used to derive the total optical thickness of the aerosols as a function of wavelength. If it is assumed that the aerosol size and composition are independent of altitude then β_a can be inferred as a function of wavelength for $0.3\mu m \lesssim \lambda \lesssim 2.5\mu m$. Passive polarization measurements such as those proposed for the Nimbus G-ERB experiment by Stowe and Hilleary (1975) may also provide information on aerosol sizes. It should be noted, however, that the analysis of such data may be ambiguous (see the remarks by Kuriyan in the reference cited above).

Con:

1) Infrared heating rate computations require prior knowledge regarding aerosol composition and size distributions before the β_a values derived at solar wavelengths can be introduced into a GCM. This problem is common to all of the lidar techniques which are presented in this section.

2) Return optical power levels are marginal at Shuttle ranges. However, high resolution laser technology is expected to advance over the coming years.

3) Receiver optics is sophisticated, and <u>may</u> require frequent maintenance. Engineering developments should assure reliability by the time that the Shuttle mission will occur.

These considerations render the HSRL technique most attractive for ground and aircraft applications. The HSRL technique is somewhat marginal for Shuttle applications, but the present limitations may become less compelling in the near future.

4-4-b) System II: Multi-Wavelength, Low Spectral Resolution Lidar

This system employs an array of three or four flash lamp pumped dye lasers, fired sequentially at a high repetition rate. It may alternatively employ an N_2 laser to pump four dye cells. Photomultipliers measure returns at each wavelength $\lambda_j (j = 1,\ldots,4)$. Each wavelength band is defined within $\delta\lambda \simeq 1$ Å resolution.

Source: Multiple wavelengths by sequential firing of flash lamp pumped dye cells. Alternatively, multiple wavelengths by superposition of output from multiple dye cavities pumped by a common N_2 laser. Spectral width of each line = 1Å. Energy per pulse (all wavelengths) = 50μJ. Separation of lines ≃ 1000 Å in the range from 4000 to 7000 Å. Repetition rate = 1 Hz (flash lamp), = 60 Hz(N_2). Pulse duration = 20ns (flash lamp), = 7ns(N_2). Energy conversion efficiency ≃ 0.3% (flash lamp), ≃ 0.03% (N_2)

Receiver: One interference filter (1 Å resolution) per wavelength. Filter transmittance ≃ 50%. Average quantum efficiency of photomultipliers≃30%.

Overall Efficiency: ≃ 0.01% for N_2 pumped system, 0.1% for flash lamp pumped system.

Theory:

This scheme measures

$$S_{\lambda,j} = \frac{N_j x_o^2}{\varepsilon_{o,j}} = \left(I\!P_{a,j}^{(\pi)} \beta_{a,j} + \frac{3}{2} \beta_{m,1} \left(\frac{\lambda_1}{\lambda_j}\right)^4 \right) \exp\left[- \int_o^{x_o} \left(\beta_{a,j} + \beta_{m,1} \left(\frac{\lambda_1}{\lambda_j}\right)^4\right) dx \right] \qquad 4\text{-}4,1$$

Four such measurements are taken at λ_j $(1 \leq j \leq 4)$. The Rayleigh extinction profile is independently measured (e.g. from radiometric inversions). The aerosol backscattering phase functions and the extinction coefficient are assumed to be of the form:

$$I\!P_{a,j}^{(\pi)} = A\lambda_j^B \qquad 4\text{-}4,2a$$

and

$$\beta_{a,j} = C\lambda_j^D \qquad 4\text{-}4,2b$$

Thus the method yields four numbers for each layer, viz A,B,C,D. If the aerosol size distribution and composition are slowly varying functions of altitude, some of these numbers may be independent of altitude and the equations will be overdetermined.

Pro:

1) The technology is relatively unsophisticated. Flash lamp pumped dye lasers have been flown on aircraft.

2) The power utilization efficiency of flash lamp pumped systems is approximately .1%, which is convenient for remote stations with restricted power sources.

3) An estimate of aerosol size can be derived directly.

Con:

1) Prior knowledge of the optical properties of aerosols is required to constrain the choice of solutions to power laws; i.e. the representation $\beta_{a,j} = C\lambda_j^D$ assumes that the aerosol size distribution obeys a power law.

2) Prior knowledge regarding aerosol composition is still required to incorporate results into GCM.

3) The lifetime of the flash lamps or optical components subject to high peak powers may be restrictive.

4) The simultaneous operation of four laser systems may be operationally difficult.

5) The science of remote sensing of the atmosphere by means of lasers will not be significantly advanced.

4-4-c) System III: Angular Scanning System

A lidar system is considered which alternately fires toward nadir and at an angle ahead of the vehicle which transports the lidar. The same volume of atmosphere is thus probed at two angles at slightly different times.

DeLuisi et al. (1975) have explored a ground based lidar system which utilizes a combination of the multiple wavelength and multiple angle approaches.

Theory:

Given a lidar system which measures $\bar{N}_\theta = \bar{N}_m + \bar{N}_a$ from the same atmospheric volume at angles θ_1 and θ_2, the lidar equations to be solved are

$$N(\theta_k) = \frac{\gamma_\theta}{x_o^2 \sec\theta_k} \left(\frac{3}{8\pi} \beta_m \omega_m + \frac{P_a(\pi)}{4\pi} \beta_a \omega_a\right) \cdot \exp\left[-2 \sec\theta_k \int_o^{x_o} (\beta_m + \beta_a) dx'\right] \quad 4\text{-}4,3$$

for $k = 1,2$ and $\gamma_\theta = \frac{E_o A_r \eta_r u}{hc\sigma}$. Assuming that the range interval u is independent of pointing angle, and that the atmosphere is horizontally homogeneous on the average in the region of interest, the various optical properties (analogous to Eqs. 4-3,2a) can be solved for as follows:

i) average slab aerosol extinction coefficient

$$\overline{\beta_a}_{ij} = \frac{\tau_a(0,x_i) - \tau_a(0,x_j)}{(x_i - x_j)} \quad 4\text{-}4,4a$$

ii) aerosol optical depth

$$\tau_a(0,x_o) = \tau(0,x_o) - \int_o^{x_o} \beta_m \, dx \quad 4\text{-}4,4b$$

iii) integrated optical depth

$$\tau(0,x_o) = \frac{1}{2[\sec\theta_2 - \sec\theta_1]} \ln\left[\frac{\sec\theta_1 \cdot \bar{N}(\theta_1)}{\sec\theta_2 \cdot \bar{N}(\theta_2)}\right] \quad 4\text{-}4,4c$$

iv) scattering ratio

$$S = \frac{N(\theta)\, x_o^2 \sec\theta}{\gamma_\theta u \frac{3}{8\pi} \beta_m \omega_m} \cdot \exp\left[2\sec\theta \cdot \tau(0,x_o)\right] \quad 4\text{-}4,4d$$

v) aerosol volume backscattering coefficient

$$\frac{B_a(\pi)}{4\pi} = (S - 1) \frac{3}{8\pi} \beta_m \omega_m \quad 4\text{-}4,4e$$

vi) average slab phase function for backscattering

$$\frac{\overline{P_a(\pi)}^{ij}}{4\pi} = \frac{B_a(\pi)}{4\pi}\ [\omega_a\ \overline{\beta_a}^{ij}]^{-1} \qquad 4\text{-}4,4f$$

It is very important in the error analysis that the quantity $\hat{\Phi} = |\sec\theta_2 - \sec\theta_1|$ should be as large as possible. However, the equations are physically unrealistic as θ_1 or θ_2 approaches $\pi/2$ radians. A good selection would be θ_1 = zero radians (vertical) and $\theta_2 = \pi/3$ radians so that $\hat{\Phi} = 2$.

The errors are as follows:

i) average slab aerosol extinction coefficient (from 4-4,4a)

$$[\delta\overline{\beta_a}^{ij}]^2 = \frac{1}{(x_i - x_j)^2}\left\{[\delta\tau_a(0,x_i)]^2 + [\delta\tau_a(0,x_j)]^2\right\} \qquad 4\text{-}4,5a$$

ii) aerosol optical depth (from 4-4,4b)

$$[\delta\tau_a(0,x_o)]^2 = [\delta\tau(0,x_o)]^2 + [\delta\tau_m(0,x_o)]^2 \qquad 4\text{-}4,5b$$

iii) integrated optical depth (from 4-4,4c)

$$[\delta\tau(0,x_o)]^2 = \frac{1}{4(\sec\theta_2 - \sec\theta_1)^2} \cdot \sum_{k=1}^{2}\left[\frac{\delta\bar{N}(\theta_k)}{\bar{N}(\theta_k)}\right]^2 \qquad 4\text{-}4,5c$$

iv) scattering ratio (from 4-4,4d)

$$\left(\frac{\delta S}{S}\right)^2 = \left[\frac{\delta\bar{N}(\theta)}{\bar{N}(\theta)}\right]^2 + \left(\frac{\delta\beta_m}{\beta m}\right)^2 + \exp[4\sec\theta \cdot \tau(0,x_o)] \cdot [\delta\tau(0,x_o)]^2 \qquad 4\text{-}4,5d$$

v) aerosol volume backscattering coefficient (from 4-4,4e)

$$\left[\frac{B_a(\pi)}{B_a(\pi)}\right]^2 : \left(\frac{\delta S}{S}\right)^2 + \left(\frac{\delta\beta_m}{\beta_m}\right)^2 + \left(\frac{\delta\omega_m}{\omega_m}\right)^2 \qquad 4\text{-}4,5e$$

vi) average slab aerosol phase function for backscattering (from 4-4,4f)

$$\left(\frac{\delta \overline{P_a(\pi)}^{ij}}{\overline{P_a(\pi)}^{ij}}\right) = \left(\frac{\delta B_a(\pi)}{B_a(\pi)}\right)^2 + \left(\frac{\delta \overline{\beta_a}^{ij}}{\overline{\beta_a}^{ij}}\right)^2 + \left(\frac{\delta \omega_a}{\omega_a}\right)^2 \qquad 4\text{-}4,5f$$

Pro:

1) The aerosol optical properties are well defined at a particular wavelength.

2) The laser and detection systems could be unsophisticated, i.e. low resolution flash lamp pumped dye lasers and low resolution receiver systems could be employed.

Con:

1) Figuring a 1 m. diameter receiver mirror to provide good optics at $\sim \pm 30°$ off axis appears to be expensive. The implementation of this scheme on a Shuttle appears to be more difficult than the preceding schemes. A smaller rotating mirror could be mounted in a pod outside an aircraft, but the cost of building an F.A.A. approved pod would be high. A multiple transmitter system is also a high cost item.

2) Prior knowledge regarding aerosol size and composition is required to incorporate the β_a profiles derived by this technique into a G.C.M.

3) Although considerable technical effort would be required for mirror engineering, the science of remote sensing by lidar from a Shuttle would be negligibly advanced.

4-4-d) System IV: Broad Band High Resolution System

This scheme is similar in principle to System I (HSRL) except that all of the light from an N_2 laser is utilized directly. The broad spectral output of the laser is spread in angle as a function of wavelength so that high spectral resolution is obtained as a function of angle. The receiver system is matched to the transmitter so that radiation which is received at a particular angle must arrive with the appropriate corresponding wavelength, see Appendix IV-3.

Source: N_2 laser-etalon-amplifier combination with off-axis etalon to give a wavelength-encoded angular distribution of laser light with a resolution of 0.001 Å at 3371 Å. Energy per pulse = .003J. Repetition rate = 60 Hz. Pulse duration = 7ns. Energy conversion efficiency ≃ 0.1%.

Receiver: Off-axis three etalon system for high resolution (0.001Å) notch and spike and moderate rejection of scattered solar continuum. Transmittance of instrument = 3%. Quantum efficiency of photomultiplier = 40%.

Overall efficiency ≃ 0.001%.

Limitation: Only useful over short ranges (ground or airplane based) due to possible multiple scattering across wavelength encoded zones in the field of view, which would effectively degrade the effective spectral resolution of the system.

Pro:

1) The derived quantities are well defined at a particular wavelength.

2) The techniques have been demonstrated in the laboratory and the system is reasonably straightforward to implement. (see Appendix IV-3a.)

3) The power utilization efficiency lies between methods #I and #II.

4) The science of laser remote sensing from the ground and aircraft can be advanced.

Con:

1) Multiple scattering in heavy hazes observed from the Shuttle is expected to render it impossible to uniquely assign angles to wavelengths in the receiver system. However the scheme should not be subjected to this limitation in ground and aircraft applications where the separation between the lidar and the atmosphere is smaller. (see Appendix IV-3b)

2) High efficiency coatings for ultraviolet radiation are difficult to fabricate.

3) Prior knowledge regarding aerosol size distributions and composition is required to incorporate this data into a G.C.M.

References

ANSI, (1973), Safe Use of Lasers. American National Standards Institute, Institute, 7-136.1, New York.

Barmore, F.E., (1975), The Filling-In of Fraunhofer Lines in the Day Sky, J. Atm. Sci., 32, pp. 1489-1493.

Cummins, H.Z., N. Knoble, and Y. Yeb, (1964), "Observation of Diffusion Broadening of Rayleigh Scattered Light," Phys. Rev. Letters, 12, 150-153.

Dabberdt, W.F., and W.B. Johnson, (1973). "Atmospheric Effects Upon Laser Eye Safety--Part II, Final Report Stanford Research Institute, Project 7472.

DeLuisi, J.J., B.G. Schuster and R.K. Sato (1975); Separation of Dust and Molecular Scattering Contributions to the Lidar Observation: A Method. App. Opt. 14, 1917-1923.

Fenner, W.R., H.A. Myatt, J.M. Kellam, and S.P.S. Porto, (1973), "Raman Cross Sections of Some Simple Gases," J. Opt. Soc. Am., 63, 74-77.

Fiocco, G., and J.B. DeWolf, (1968), "Frequency Spectrum of Laser Echoes From Atmospheric Constituents and Determination of the Aerosol Content of Air, J. Atm. Sci., 25, 488-496.

Fiocco, G., G. Benedetti-Michelangeli, K. Maischberger, and E. Madonna, (1971), "Measurement of Temperature and Aerosol to Molecule Ratio in the Troposphere by Optical Radar," Nature, Phys. Sci., Letters, 229, 78-79.

Grainger, J.F., and J. Ring, (1962), "Anomalous Fraunhofer Line Profiles," Nature, 193, 762.

Hänsch, T.W., (1972). Repetitively Pulsed Dye Laser for High Resolution Spectroscopy, App. Opt. 11, 895-898.

Kitt, Peak Solar Atlas (1975), in press.

Mack, J.E., D.P. McNutt, F.L. Roesler, and R. Chabbal, (1963), "The PEPSIOS Purely Interferometric High-Resolution Scanning Spectrometer. I. The Pilot Model," App. Opt., 2, 873-885.

McClatchey, R.A., R.W. Fenn, J.E.A. Selby, F.E. Volz, and J.S. Garing, (1971), "Optical Properties of the Atmosphere (revised)" AFCRL-71-0279.

Moses, R.A., Ed., (1970), Adlers Physiology of the Eye; Clinical Application, 5th Edition. St. Louis, C.V. Mosby Co., Chapter 11.

Munter, D.M., (1970), "Surface Albedo and the Filling-in of Fraunhofer Lines in the Day," Astrophys J., 159, 1107-1110.

Noxon, J.F., and R. Goody, (1965), Atmos. and Oceanic Phys., 1, 163.

Penney, C.M., R.L. St. Peters, and M. Lapp, "Absolute Rotational Raman Cross Sections for N_2, O_2, and CO_2," J. Opt. Soc. Am., 64, 212-216.

Pressley, R.J., ed., (1971), CRC Handbook of Lasers, The Chemical Rubber Co., Section 1, "Ocular Hazards" by A.M. Clark, pp. 3-10.

Stowe, L.L., Hilleary, D.T. (1975) Proposal: Adaptation of ERB Scanning Channels for Polarization Measurements.

Wallerstein, R. and Hänsch, T.W., (1975), Powerful Dye Laser Oscillator-Amplifier System for High Resolution Spectroscopy, Optics. Comm. (to appear July 1975)

Wang, W., and G.A. Domoto, (1974), "The Radiative Effects of Aerosols in the Earth's Atmosphere," J. Appl. Meteor., 13, pp. 521-534.

Yip, S., (1971), "Rayleigh Scattering in Dilute Gases," J. Acous. Soc. of Amer., 49, (Part 3), pp. 941-949.

Yip, S., and M. Nelkin, (1964), "Application of a Kinetic Model to Time-Dependent Density Correlations in Fluids" Phys. Rev., 135, pp.A1241-A1247.

Appendix IV-1

On the Derivation of Atmospheric Density from a Temperature Profile in a Dry Atmosphere.

Using the equation of state for an ideal gas and the hydrostatic approximation, the derivative of pressure P with respect to height z is

$$\frac{dP}{dz} = -g\rho = RT\frac{d\rho}{dz} + R\rho\frac{dT}{dz} \qquad \text{IV-1,1}$$

where $R = 2.87 \times 10^6$ erg gm^{-1} $°K^{-1}$ is the gas constant for dry air and g is the acceleration of gravity. Eq. 1 has the solution

$$\rho(z) = \rho(h) \exp\left[-\int_h^z f(z)dz\right] \qquad \text{IV-1,2}$$

for

$$f(z) = T^{-1} \cdot \frac{dT}{dz} + gR^{-1} \cdot T^{-1} \qquad \text{IV-1,3}$$

where $\rho(h)$ and $T(h)$ are the atmospheric density and temperature at height h, respectively. The error in this calculation is

$$\left(\frac{\delta\rho}{\rho}\right)^2\Big|_h = \left(\frac{\delta\rho(h)}{\rho(h)}\right)^2 + \left(\frac{\delta T(z)}{T(z)}\right)^2 + \left[\delta\left(gR^{-1}\int_h^z T^{-1}(z)dz\right)\right]^2 + \left(\frac{\delta T(h)}{T(h)}\right)^2 \qquad \text{IV-1,4}$$

Breaking up the last term of Eq. IV-1,4 into N layers of width u, and letting $\frac{\delta T}{T} = \frac{\delta\rho(h)}{\rho(h)}$ be constant throughout the atmosphere, then

$$\left(\frac{\delta\rho}{\rho}\right)^2 = \frac{1}{2}\left[2 + \left(gR^{-1}\, u\, \sqrt{N} \cdot T^{-1}\right)^2\right] \cdot \left(\frac{\delta T}{T}\right)^2 \qquad \text{IV-1,5}$$

$$= \zeta_{dry}^2 \cdot \left(\frac{\delta T}{T}\right)^2 = \left[1 + \frac{\left(gR^{-1}\, u\, \sqrt{N}\, T^{-1}\right)^2}{2}\right]\left(\frac{\delta T}{T}\right)^2$$

Values of ζ_{dry} as a function of height are plotted for various values of u in Figure IV-1,1.

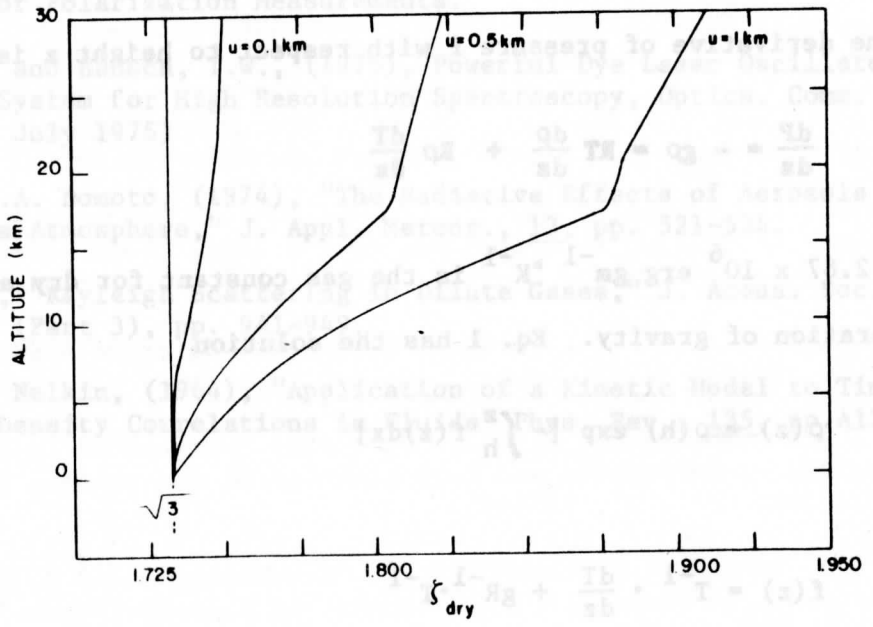

Figure IV-1,1. Values for ζ_{dry} plotted for several values of u as a function of height.

Appendix IV-2 : Determination of the Dependence of the Optical Thickness of Aerosols on Wavelength

The total optical thickness of aerosol layers can be determined as a function of wavelength by means of passive imagery of the earth's surface. This appendix will outline a possible technique that may be employed for this purpose.

IV-2.1 Introduction

The contrast of images of the earth's surface obtained with spectrophotometric instrumentation carried on board aircraft and earth orbiting satellites is frequently degraded by atmospheric haze. This problem has been comprehensively reviewed by Duntley et al. (1964). The solution of radiative transfer problems has advanced since Duntley et al. (1957) identified the factors which affect image contrast degradation so that acceptable models of contrast degradation can now be developed.

A method is presented to compute the degradation of contrast as a function of the following parameters:

1. Optical thickness of the haze
2. Scattering characteristics of the haze particles
3. Solar zenith angle and viewing zenith and azimuth angles
4. Mean surface albedo
5. Contrast of surface features

The following analysis may be used to determine the optical thickness of the haze by measuring the radiances reflected from small objects.

This problem has been investigated by Breitling and Pilipowskyj (1970), Van de Hulst (1971) and Kondratyev et al. (1973). These studies considered

surface features which are horizontally semi-infinite i.e. the mean free path of photons is small compared to the scale of surface features. Such schemes are applicable to surfaces which have features on a scale which exceeds ∿1 km.

However, much imaging over land masses concerns itself with features which are on a scale which is smaller than ∿1 km. The present analysis addresses itself to the computation of contrast of such features viewed through hazes.

IV-2.2 Analysis

Consider a plane parallel hazy atmosphere of optical thickness, τ, illuminated from above by a parallel solar irradiance, F_o, per unit area perpendicular to the incident beam. The radiances diffusely reflected and transmitted are I_R and I_T respectively and they can be expressed in $ster^{-1}$ for unit incident irradiance in a given spectral pass band. The reflection and transmission functions, R and T are defined in terms of the radiances in the manner described by Irvine (1968).*

$$I_R(A_f,\bar{A},\mu,\mu_o,\phi) = \frac{1}{2\pi}\mu_o F_o \sum_{m=0}^{\infty}(1+\delta_{m,0})R_m(\mu,\mu_o)\cos m\phi \qquad \text{IV-2,1a}$$

$$I_T(A_f,\bar{A},\mu,\mu_o,\phi) = \frac{1}{2\pi}\mu_o F_o \sum_{m=0}^{\infty}(1+\delta_{m,0})T_m(\mu,\mu_o)\cos m\phi \qquad \text{IV-2,1b}$$

$$\delta_{m,0} = \begin{cases} 1 & \text{if } m = 0 \\ 0 & \text{if } m \neq 0 \end{cases}$$

Where $\theta_o = \cos^{-1}\mu_o$ and $\theta = \cos^{-1}\mu$ are the solar and viewing zenith angles respectively, and ϕ is the azimuth angle measured from the solar azimuth shown in Fig. IV-2,1.

*The adding procedure is described in detail by van de Hulst (1962), A New Look at Multiple Scattering Mimeographed Report N.A.S.A., Goddard Institute of Space Studies, New York. Unfortunately this report was not widely circulated.

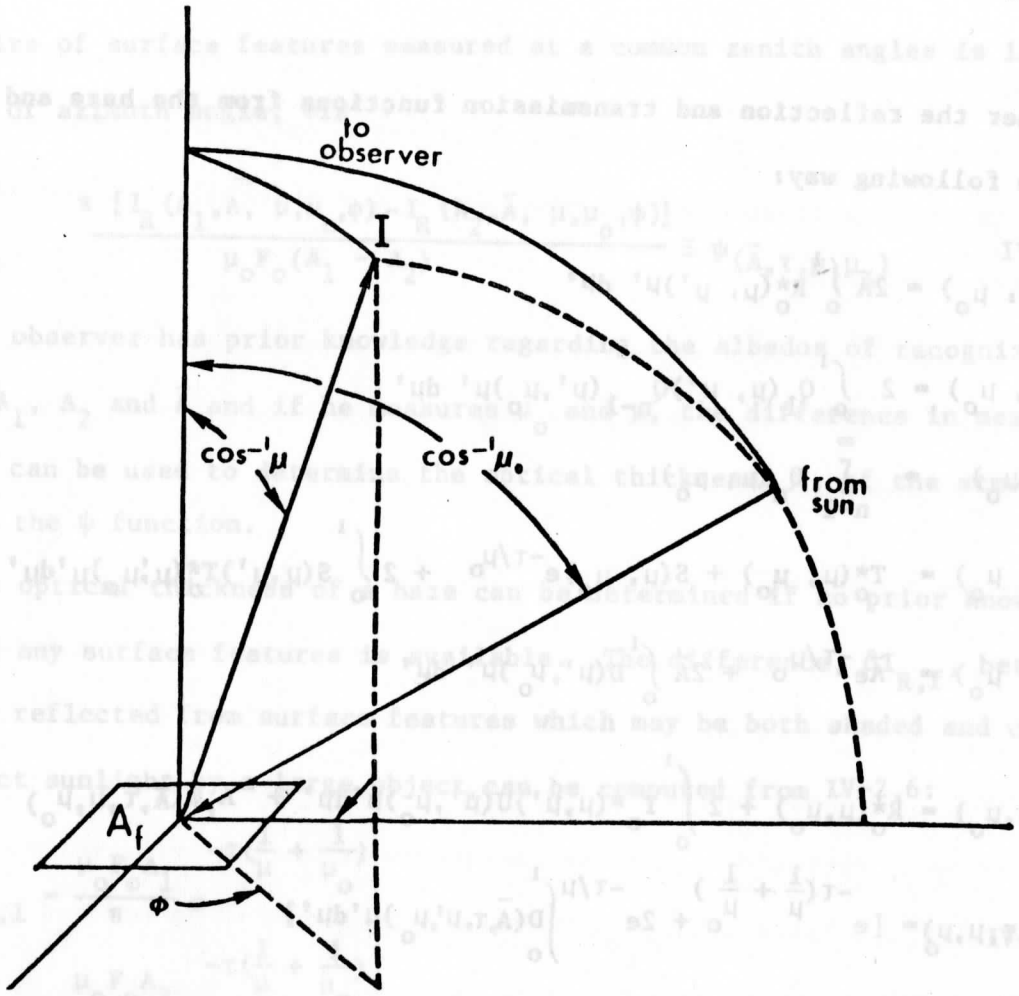

Fig. IV-2,1. Schematic view of coordinates which define the reflected radiance, $I_R(A_f, \bar{A}, \mu, \mu_o, \phi)$, see IV-2,1a.

The surfaces are assumed to Lambertian so that radiances reflected from the surface are azimuthally symmetric. Specular reflectors would contribute to azimuthally dependent terms, $R_m(\mu, \mu_o)$. The underlying surface is assumed to be characterized by an albedo A_f for the small features and by a mean albedo $\bar{A}$ of the surface, averaged over a horizontal scale exceeding the order $\sim$ 1 km. The reflection and transmission functions of the haze alone are designated R_m^* and T_m^*; they can be found by the doubling method which is described by Hansen (1969), for example. The reflection function R_m is found by adding

together the reflection and transmission functions from the haze and the ground in the following way:

$$Q_1(\mu, \mu_o) = 2\bar{A} \int_o^1 R_o^*(\mu, \mu')\mu' \, d\mu' \qquad \text{IV-2,2a}$$

$$Q_n(\mu, \mu_o) = 2 \int_o^1 Q_1(\mu, \mu')Q_{n-1}(\mu', \mu_o)\mu' \, d\mu' \qquad \text{IV-2,2b}$$

$$S(\mu, \mu_o) = \sum_{n=1}^{\infty} Q_n(\mu, \mu_o) \qquad \text{IV-2,3}$$

$$D(\mu, \mu_o) = T_o^*(\mu, \mu_o) + S(\mu, \mu_o)e^{-\tau/\mu_o} + 2 \int_o^1 S(\mu, \mu')T_o^*(\mu', \mu_o)\mu' d\mu' \qquad \text{IV-2,4a}$$

$$U(\mu, \mu_o) = \bar{A}e^{-\tau/\mu_o} + 2\bar{A} \int_o^1 D(\mu', \mu_o)\mu' \, d\mu' \qquad \text{IV-2,4b}$$

$$R_o(\mu, \mu_o) = R_o^*(\mu, \mu_o) + 2 \int_o^1 T_o^*(\mu, \mu')U(\mu', \mu_o)\mu' d\mu' + A_f \psi(\bar{A}, \tau, \mu, \mu_o) \qquad \text{IV-2,5}$$

$$\psi(\bar{A}, \tau, \mu, \mu_o) = [e^{-\tau(\frac{1}{\mu} + \frac{1}{\mu_o})} + 2e^{-\tau/\mu} \int_o^1 D(\bar{A}, \tau, \mu', \mu_o)\mu' d\mu'] \qquad \text{IV-2,6}$$

$$R_m(\mu, \mu_o) = R_m^*(\mu, \mu_o) \quad \text{for } m > 0 \qquad \text{IV-2,7}$$

In IV-2,4a , D is proportional to the downward directed radiance striking the ground, and in IV-2,4b , U is proportional to the radiance averaged over the horizontal surface propagating upward from the ground. The azimuthally averaged reflection from the haze and the surface feature is R_o in IV-2,5. This quantity is the sum of radiances reflected from:

i) the haze
ii) the ground in the direction μ'; the radiance is scattered into the direction μ by the haze. The ground albedo, $\bar{A}$, is averaged over all features.
iii) the surface feature in the direction μ; the radiance is extinguished but not scattered as it propagates in the direction μ. The surface feature has an albedo A_f.

Eq. IV-2,7 is a consequence of the Lambertian characteristic of the surface.

The quantity, ψ, in IV-2,6 is a contrast transmission function whose values lie between 1 for $\tau = 0$ and 0 for $\tau = \infty$; it is proportional to a similar quantity defined by Duntley et al. (1964). The difference between radiances reflected

from pairs of surface features measured at a common zenith angles is independent of azimuth angle, viz

$$\frac{\pi\,[I_R(A_1,\bar{A},\mu,\mu_o,\phi)-I_R(A_2,\bar{A},\mu,\mu_o,\phi)]}{\mu_o F_o(A_1-A_2)} \equiv \psi(\bar{A},\tau,\mu,\mu_o) \qquad \text{IV-2,8}$$

If an observer has prior knowledge regarding the albedos of recognizable features A_1, A_2 and $\bar{A}$ and if he measures μ_o and μ, the difference in measured radiances can be used to determine the optical thickness, τ, of the atmospheric haze from the ψ function.

The optical thickness of a haze can be determined if no prior knowledge regarding any surface features is available. The difference, $\delta I_{R,f}$, between radiances reflected from surface features which may be both shaded and unshaded from direct sunlight by a large object, can be computed from IV-2,6:

$$\delta I_{R,1} = \frac{\mu_o F_o A_1}{\pi} e^{-\tau(\frac{1}{\mu}+\frac{1}{\mu_o})}$$

$$\delta I_{R,2} = \frac{\mu_o F_o A_2}{\pi} e^{-\tau(\frac{1}{\mu}+\frac{1}{\mu_o})} \qquad \text{IV-2,9}$$

These quantities are proportional to the solar irradiance which is reflected from the surface feature and which passes through the haze undeflected by scattering. Combining eqs. (8) and (9) yields an expression which is a function of optical depth, the mean surface albedo, and the viewing and solar zenith angles only:

$$\frac{[I_R(A_1,\bar{A},\mu,\mu_o,\phi)-I_R(A_2,\bar{A},\mu,\mu_o,\phi)]}{[\delta I_{R,1}-\delta I_{R,2}]} = e^{\tau(\frac{1}{\mu}+\frac{1}{\mu_o})}\,\psi(\bar{A},\tau,\mu,\mu_o) \qquad \text{IV-2,10}$$

The optical thickness of the haze can be obtained from this expression because μ and μ_o can be measured and $\bar{A}$ can be estimated.

IV-2,3 Numerical Examples:

Various mixtures of black earth and deciduous trees viewed at wave length $\lambda = 0.8$ μm are modelled to illustrate the degradation of contrast produced by

haze. This wavelength is selected for the example because Rayleigh scattering and gaseous absorption may be conveniently neglected, however the present method is applicable to other wavelengths if due attention is devoted to these considerations.

The haze is assumed to be represented by a water haze M defined by Deirmendjian (1969). This model assumes that the haze particle size distribution is represented by:

$$n(r) = 5.33 \times 10^4 \, r \exp(-8.94 r^{1/2}) \qquad \text{IV-2,11}$$

where r is in μm and n(r) is in $cm^{-3}\mu m^{-1}$. It is assumed that the phase function for $\lambda = 0.7$ μm is valid at $\lambda = 0.8$ μm, and that the albedo for single scattering is $\tilde{\omega}_o = .99999$. The haze is assumed to have optical thickness values $\tau = 0.5$ and $\tau = 2.0$. These optical thicknesses correspond to haze layers, which, if they are ∿1.0 km thick, are characterized by visibility ranges of ∿8 km and ∿ 2 km respectively.

The albedo of trees at $\lambda = 0.8$ μm is $A_t = .53$ and the albedo of soil is $A_s = .05$, see Krinov (1953). Four cases are illustrated in Fig. IV-2,2:

1. A small isolated bare soil patch exists in a forest so that $\bar{A} = A_t = .53$ $A_s = .05$. Table 1 shows the radiances reflected from trees and soil for several solar and viewing angles.
2. A small group of trees exists in a region of bare earth so that $\bar{A} = A_s = .05$, and $A_t = .53$. Table 2 shows the reflected radiances as described above.
3. A broken forest covers half a region of bare soil $\bar{A} = .29$, $A_t = .53$, $A_s = .05$. Table 3 shows the reflected radiances.
4. A semi-infinite bare earth abutts against a semi-infinite deciduous forest $\bar{A}_t = .53$, $\bar{A}_s = .05$. The radiances emerging from tree covered areas are presented in tables 1a, and 1c and those emerging from bare soil areas are presented in tables 2a and 2c.

Table 1

Trees: $\bar{A} = .53$ $A_t = .53$ Soil: $\bar{A} = .53$ $A_s = .05$

$\tau = 0.5$		a				b			
μ	μ_o	$\phi = 0°$	$\phi = 60°$	$\phi = 120°$	$\phi = 180°$	$\phi = 0°$	$\phi = 60°$	$\phi = 120°$	$\phi = 180°$
.17	.38	.339	.100	.060	.071	.329	.090	.050	.061
.38	.38	.151	.081	.062	.071	.137	.068	.049	.057
.62	.38	.085	.069	.061	.065	.063	.046	.039	.043
.96	.38	.061	.060	.060	.059	.031	.030	.030	.030
.17	.83	.147	.125	.110	.109	.103	.080	.065	.065
.38	.83	.146	.137	.131	.132	.086	.077	.071	.073
.62	.83	.141	.139	.137	.141	.075	.072	.071	.075
.96	.83	.138	.138	.140	.141	.064	.065	.066	.067
$\tau = 2.0$		c				d			
.17	.38	.397	.124	.069	.080	.397	.124	.069	.080
.38	.38	.216	.109	.072	.082	.216	.109	.071	.081
.62	.38	.119	.085	.067	.072	.117	.084	.065	.070
.96	.38	.064	.062	.060	.059	.059	.057	.055	.054
.17	.83	.167	.136	.113	.112	.162	.130	.107	.106
.38	.83	.172	.152	.135	.137	.165	.145	.128	.129
.62	.83	.158	.149	.143	.149	.149	.140	.134	.140
.96	.83	.142	.142	.145	.147	.128	.128	.130	.133

Table 2

Soil: $\bar{A} = .05$ $A_s = .05$ Trees: $\bar{A} = .05$ $A_t = .53$

$\tau = 0.5$		a				b			
μ	μ_o	$\phi = 0°$	$\phi = 60°$	$\phi = 120°$	$\phi = 180°$	$\phi = 0°$	$\phi = 60°$	$\phi = 120°$	$\phi = 180°$
.17	.38	.308	.068	.029	.039	.317	.078	.038	.049
.38	.38	.108	.039	.020	.029	.121	.052	.033	.042
.62	.38	.038	.022	.014	.018	.060	.043	.036	.040
.96	.38	.012	.012	.011	.011	.041	.040	.040	.039
.17	.83	.069	.044	.032	.031	.112	.089	.074	.074
.38	.83	.040	.031	.025	.027	.098	.089	.083	.085
.62	.83	.025	.022	.021	.025	.089	.087	.086	.089
.96	.83	.018	.018	.019	.021	.090	.090	.091	.093
$\tau = 2$		c				d			
.17	.38	.381	.107	.053	.064	.381	.107	.053	.064
.38	.38	.194	.086	.049	.059	.194	.087	.049	.059
.62	.38	.090	.056	.038	.043	.091	.058	.040	.045
.96	.38	.030	.028	.026	.025	.035	.033	.030	.030
.17	.83	.116	.085	.062	.061	.121	.090	.067	.066
.38	.83	.102	.082	.065	.067	.109	.088	.072	.073
.62	.83	.071	.062	.056	.062	.079	.071	.064	.071
.96	.83	.042	.042	.044	.046	.055	.055	.057	.059

Table 3

Soil: $\bar{A} = .29$, $A_g = .05$ Trees: $\bar{A} = .29$, $A_t = .53$

$\tau = 0.5$		a				b			
μ	μ_o	$\phi = 0°$	$\phi = 60°$	$\phi = 120°$	$\phi = 180°$	$\phi = 0°$	$\phi = 60°$	$\phi = 120°$	$\phi = 180°$
.17	.38	.318	.079	.039	.050	.328	.089	.049	.060
.38	.38	.122	.053	.034	.043	.136	.066	.047	.056
.62	.38	.050	.034	.026	.030	.072	.056	.048	.052
.96	.38	.021	.021	.020	.020	.051	.050	.049	.049
.17	.83	.086	.063	.048	.048	.129	.107	.092	.091
.38	.83	.062	.054	.048	.049	.121	.113	.107	.108
.62	.83	.049	.047	.046	.050	.115	.112	.111	.115
.96	.83	.041	.041	.042	.044	.114	.114	.115	.117
$\tau = 2.0$		c				d			
.17	.38	.389	.115	.060	.071	.389	.115	.061	.071
.38	.38	.205	.097	.060	.070	.204	.097	.060	.070
.62	.38	.103	.069	.051	.056	.104	.071	.053	.058
.96	.38	.044	.042	.040	.039	.049	.047	.044	.043
.17	.83	.138	.106	.084	.082	.143	.112	.089	.087
.38	.83	.131	.111	.095	.096	.139	.118	.102	.103
.62	.83	.108	.099	.093	.099	.117	.108	.102	.108
.96	.83	.083	.083	.085	.087	.097	.097	.098	.101

Table 4. Downward Directed Irradiance Function

$$2\int_0^1 D(\bar{A}, \tau, \mu', \mu_o)\, \mu'\, d\mu'$$

	$\tau = 0.5$			$\tau = 2.0$		
μ_o	$\bar{A} = .05$	.29	.53	.05	.29	.53
.17	.565	.577	.589	.427	.451	.477
.38	.563	.578	.596	.588	.621	.657
.62	.477	.491	.506	.698	.738	.783
.83	.407	.418	.430	.733	.774	.819
.96	.369	.379	.389	.734	.772	.815

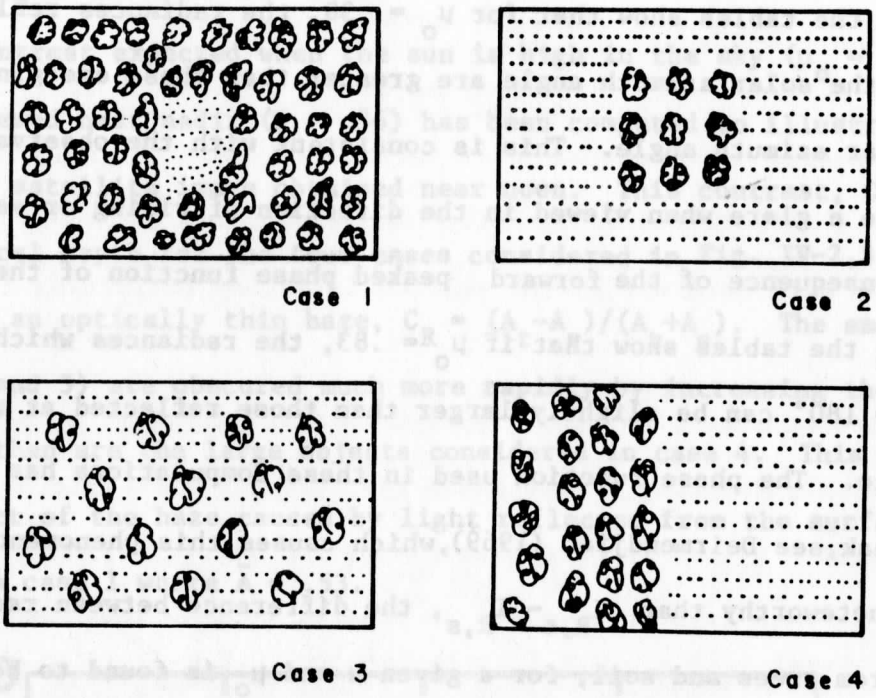

Fig.IV-2,2 Schematic views of various cases showing trees and soil which are considered in this study.

Predicted radiances can be found by multiplying the tabulated values by F_o(the incident solar irradiance in the bandpass of the detector). For example, if a spectrophotometer with a .01 μm bandpass is utilized at $\lambda = 0.8$ μm, Kondratyev (1969) gives the incident solar irradiance $F_o = 11.35$ w m^{-2} $sterad^{-1}$.

Examples of the downward directed diffuse irradiance function, $2\int_0^1 D(\bar{A}, \tau, \mu', \mu_o)\mu' d\mu'$, which appears in IV-2,6 are presented in table 4.

IV-2.4 Discussion:

Inspection of tables 1 through 3 reveal a number of characteristics;

Comparison of radiances computed for $\mu_o = .38$ and $\mu \leq .38$ in tables 1c and 1d, 2c and 2d and 3c and 3d show that if the sun is near the horizon, ground features cannot be distinguished through a thick haze near the hori-

zon even though such features may be evident near nadir.

All of the tables show that for $\mu_o = .38$, the radiances reflected from the haze at the solar azimuth angle are greater than those emerging at 180° from the solar azimuth angle. This is consistent with the observation that hazes produce a glare when viewed in the direction of rising or setting sun; it is a consequence of the forward peaked phase function of the haze.

All of the tables show that if $\mu_o = .83$, the radiances which are scattered at $\phi = 180°$ can be slightly larger than those reflected at the solar azimuth angle. The phase function used in these computations has a slight backscattering peak, see Deirmendjian (1969), which causes this phenomenon.

It is noteworthy that $I_{R,t} - I_{R,s}$, the difference between radiances reflected from trees and soil, for a given μ and μ_o is found to be independent of azimuth angle. This is a consequence of the Lambertian character of these surfaces and it follows from IV-2,5 and IV-2,6.

Representative values of the downward directed diffuse irradiance function which appears in IV-2,6 are presented in table 4. Values of this function which are appropriate for various values of τ, μ_o and $\bar{A}$ can be obtained by interpolation of the numbers presented in that table. It should be noted that the earth's curvature renders results obtained for $\mu_o \leq 0.3$ somewhat unreliable.

Visual contrast is defined by Middleton (1952) as

$$C_M = (I_R - I_R')/I_R' \qquad \text{IV-2,12}$$

where I_R is the radiance reflected by an object and I_R' is the radiance reflected by the background. The distinction between object and background is not clear if an inhomogeneous surface is viewed from above. Duntley et al. (1964) introduced a modulation contrast function which avoids the need to distinguish which surface feature comprises an object and which is the background:

$$C_R = (I_R - I_R')/(I_R + I_R') \qquad \text{IV-2,13}$$

We will use C_R in the following discussion.

The contrast expected when the sun is high in the sky (μ_o = .83) and the ground is viewed near nadir (μ = .96) has been computed to illustrate the effect of haze on a satellite image obtained near noon. This contrast, C_R, is plotted against optical depth for the four cases considered in Fig. IV-2,3. Note that in the limit of an optically thin haze, $C_R = (A_t - A_s)/(A_t + A_s)$. The small objects (cases 1, 2 and 3) are obscured much more rapidly by increasing the thickness of the haze than are the large objects considered in case 4. This is due to the veiling effect of the haze caused by light reflected from the surface, especially in case 1 where $\bar{A}$ = .53.

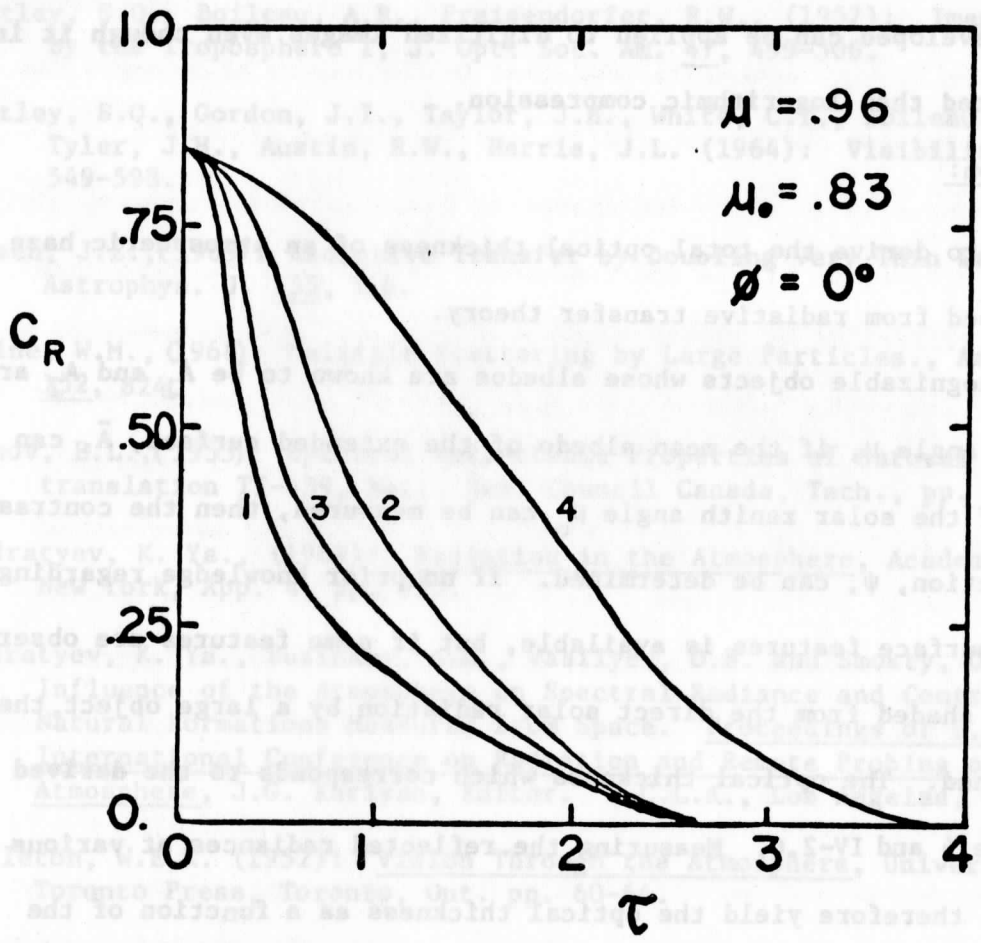

Fig. IV-2,3. Modulation contrast function, C_R, as a function of the optical thickness of hazy atmosphere covering surfaces shown in Fig. IV-2,2. The number on each curve identifies the case considered.

Fig. IV-2,3 shows that the semi infinite representation of a horizontally inhomogeneous surface (case 4) overestimates the modulation contrast if the surface is actually heterogeneous on a horizontal scale which is smaller than 1 km. Multiple reflections between the hazy atmosphere and the surface degrade the modulation most severely if the surface is highly reflecting (see case 1 with large $\bar{A}$).

It should be noted that the visual modulation contrast is proportional to the logarithmic response of the human eye; however much data obtained from photoelectric remote sensing instrumentation is proportional to reflected radiances, I_R. Such data is obtained in digital form so that the algorithm which we have developed can be applied to digitized images even though it is more sophisticated than logarithmic compression.

IV-2.5 Conclusion:

A method to derive the total optical thickness of an atmospheric haze has been developed from radiative transfer theory.

If two recognizable objects whose albedos are known to be A_1 and A_2 are found at zenith angle μ, if the mean albedo of the extended surface, $\bar{A}$, can be estimated and if the solar zenith angle μ_o can be measured, then the contrast transmission function, ψ, can be determined. If no prior knowledge regarding the albedos of surface features is available, but if some features are observed to be partially shaded from the direct solar radiation by a large object, then ψ can also be determined. The optical thickness which corresponds to the derived ψ can be found from table 4 and IV-2,6. Measuring the reflected radiances at various wavelengths will therefore yield the optical thickness as a function of the corresponding wavelengths.

Acknowledgments:

We wish to thank Dr. J. E. Hansen of the Institute for Space Studies G.S.F.C. for providing us with a copy of his doubling program.

References for Appendix IV-2.

Breitling, P.J., Pilipowskyj, S.,(1970): Computer Simulation of Optical Contrast Reduction Caused by Atmospheric Aerosol. AIAA paper #70-194, AIAA 8th Aerospace Sciences Meeting, New York. American Inst. of Aeronautics and Astronautics, 1290 Ave. of Americas, N.Y.

Deirmendjian,(1969): Electromagnetic Scattering on Spherical Polydispersions, American Elsevier Publishing Co., Inc., New York, pp. 290.

Duntley, S.Q., Boileau, A.R., Preisendorfer, R.W., (1957): Image Transmission by the Troposphere I, J. Opt. Soc. Am. 47, 499-506.

Duntley, S.Q., Gordon, J.I., Taylor, J.H., White, C.T., Boileau, A.R., Tyler, J.H., Austin, R.W., Harris, J.L. (1964): Visibility, App. Opt. 3, 549-598.

Hansen, J.E.,(1969): Radiative Transfer by Doubling Very Thin Layers, Astrophys. J. 155, 566.

Irvine, W.M., (1968): Multiple Scattering by Large Particles., Astrophys. J. 152, 824.

Krinov, E.L.,(1953): Spectral Reflectance Properties of Natural Formations, translation TT-439, Natl. Res. Council Canada, Tech., pp. 268.

Kondratyev, K. Ya., (1969): Radiation in the Atmosphere, Academic Press, Inc., New York, App. 4, pp. 912.

Kondratyev, K. Ya., Buzinkov, A.A., Vasilyev, O.B. and Smokty, O.I.,(1973): Influence of the Atmosphere on Spectral Radiance and Contrasts of Natural Formations Measured from Space. Proceedings of U.C.L.A. International Conference on Radiation and Remote Probing of the Atmosphere, J.G. Kuriyan, Editor. U.C.L.A., Los Angeles, CA, pp. 309-336.

Middleton, W.E.K. (1952): Vision Through the Atmosphere, University of Toronto Press, Toronto, Ont. pp. 60-64.

Van de Hulst, (1971): Some Problems of Amisotropic Scattering in Planetary Atmospheres, presented at Symposium #40 on Planetary Atmospheres, Marfa, Texas, Oct. 26-31, 1969. C. Sagan, T. Owen, H. Smith, Editors. D. Reidel Publishing Co., Dordrecht, Holland. pp. 177-185.

Appendix IV-3: The Direct Use of a Nitrogen Laser for a Broad Band High Resolution Lidar (System IV)

IV-3a) Experimental Considerations of System IV

In preliminary experiments we showed that individual lines from the N_2 laser output at 3370 Å can be as narrow as about 4mÅ; however the energy is distributed among a large number of lines covering an approximately 1 Å bandwidth. Consequently, using conventional practices, an impractically small fraction of the N_2 laser light is available for the high-resolution scheme.

It would be possible to make use of the full output energy if the output could be directed to obey the proper wavelength vs. angle law. An explanation and demonstration of this scheme is contained in the papers of Trauger and Roesler (1972), Roesler and Stoner (1973), and Trauger et al.(1973). Basically the scheme is to match the change in wavelength with viewing angle to the angular dispersion of the spectrometer. As shown in the references, excellent results are obtained when the wavelength vs. angle is produced by source motion. To apply this idea to the atmosphere, it is necessary to illuminate the atmosphere with light having the proper λ vs. θ behavior.

What needs to be demonstrated is that one can force the laser output to deliver its energy in the proper λ vs θ relationship. Since a special N_2 laser would have to be built for this purpose, we have investigated the possibilities using an N_2 pumped dye cell. The λ vs θ function was obtained using a wedge etalon as shown in Fig. IV-3,1.

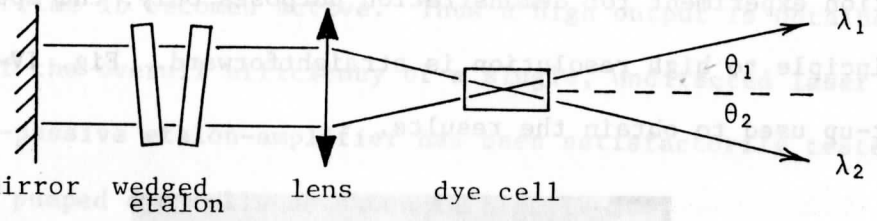

Fig. IV-3,1. Schematic view of a system IV transmitter.

Light passing through the top of the etalon has wavelength λ_2. It reflects from the mirror back through the same part of the etalon and is directed by the lens through the active region of the dye cell at angle θ_2. Similarly light of wavelength λ_1 passes through the lower portion of the dye cell and finally emerges at angle θ_1; intermediate wavelengths are found at intermediate angles. Figure IV-3,2 shows a photograph of the output light dispersed horizontally by a coarse grating. Five grating diffraction orders

Fig. IV-3,2. Output of laser system IV prototype. Output angle is displayed vertically, while grating dispersion is horizontal. Dispersion in highest (right-most) order is $\sim$5Å/mm. Lower exposure is for a smaller wedge angle.

of the active range of the dye are seen, each crossed by several diagonal bands (one for each etalon order) demonstrating the change of wavelength with angle. The picture is a double exposure in which the wedge angle has

been changed between exposures, and consequently the wavelength difference between top and bottom of the etalon is different. While this was a low resolution experiment for demonstration purposes only, the application of the principle to high resolution is straightforward. Fig. IV-3,3 shows the set-up used to obtain the results.

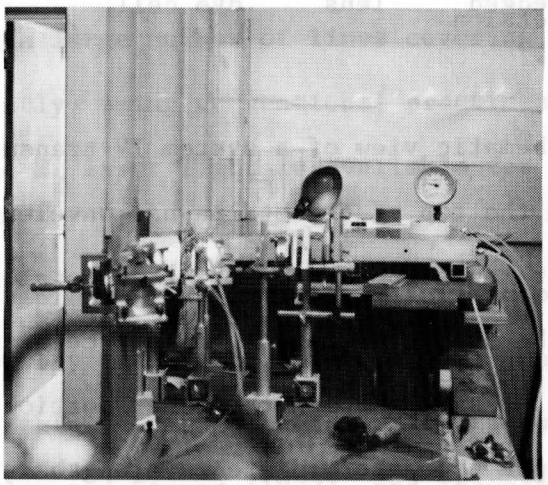

Fig. IV-3,3. View of N_2-pumped dye laser system configured as system IV type transmitter. Note output projected on wall.

To make this scheme work with the N_2 laser one must use a slightly different approach, the elements of which have been demonstrated. As shown above, to achieve the proper λ vs.θ behavior, the active medium must be directed. Since the dye cell is short and can amplify at any λ within its range, an etalon is sufficient for this. The N_2 laser is highly superradiant and photons generated spontaneously at one end are amplified as they travel down the discharge tube. In order to prevent this, properly selected "leader photons" must be present in the laser tube before it becomes active. This can be accomplished by the following proposed oscillator-amplifier scheme: Two lasers are triggered by the same spark gap trigger, the first laser being adjusted to become active 3-4 ns before

the second. The output of the first is filtered by an external passive etalon to obey the proper λ vs. θ function and fills the second with leader photons by the time it becomes active. Thus a high output is obtained with about half the overall efficiency of a single, undirected laser output. The oscillator-passive etalon-amplifier has been satisfactorily tested using nitrogen pumped dye cells as shown in Fig. IV-3,4.

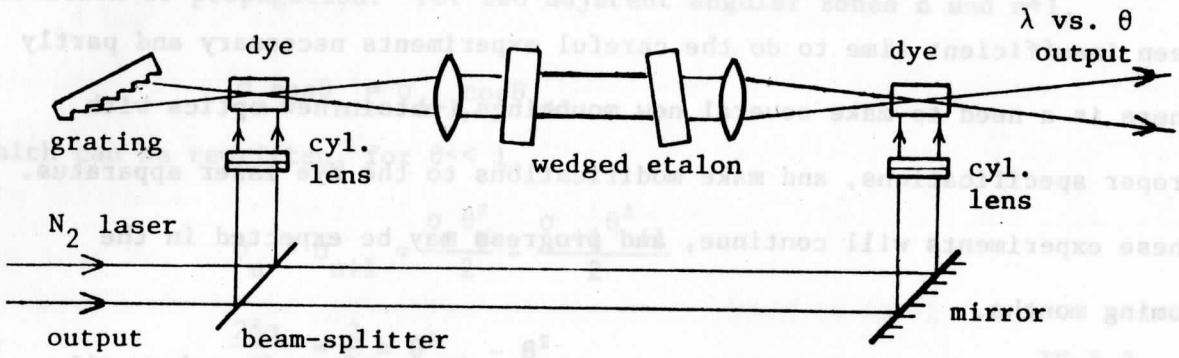

Fig. IV-3,4. Simplified schematic view of oscillator-amplifier dye laser for system IV use.

The experiments with the N_2 laser-pumped dye cells have been conducted to demonstrate the principles and gain experience with the various possibilities before designing a special N_2 laser system. The experiment illustrated in Fig. IV-3,4 has been conducted with a large gap etalon providing high resolution. We have also conducted experiments to determine the optimum timing of pulses in the dye laser - amplifier combinations. Since the N_2 laser pulse is short, it is important that the pumping radiation reach the amplifier dye cell properly timed so that maximum efficiency is obtained in amplifying the narrowed etalon output. The delays caused in narrowing the oscillator output by the grating-etalon combination are significant, and the scheme shown in Fig. IV-3,4 is not optimum; greater

delay should be provided by lengthening the N_2 laser light path to the amplifier dye cell.

The status of experiments aimed at optimizing the timing is as follows: we have noted the delays and the loss of efficiency when the separation between the grating and dye cell is increased, and have made some attempts to increase the efficiency by adjusting the timing. The efficiency experiments have been somewhat inconclusive. Partly there has been insufficient time to do the careful experiments necessary and partly there is a need to make several new mountings, obtain new optics with proper specifications, and make modifications to the dye laser apparatus. These experiments will continue, and progress may be expected in the coming months.

Experiments are also being made to determine the optimum dye cell size and the optimum splitting of the N_2 laser light. Considerable progress has been made, but more careful work under more carefully controlled conditions is required.

IV-3b) Theoretical Limitations of System IV.

The broad band high spectral resolution lidar system is designed so that the radiance which is propagated at an angle ψ with respect to the laser axis is a unique function of the wave length. Similarly the radiance which is backscattered to the lidar receiver is expected to be a unique function of ψ', the angle between the propagated direction and the receiver axis. The lidar system is designed so that:

$$\psi d\psi = \psi' d\psi' \quad \text{and} \quad \psi(\lambda) = \psi'(\lambda) \qquad \text{IV-3,1}$$

The angle ψ is proportional to θ and the ratio of the apertures of the lidar and the etalon system.

A spectral resolution $\delta\lambda = 10^{-3}$ Å at 3371 Å corresponds to

$$R = \frac{\lambda}{\delta\lambda} = \frac{\sigma}{\delta\sigma} = 3.37 \times 10^{6} \qquad \text{IV-3,2}$$

where σ is the wave number.

The resonance condition in an etalon with spacing ℓ and refractive index μ requires

$$2\mu\ell\sigma \cos\theta = k$$

where k is an integer, and θ is the angle between the optic axis and the direction of propagation. For two adjacent angular zones n and n+1,

$$\sigma_n \cos\theta_n = \sigma_{n+1} \cos\theta_{n+1}$$

which can be rewritten, for $\theta << 1$,

$$\sigma_n - \sigma_{n+1} \simeq \frac{\sigma_n \theta_n^2}{2} - \frac{\sigma_{n+1}\theta_{n+1}^2}{2}$$

or

$$\frac{2\delta\sigma}{\sigma} = \frac{2}{R} \simeq \theta_{n+1}^2 - \theta_n^2 \qquad \text{IV-3,3}$$

if

$$\theta_o = 0 \ , \ \theta_1 = 7.7 \times 10^{-4} \text{rad} \qquad \text{IV-3,4}$$

and

$$\theta_n = \sqrt{n} \ \theta_1$$

If the etalon system is designed to accept 20 zones, i.e. n = 20, then the maximum receiver field of view angle is

$$\theta_{20} = 3.45 \times 10^{-3} \text{ radians} \qquad \text{IV-3,5}$$

The ratio of apertures of the telescope and the etalon reduce this angle so that for a 5 cm diam. etalon system and a 1 m diam. telescope which is proposed for the Shuttle

$$\psi' = 1.72 \times 10^{-4} \text{ radian} \qquad \text{IV-3,6a}$$

while an aircraft system with a 20 cm diameter telescope has

$$\psi' = 6.90 \times 10^{-4} \text{ radians.} \qquad \text{IV-3,6b}$$

Conditions cited in Eq. IV-3,1 can be achieved if single scattering is the only scattering mechanism; however, multiple scattering degrades the angular and hence the spectral resolution of the proposed high spectral

resolution lidar system.

The theory developed by Weinman (1976) was used to estimate the magnitude of multiple scattering. The hazes which we investigated were assumed to have extinction coefficients β = 2 km^{-1} and 0.2 km^{-1} which are independent of altitude. These models correspond to visibilities of 2 and 20 km respectively. These conditions are found at the surface for the BF = 10 and BF = 1 models respectively; see Tables 3-1 and 3-2. The lidar is assumed to be located distances h_o [1] from the haze; h_o = 185 km for the Shuttle case and h_o = 10 km for the aircraft case. The phase function is approximated by the parameters applicable to Haze-C cited in Table 1 of the Weinman paper. M_N and M_1 are the total and the singly scattered lidar return measurements.

Table IV-3,1. Ratio of Multiple to Single Scattering, $(M_N-M_1)/M_1$, from a System IV Lidar.

	β = 2 km^{-1}	β = 0.2 km^{-1}
Shuttle (h_o = 185 km)	.213	.030
Aircraft (h_o = 10 km)	.065	.008

The entries in Table IV-3,1 represent the proportion of multiply scattered lidar photons which both enter the atmosphere within the angle ψ' (Eqns. IV-3,6) and return within the same angle. Since any multiply scattered photon has roughly a .95 probability of being received in a different resolution zone, this has the effect of degrading the high spectral resolution and nullifying the potential advantage of this technique.

(1) The distance separating the lidar from the haze, h_o, is designated H' by Weinman.

In summary, the scheme presented here for producing a wavelength encoded angular distribution of laser radiation, together with a properly tuned PEPSIOS receiver, make it possible to use a larger proportion of the available direct N_2 radiation in a proposed HSRL system. In the example presented here, 2% of the available N_2 energy available across a 1 Å band width, has been utilized at an effective resolution of 10^{-3} Å. However, the solid angle of the field of view has been correspondingly increased 20-fold. Thus solar background radiation has also increased 20-fold. This scheme is susceptible to degradation of the spectral resolution due to multiple scattering within the field of view, as discussed above. Finally, the tolerance in angular alignment of the laser and receiver field of view has been decreased by a factor of $1/2\sqrt{20}$.

References for Appendix IV-3.

Roesler, F. L., Stoner, J. O. Jr., (1973): High-Resolution Fast-Beam Spectroscopy Using an Off-Axis Fabry-Perot Interferometer. Nuc. Instr. and Methods 110, 465-

Trauger, J. T., Roesler, F. L., (1972): Fabry-Perot Spectrometer Adjustment for the Compensation of Doppler Shift from Rapidly Rotating and Rapidly Flowing Sources. App. Opt. 11, 1964-

Trauger, J. T., Roesler, F. L., Carleton, N. P., Traub, W., (1973): Observation of HD on Jupiter and the D/H Ratio. Astrophys. J. 184, L137-

Weinman, J. A., (1976): Effects of Multiple Scattering on Light Pulses Reflected by Turbid Atmospheres. J. Atom. Sci. (to be published).

5-0 Conclusion

The most widely dispersed aerosol in the atmosphere originates over deserts. Models of the desert aerosol were defined on the basis of the varied data presented in the literature. Radiative heating and cooling rates produced by such model aerosols were computed using computational schemes which are sufficiently fast yet accurate enough to be incorporated into General Circulation Models. (The results obtained from General Circulation Models which include perturbations due to desert aerosols are not presented in this report. The first results are emerging as this conclusion is being written.) General Circulation Models are inherently noisy due to the finite temporal and spatial increments which they employ. Such noise corresponds to an uncertainty of 0.5°C/day in the heating rate. An analysis was conducted to show how this uncertainty in heating rate ultimately manifests itself on the aerosol optical extinction profile. This analysis provided the foundation for the design of two specific lidar systems: one which could be flown on the Shuttle missions and the other on an aircraft.

High Spectral Resolution Lidar (or HSRL) systems may be used to separate the light scattered by aerosols from that scattered by molecules in order to determine vertical profiles of the aerosol extinction coefficient. All HSRL systems considered were eyesafe for the unaided eye looking up from the Earth's surface.

It was found that the HSRL dye laser experiment is feasible for aircraft deployment using present technology. Solar noise is not a problem due to the relatively high returned powers, and consequently HSRL operation in a Fraunhofer line is not necessary.

The simplest aircraft borne system would deliver 3 mw of optical power @ 60 Hz from a platform located at h_o = 10 km above the Earth's surface. Such a system will provide values for the aerosol extinction coefficient in vertical intervals of depth u = 0.75 km with sufficient accuracy to determine atmospheric heating due to aerosols within ± 0.5°K day^{-1}.

The simplest Shuttle borne system would deliver 3 mw of optical power @ 60 Hz from a platform located at h_o = 185 km above the Earth's surface. This system also determines the aerosol extinction coefficient in vertical intervals of depth u = 0.75 km with sufficient accuracy to determine atmospheric heating due to aerosols within ± 0.5°K day^{-1}. This system yields solar background levels which are higher than the returned signal strength; however operation in a Fraunhofer line using a receiver field of view which is a practical optical (component) limit gives a feasible value for $\bar{N}_s/\bar{N}_m$. Thus, the Shuttle borne HSRL is theoretically capable of providing the desired information on $\overline{\beta_a}$, but it is at the limit of current technology.

Solar noise could be reduced by employing a flash-lamp pumped transmitter which would deliver 3 mw @ 1 Hz repitition rate with the desired spectral resolution. This would eliminate the need for a very small receiver field of view and operation in a Fraunhofer line. However it would be difficult to attain both the high spectral resolution and high spectral stability using a flash-lamp pumped transmitter.

It appears that a 15 mw @ 60 Hz dye laser is forthcoming. Our analysis shows that HSRL operation from the Shuttle using such a dye laser system, operating in a Fraunhofer line, is capable of yielding vertical profiles of the aerosol extinction coefficients both by day and night.